

December 20, 1987

Final Report
Covering the Period
September 1, 1986 to August 31, 1987

IMPACT OF SOLIDS ON COMPOSITE MATERIALS

By

Arturo Bronson*, Jerry Maldonado, Tzong Chern,
Francisco Martinez, and Johnnie McCord-Medrano
Department of Metallurgical Engineering
University of Texas at El Paso

and

Paul N. Roschke*
Department of Civil Engineering
Texas A & M University

Prepared for:

NASA Lyndon B. Johnson Space Center
Mail Code: ES2
Houston, Texas 77058

ATTENTION: Dr. Orvis E. Pigg

NASA Grant No. NAG 9-175

*A. Bronson and P. Roschke are Principal Investigators for the
research project.

(NASA-CR-182395) IMPACT OF SOLIDS ON
COMPOSITE MATERIALS Final Report, 1 Sep.
1986 - 31 Aug. 1987 (Texas Univ.) 83 p
CSCL 11D

N88-15015

Unclas
G3/24 0118835

TABLE OF CONTENTS

	SUMMARY OF OVERALL PROGRESS	1
I.	INTRODUCTION	1
	A. Impact Induced Failure	2
	B. Failure Mode Analysis	5
	C. Finite Element Analysis	7
	D. Summary	8
II.	METHODOLOGY	9
III.	RESULTS AND DISCUSSION	13
III.	SUMMARY OF FUTURE OBJECTIVES	18
IV.	REFERENCES	20
	LIST OF FIGURES	24
	Appendix A	A1
	Appendix B	A2
	Appendix C	A3

SUMMARY OF OVERALL PROGRESS

The research project investigates the failure modes of composite materials as a result low velocity impact by simulating the impact with a finite element analysis. An important facet of the project is the modeling of the impact of a solid onto cylindrical shells composed of composite materials. Most computer models have been developed for laminated composites in the form of plates and under uniform displacement or load. The model under development will simulate the delamination sustained when a composite material encounters impact from another rigid body.

For the year, the investigators installed computer equipment, tested the computer network and developed a finite element model to compare results with known experimental data. The model simulated the impact of a steel rod onto a rotating shaft. The rod scribes the surface and creates a plowed region which is subsequently measured optically for the surface area. The surface area was then compared with the results of the three dimensional finite element analysis.

Pre-processing programs (GMESH AND TANVEL) were developed to generate node and element data for the input into the three dimensional, dynamic finite element analysis code (DYNA3D). The finite element mesh was configured with a fine mesh near the impact zone and a coarser mesh for the impacting rod and the regions surrounding the impact zone. For the computer simulations, five impacting loads (35, 50, 85, 185 and 285g) were used to determine the time history of the stresses, the scribed surface areas, and the amount of ridging. The processing time of the computer codes amounted from 1-4 days. for example, the calculations for the 85g impact onto the rotating shaft approximated 45 hours of central processor unit's time. The calculated surface area were within 6-12 percent, relative error when compared to the actual scratch area.

I. INTRODUCTION

Composite materials have been increasingly used for structural materials because of their high strength-to-weight ratio. These newly developed materials are by no means excluded from damage resulting from low-velocity impact. In some cases of normal use, these materials may appear to be sound when struck by a foreign object, but interior structural damage may result from the separation between laminae. The delamination would not be immediately known and could later expand in use.

Delamination has caused significant concern in the design and analysis of composite materials and structures. The

failure is complicated because it involves geometric and material discontinuities (i.e. interlaminar cracks and variation of ply properties in the transverse direction), as well as the coupled mode I, mode II, and mode III fracture in a layered anisotropic material system. For reference the three types of relative movements of the cracking surfaces have been shown in Fig. 1. Mode I represents the symmetric displacements with respect to the x-y and x-z planes. The sliding or shear mode, Mode II, has symmetry with respect to the x-y plane and distorted with respect to the x-z plane. The tearing mode, Mode III, has displacements that are distorted with respect to both x-y and x-z planes.

A target-impactor test and including some models have been developed to study the effects of composite materials under different dynamic loading conditions. From results of this test, important data on the stress-strain-delamination relationship can be used to make further studies on the behavior of multidirectional composites to low-velocity impact.

In this section, a brief summary of the relevant literature on composite materials is presented on failures resulting from impact and the failure modes of composite materials from a fracture mechanics viewpoint. The review is not an extensive discussion of the subject but will serve as an eye-opener to the complicated nature of failure modes of composite materials.

A. Impact Induced Failure

The behavior of multidirectional composites to dynamic loads, as a function of laminae thickness, geometry, and load, is an important indicator of their damage resistance. In many structural applications impact behavior is considered one of the most important criteria for material selection [2]. The emphasis for the development of tougher graphite fiber reinforced composites has brought an increase in composite impact testing. The data obtained from these tests can be used to provide valuable information about the impact failure mechanisms and the variables which can affect the impact resistance of graphite-fiber-reinforced polymer matrix composites [3].

The approach in studying the response of composite materials to low-velocity impact is shown in Fig. 2. The three major steps of the approach are: (1) determination of impactor-induced surface pressure and its distribution, (2) determination of internal stresses in the composite target caused by the surface pressure, and (3) determination of failure modes in the target caused by the internal stresses [4].

Shivakumar, Elber and Illg [5] have analyzed circular composite plates under static equivalent impact loads. Their analysis was based on the minimum potential energy method. The ply failure region and mode were calculated by using the Tsai-Wu [6] and the maximum stress criteria [7] given in Appendix A. A step-by-step incremental transverse displacement procedure was used to calculate plate load and ply stresses. Their analysis predicted the following:

- 1.) The first failure mode was splitting and initiated first in the bottom-most ply.
- 2.) The splitting failure thresholds were relatively low and tended to be lower for larger plates than for small plates.
- 3.) The splitting damage region in each ply was elongated in its fiber direction; the bottom ply had the largest damage region.
- 4.) Larger plates developed larger splitting damage regions than smaller plates subjected to the same transverse load.
- 5.) First fiber failure threshold (load or energy) are higher for large plates over a limited range of fiber radius-to-thickness ratio ($r/t > 10$).

Delamination in composite materials usually follows a geometrical pattern from the first ply to the last as reported by Sankar and Sun [8]. In their investigation of graphite/epoxy beams, they reported that impact loads will readily create two types of cracks: (1) a single longitudinal crack on the back surface symmetric about the impact point and (2) two parallel longitudinal cracks on either side of the impact point. Also, a damage area on the front side (or impact side) was always on either side of the longitudinal axis of symmetry. On the back side there is usually two damage areas on either side of the transverse line of symmetry; whereas in the center, delamination occurs in all four quadrants. A representative C-scan of the damage area is shown in Fig. 3.

The plastic deformation at the delaminated crack tip can be accounted for in a number of ways by elasto-plastic fracture mechanics theories. Mahishi and Adams [9] made studies on the initiation and growth of delaminations in central and single-edge notched $[+45/0]_s$ graphite/epoxy laminates. The symbolism for the laminate code has been explained in Appendix C. A three-dimensional elasto-plastic, generally orthotropic, finite-element method developed by Monib and Adams [10] was used and has been summarized in Appendix B. They assumed that the edge delamination involves only matrix-dominated fracture, based on elastic and brittle behavior, and that the crack surface is parallel to the ply interface.

Their criteria for delamination was based on the local elastic strain energy release rate in the presence of plasticity and they accounted for the coupled Mode I, II, and III delamination. Once their energy release rate was evaluated it was compared with experimentally measured fracture toughness values and when they were equal, the nodes were separated to simulate the crack growth. The experimentally measured [11] fracture toughness values for a Hercules AS4/3501-6 graphite/epoxy composite, namely, $G_{IC} = 130 \text{ J/m}^2$ and $G_{IIc} = G_{IIIc} = 230 \text{ J/m}^2$, were used as critical energy release rates.

The elastic strain energy release rate in the presence of plasticity for the three modes of fracture were given as:

$$G_I = \frac{1}{2\Delta A} [F_{zz}^2/K_{zz} - (F_z - \sigma_{zz}^Y \Delta a)^2/\bar{K}_{zz}] \quad (1)$$

$$G_{II} = \frac{1}{2\Delta A} [F_x^2/K_{zx} - (F_x - \tau_{zx}^Y \Delta a)^2/\bar{K}_{zx}] \quad (2)$$

$$G_{III} = \frac{1}{2\Delta A} [F_y^2/K_{zy} - (F_y - \tau_{zy}^Y \Delta a)^2/\bar{K}_{zy}] \quad (3)$$

where

Δa = incremental crack growth,

ΔA = area of the incremental crack,

F_x, F_y, F_z = force components,

K_{zz}, K_{zx}, K_{zy} = total stiffness coefficients,

$\bar{K}_{zz}, \bar{K}_{zx}, \bar{K}_{zy}$ = reduced stiffness coefficients, and

$\sigma_{zz}^Y, \tau_{zx}^Y, \tau_{zy}^Y$ = yield stress values.

The total elastic strain energy release rate is then

$$G_L = G_I + G_{II} + G_{III} \quad (4)$$

Their analysis demonstrated that the proposed elasto-plastic fracture criterion is very effective in predicting stable delamination crack growth in composite laminates having non-

linear matrix-dominated properties. The result did predict a very large area of delamination because of the coarse grid used in their analysis.

Joshi and Sun [12] experimentally studied crack patterns in conjunction with numerical results under impact induced fracture in a $[0_5/90_5/0_5]$ laminated composite plate. They established the rôle of transverse shear stress in proximal and middle layer crack initiation. Delamination zones were constructed using metallographic techniques of the damaged area. Their study is important in understanding the behavior of each laminae under dynamic loading by observing crack path versus shear stress maximum.

Figure 4 is a typical fracture pattern of a transverse section approximately 0.5 mm from the impact point which was observed by Joshi and Sun [12]. Figure 5 shows details of the finite element mesh used to calculate the shear stresses shown in Figures 6 to 9. They concluded that a crack in the upper layer appeared to start at point B (in Fig. 4) and moved towards point C, from which delaminated crack propagates. A strong correlation can be seen (Figs. 6 to 9) between the crack path in the upper layer and the locus of the shear stress maximum.

B. Failure Mode Analysis

One of the underlying principles of fracture mechanics is that unstable fracture occurs when the stress-intensity factor at the crack tip reaches a critical value. By knowing the critical value of K_I , K_{II} , and K_{III} at failure for a given material of a particular thickness and at a specific temperature and loading rate, the designer can determine flaw sizes that can be tolerated in structural members for a given design stress level. Conversely, for an existing crack that may be present in the structure the design stress level can be safely determined [13].

The interfacial cracks in multidirectional composite are introduced during fabrication or processing operations. These defects may be caused by incomplete wetting or trapped air bubbles between layers, or by debonding of two laminae as a result of high-stress concentrations at geometric or material discontinuities [14]. Kuo and Wang [15] defined the stress-intensity factors of the singular stress field around a crack tip as

$$\sigma_y = \frac{K_I}{(2\pi x)^{1/2}} \cos[\gamma \ln(x/a) + \beta] \quad (5)$$

$$\tau_{xy} = \frac{K_{II}}{(2\pi x)^{\frac{1}{2}}} \quad (6)$$

$$\tau_{yx} = \frac{K_{III}}{(2\pi x)^{\frac{1}{2}}} \sin[\gamma \ln(x/a) + \beta] \quad (7)$$

where γ is the imaginary part of the oscillatory stress singularity and β is a form factor. For the eight-node quadrilateral element used by Kuo and Wang [15] (Figs. 10 and 11), the values for γ and β were 1/2 and 1/4, respectively. The variables a and x are the crack length and element width, respectively. Very good agreement between their analysis and those of other references was reported as shown in Figs. 12 and 13.

Other investigators [15-19] have also used the same methods as Kuo and Wang [15] for the analysis of interfacial cracks in composites. Lakshminarayana, Murthy and Srinath [16] applied their analysis to laminated anisotropic cylindrical shells. Their numerical comparisons showed that the model will yield accurate stress intensity factors from a relatively coarse mesh. The mass and stiffness matrices for the laminated composites can be found in [16] or [17]. The finite element approach to analyze interlaminar stresses between composite laminae has proved to be quite accurate.

Ross, Malvern, Sierakowski, and Takeda [1] analyzed [0₅/90₅/0₅] glass/epoxy plates subjected to central localized impact. Their analysis was performed using the finite-element computer program SAPIV [20]. This program incorporated a three-dimensional elastic-orthotropic-material model with dynamic analysis capability that allows the calculation of transverse shear stresses directly.

The numerical results based on an impact velocity of 45.7 m/s are summarized in Figs. 14-17. The top interlaminar plane is the one closest to the impact side and the bottom interlaminar plane is the one farthest from the impact side. For an elastic solution, the shear stress τ_{xz} attains or exceeds the estimated interlaminar shear strength of 17.24 MPa at almost every station along the plane parallel to the x -axis (fiber direction of the top and bottom laminas) in both interlaminar planes, as shown in Figs. 14 and 15. The shear stress along the line at 90° to the top and bottom fiber direction exceeds the interlaminar shear strength only locally near the impact point, shown in Figs. 16 and 17. Their results were based upon elastic material

models that may prove useful in extending the analytical methodology to provide insight into incorporating failure models into the evaluative procedures.

C. Finite Element Analysis

There are many different computer codes presently available for calculating a dynamic response due to impact. Basically, there are two general classes of algorithms for dynamic problems: Lagrangian and Eulerian. Each has peculiar advantages and disadvantages for various problems. The primary advantage of Lagrangian codes is their ability to accurately track material boundaries and interfaces. They are ideally suited for constitutive models that require time histories of material behavior. Materials at an interface are designated as slave and master, and procedures are built into programs to permit contact, separation, and sliding, with or without friction, between master and slave surfaces. In contrast, Eulerian codes are ideally suited for treating large distortions. For problems in which large distortions predominate, an Eulerian description of material behavior is necessary. Early finite element three-dimensional computations were impractical from the standpoint of both cost and computer-storage capability. Hence, the pioneering solutions to impact problems were often obtained with two-dimensional Lagrangian codes, such as HEMP [21] and TOODY [21], and two-dimensional Eulerian codes, such as HELP [21]. The advent of third- and fourth-generation computers such as the CDC 7600 and CRAY machines has made three-dimensional computations feasible and attractive. Consequently, a number of computer programs capable of solving the fully three-dimensional equations of continuum physics were developed. Three-dimensional Lagrangian codes include EPIC-3 [22], HEMP3D [21], and DYNA3D. Some of the three-dimensional Eulerian codes are HULL, TRIOIL/TRIDORF, and METRIC [21].

In 1976, impacts of both a nickel cylinder and a nickel sphere onto an aluminum plate at 1500 m/s were performed by using a two-dimensional computer program, EPIC (Elastic-Plastic Impact Calculations) [23]. Johnson [23] reported that that a triangular element is better suited to represent severe distortions than a quadrilateral element because a triangle resists a node to cross the opposite side of the triangle during large distortion. For impact problems involving severe distortions, quadrilateral meshes become entangled and may take on shapes resulting in negative volumes, thus rendering computations useless.

One year later, in 1977, a three-dimensional code, EPIC-3, was developed for high velocity impact problems. It was successfully applied to normal impact of a nickel trun-

cated cone onto an aluminum plate of variable thickness at 1500 m/s and oblique impact of an aluminum rod onto a rigid surface at 1000 m/s. The formulation in EPIC-3 was derived for tetrahedral elements subjected to large strains and displacements [22]. In 1981, Hutchings et al. [24] assumed that a target is a rigid-plastic solid and a projectile is a rigid sphere. Their result provided a surprisingly successful explanation of the observed variation of crater volume and projectile energy loss with impact angle and velocity. For impact problems the impact force and duration are not easily determined. In 1985, two simple and improved models incorporating energy and mass balances were successfully developed to calculate impact force and duration during low-velocity impact of circular composite plates [25].

An explicit three-dimensional finite element code, (DYNA3D) developed by Lawrence Livermore National Laboratory, California was first released in 1976. The code has evolved considerably since 1976 and originated from the early finite element codes by Wilson [26] and HONDO [27]. The interface treatment for handling contact, sliding, and impact has been the most significant contribution of DYNA3D. The approach has proven useful in many applications, such as "Bar Impact on Rigid Wall" [28], "Impact of Cylinder into Rail" [29], and "Three-Dimensional Finite Element Impact Analysis of A Nuclear Waste Truck Cask" [30].

The above examples cited deal with dynamic impact problems using numerical methods of low-velocity impact or indentation of surfaces. The objective of this study is to combine finite element simulation with experimental composite material failures. In the past, these two disciplines have usually been treated as two separate branches of study. Hereby, a numerical finite element code, DYNA3D, has been employed to simulate the impact system and provide predictive post-impact information for future laboratory experimentation as well as real-time impact behavior. A large number of engineering problems, such as the one presented here, are too complex to be solved by closed-form analytical methods. For such problems, the finite element technique can be used to approximate the structural behavior during and after impact of solids onto composite materials.

D. Summary

The interlaminar fracture of composite materials has been extensively studied under low-velocity impact. From the results of impact studies, a generalized understanding of the complex behavior of multidirectional composites can be obtained. The study of these materials is complex and therefore requires some highly advanced method of obtaining

pertinent information such as: (1) What stresses cause fracture? and (2) How are these stresses related to the geometrical and physical properties of each laminae?

One method of obtaining information about this complex behavior is by a simple impact test. From this test, useful information concerning the transverse strain capability or stress capability of any material can be obtained. It has been shown that the impact behavior of composite materials is a function of laminae geometry and its properties. This will directly influence the stress distribution between each laminae under dynamic loading.

From calculated interlaminar stresses, failure criteria can be used to initiate a crack. Once the crack has been initiated, or if there is an existing crack, then the strain energy release rate or the stress-intensity factors can be compared to experimentally determined values as criteria for crack propagation. With the aid of an algorithm and an efficient model the stresses between each laminae can be found quite rapidly.

II. METHODOLOGY

A schematic of the impact system assumed in the numerical simulation is shown in Fig. 18. The schematic was selected for the analysis because the principal investigators have experimental data to compare with the results of the finite element analysis. The shaft rotates with a tangential velocity of 1000 rpm about the Z axis. A steel rod containing a diamond impacts the rotating shaft with a downward speed due to gravity loading. Although the shaft geometry is axisymmetric, the loading due to impact between the rotating shaft and the diamond head is not. Therefore, the problem is not amenable to a two-dimensional approach and must be solved with a three-dimensional model. An existing three-dimensional dynamic finite element structural analysis code, DYNA3D [6,7], was used to analyze the impact. From the analysis, a measure of anticipated surface area can be predicted and compared with that observed in the laboratory, to determine whether the computer model is correct.

A description of the computational process, which is employed herein for the impact simulation depicted in the previous section is shown in Figure 19. Programs were run on a Digital Equipment Corporation VAX 11/780 and the acquired VAX Station II/GPX computers. Two pre-processors, GMESH and TANVEL, were developed to prepare the information in a form usable by the main program, DYNA3D. Results of the computations typically contain physical quantities and material conditions throughout the physical domain as a function of time.

The resulting output files were generally too massive to read alphanumerically. Hence, TAURUS [31], a post-processor, provides graphical displays of items of interest. Each component of these tandem codes is described in more detail in this section.

An interactive program, named GMESH, was developed for the trial study to generate preliminary node and element data for input to the analysis code, because DYNA3D does not yet have significant mesh generation capabilities. The flowchart of GMESH, which is fully interactive, is shown in Figure 20. The program was designed for prismatic, circular shafts or cylinders. The longitudinal axis of the circular shaft was designated as the Z-direction. The number and relative location of nodes must be the same for each cross-section. On VAX computers running the VMS operating system the following commands were used to compile and link GMESH:

```
$ ASSIGN NODELE.DAT FOR006
$ ASSIGN TANVEL.DAT FOR007
$ FORTRAN GMESH
$ LINK GMESH
$ RUN GMESH
```

After executing the foregoing commands, a screen message prompts for input as shown in Figure 20. After finishing interactive responses to GMESH, two data files were created. One is NODELE.DAT, the node and element raw data for DYNA3D; the other is TANVEL.DAT, the input data for tangential velocity generation program TANVEL. The purpose of developing this tangential velocity generation routine will be stated below.

In this impact simulation both the diamond head (impactor) and the shaft (target) were in simultaneous motion: one linear, and the other rotational. Because the current version of DYNA3D does not allow direct input of the angular velocity of the rotating shaft, Hallquist [32] suggested that the angular velocity of the shaft be provided to DYNA3D by calculating the rotational tangential velocities of every nodal point on the shaft. A tangential velocity generation routine, TANVEL, was developed for this purpose. To execute TANVEL, the following commands were entered:

```
$ ASSIGN TANVEL.DAT FOR005
$ ASSIGN TANVEL.OUT FOR006
$ FORTRAN TANVEL
$ LINK TANVEL
$ RUN TANVEL
```

The commands then created an output file, TANVEL.OUT, containing the tangential velocities of every nodal point.

By concatenating NODELE.DAT and TANVEL.OUT into a single data file, DYNA3D.DAT, renders the input data for DYNA3D nearly ready. Although NODELE.DAT and TANVEL.OUT are in the form required for DYNA3D input instructions, certain items specific to the analysis were added. These include material property data, termination time for computations, initial velocity of the diamond head, and the sliding interface definitions.

The finite-element method models complicated problems in structural engineering and solid mechanics, with the resulting equations involving many thousands of degrees of freedom. Basically, the transient algorithms currently in use may be classified into two general classes: implicit and explicit [33]. Implicit algorithms tend to be numerically stable, permitting large time steps. However, the cost per step is high and storage requirements tend to increase dramatically with the size of the mesh. Explicit algorithms tend to be inexpensive per step and require less storage than implicit algorithms, but numerical stability requires that small steps be employed [34,35].

DYNA3D employs explicit algorithms to develop a three-dimensional finite element code whose equations are integrated by the central difference method. Hence, the time integration is only conditionally stable with respect to step size. During execution, DYNA3D continuously monitors the step size and adjusts it to keep the calculation stable. Fifteen material models are available in DYNA3D which cover a wide range of material behavior, such as elastic, kinematic/isotropic elastic-plastic, soil and crushable foam, thermo-elastic-plastic, rubber, temperature dependent elastic-plastic hydrodynamic, and so on [28].

According to the first few trial executions of DYNA3D, the rotating shaft, impacted by the diamond head, undergoes elastic-plastic deformations. Hence, material type 3, an elastic-plastic behavior with kinematic/isotropic work hardening, is exclusively used in this analysis. There are three types of sliding interfaces available in DYNA3D: sliding only, sliding-with-gaps, and tied. Because the diamond head rebounds from the shaft at the end of the impact, a sliding-with-gaps interface, in which the contact-impact algorithm employed by the code allows gaps to open or close, is used between the diamond head and rotating shaft [36].

For implementation of DYNA3D, one surface of the interface, is identified as a master surface (i.e. diamond head), which was more coarsely zoned, and the other was identified as a slave surface (i.e. rotating shaft). Each surface is

defined by a set of three or four node quadrilateral segments, called master and slave segments, on which the nodes of the slave and master surfaces, respectively, must slide. Time zero was defined as the instant of impact of the diamond head and the shaft.

The X-Y plane was the plane of symmetry with respect to the loading, so only one-half of the geometry in the positive Z-direction was actually modeled, as shown in Figs. 21 and 22. The diamond head was initially specified to have the velocity resulting from a gravity loading, which is 2.53 m/s in the negative Y-direction. The angular velocity of the shaft is input in terms of the rotational tangential velocity X- and Y-components at every nodal point, as previously described.

The command for executing DYNA3D was

```
$ RUN DYNA3D
      DYNA3D will prompt:
PLEASE DEFINE INPUT FILE NAMES OR CHANGE DEFAULTS:
```

Then, the following command

```
> DYNA3D I=DYNA3D
```

caused DYNA3D to execute, where I=DYNA3D means that the input filename was DYNA3D.DAT.

TAURUS, an interactive post-processor for DYNA3D, reads the output binary plotfiles generated by DYNA3D and plots contours, time histories and deformed shapes. TAURUS has three phases

```
Phase 0: initialization,
Phase 1: geometry display with contouring,
Phase 2: time history processing.
```

According to the termination time and time interval between complete state dumps in the input control card, DYNA3D generated several binary plotfiles under the names of D3PLOT.DAT, D3PLOT01.DAT, D3PLOT02.DAT, etc. On VAX computers, the command

```
$ RUN TAURUS
```

causes TAURUS to prompt:

```
PLEASE DEFINE INPUT FILE NAMES OR CHANGE DEFAULTS:
```

After this, the command

> TAURUS G=D3PLOT

allowed TAURUS to access all of the binary plotfiles and acted interactively, where G=D3PLOT defined that the binary plot filenames are D3PLOT.DAT, D3PLOT01.DAT, D3PLOT02.DAT, etc. The commands needed to effectively plot data are listed in Table 1.

Table 1: Phase 1 and Phase 2 Commands in TAURUS

Phase 1 Commands	Phase 2 Commands
CONTOUR	ASCL
DAM	ASET
DSF	ELEMENTS
M	ETIME
PHS2	GATHER
RAXY	GTIME
RAYZ	MATLS
RAZX	MTIME
RX	NODES
RY	NRTIME
RZ	NTIME
STATE	OSCL
TIME	OSET
TRIAD	PHS1
VIEW	PRINT
XSCALE	
YSCALE	
ZSCALE	

III. RESULTS AND DISCUSSION

The finite element mesh used in this simulation contains 1040 elements (1030 for the rotating shaft and 10 for the vertical steel rod containing the diamond tip, respectively) and 1339 nodes (1298 for the rotating shaft and 41 for the diamond head and attached vertical steel rod, respectively). Eight-node isoparametric solid elements were used for spatial discretization of the finite element mesh used in this simulation as shown in Figures 21 through 24. Figure 21 depicts a front wire-frame view of the impact system in the X-Y plane where the Z-axis goes directly into the paper and the origin is located at the center of the shaft. A side view is shown

in Figure 22. Instead of showing only one-half of the geometry of the system, Figs. 23 and 24 are two different angle views of the entire system.

Two primitive meshes in early simulations are shown in Figs. 24 and 25. In Figure 24, the entire mesh, containing 840 elements and 1155 nodes, is symmetrical about the longitudinal axis. The configuration was inefficient and costly in numerical computation, because deformations of the shaft from impact were not considered near the top surface. A finer mesh was developed for the vicinity of the diamond head, where the effect of impact is predominant, includes 870 elements and 1162 nodes as shown in Fig. 26. To reduce the amount of effort required to generate meshes, the interface treatment in DYNA3D permits sudden transitions in zoning with tied interfaces. The more coarsely meshed side of the interface is recommended as the master surface, and the finer meshed side as the slave surface. Each master node should coincide with a slave node to ensure complete displacement compatibility along the interface. As indicated in Figs. 25 and 26 these slave nodes do not coincide with master nodes between the interface. Hence, incompatible displacements exist along these interfaces. The total number of elements in Figs. 25 and 26 is much less than that of Fig. 21, which could save substantial computational cost. However, both meshes of Figs. 25 and 26 were not employed in the simulation because they would result in incompatible displacement of nodes as indicated in the figures.

An angular velocity of 1000 rpm (i.e. 105 rad/s in the negative Z-direction) is specified for the rotating shaft. The angular velocity was used for the tangential velocities at every nodal point in the shaft at time zero. The tangential velocity of each node obviously changes once the impact has started, but DYNA3D makes no provision for altering this velocity with time. Fortunately, the duration of impact was only 0.1 to 0.2 milliseconds, and it is assumed that the continuous change in velocities will not cause disastrous results for such a short response time. For the simulation, five loads of 35, 50, 85, 185, and 285 grams were applied to the diamond head for five executions.

A time history plot of mesh geometry was made to monitor the calculations and to determine that the diamond head has rebounded off of the shaft. For example, for an 85 gram applied load 105 microseconds elapsed before the diamond tip bounced from the surface. To ensure the impact event is completely finished, the total numerical simulation time was extended to about 200 micro-seconds, which requires approximately 45 hours of central processor unit time on a VAX 11/780 super-minicomputer. This results in a time step being used for this simulation of approximately 7.0×10^{-9} seconds. A

small time step was used because the minimum element dimension, which determines the critical time step size, was only 0.39 millimeters. The finer the mesh, the smaller the required time step size.

A sequence of deformed configurations is shown in Figures 27 through 32. As time progresses, indentation proceeds followed by rebounding as shown in Figs. 27 through 29 and Figs. 30 through 32, respectively. The vertical rod also undergoes some bending moment caused by frictional contact and shown in Figs. 29 through 32. Figure 33 shows another view of the mesh geometry at the end of impact. By using a nodal displacement magnification factor of ten, Fig. 34 provides a top view of the mesh geometry, which indicates an indented crater. A close-up view of the impact region of interest is shown in Fig. 35, where nodes and elements are numbered. At time zero node 101 on the shaft is directly impacted by node 1299, which is the diamond's lowermost point.

Time history plots of displacement, velocity, and acceleration in Y-direction (due to an 85-gram applied load) for nodes 1299 and 101 are shown in Figs. 36 through 38, respectively. Because the diamond and shaft interface allows slippage, nodes 1299 and 101 were not always in contact with each other. At the end of impact the Y-displacement curve tangent of node 101 approaches the horizon as a consequence of the plastic deformation. From Fig. 37, the terminal vertical component speeds of nodes 1299 and 101 are 0.9 and approximately 0.0 m/s, respectively. The nodes' accelerations oscillate near zero (i.e. no contact force) at the end of the response (Fig. 38), which means that the diamond head and rotating shaft have completely separated from each other.

The Y-displacement-time history for nodes 100, 101 and 102 representing the left node, impact node, and right node, are respectively shown in Fig. 39. The calculations show that the indenter causes the right node to form a ridge as expected as well as the left node.

The stress developed in the elements (841 and 851) sustaining impact are summarized in Figs. 40 through 49. The maximum and residual stresses of these two elements are also listed in Table 2. Normal yield stress for the shaft material is 35.0×10^7 Pa (see Section 3.3). The maximum Y-direction stresses of elements 841 and 851 are beyond this elastic limit, which causes severe plastic deformations, as shown in Table 2. As stated previously, the loading from impact of the diamond on the rotating shaft was not symmetrical. If the shaft (i.e. target) was not rotating, the time history plots of stresses for elements 841 and 851 would be the same (such as the similarity between Figures 42 and 43) or symmetrical with respect to the line of zero stress (Figures 46 and 49).

Because the shaft is rotating in the negative Z-direction, causing the diamond head (i.e. impactor) to slide toward element 851, the time history plots of the stresses for elements 841 and 851 are neither the same nor symmetrical with respect to the line of zero stress. The irregularity of stress time history between time zero and 5×10^{-5} seconds in Figures 40 through 49 is also caused by the rotation of the shaft.

Table 2: Maximum and Residual Stresses
for Elements 841 and 851

	Element 841		Element 851	
	Maximum	Residual	Maximum	Residual
	($\times 10^7$ Pa)	($\times 10^7$ Pa)	($\times 10^7$ Pa)	($\times 10^7$ Pa)
X	-33.00	-15.63	-32.20	-15.39
Y	-46.11	- 5.28	-46.67	- 5.83
Z	-31.80	-15.49	-32.47	-15.10
XY	+14.92	- 1.66	-14.66	+ 1.86
YZ	+14.65	- 3.65	+14.88	- 3.24
ZX	- 7.18	- 2.00	+ 6.55	+ 1.82

Figures 50 through 53 depict the time histories of effective plastic strain for elements 831, 841, 851, and 861, respectively. The plastic deformations of elements 831 and 861 are much smaller than those of elements 841 and 851. The time history plots of plastic strain states for elements other than 831, 841, 851, and 861 are all zero (not shown), which means that they are still within the elastic range after impact.

The foregoing data were based on a 85 gram applied load. Four other loads (35, 50, 185, and 285 grams) were also used for the simulation. Table 3 and Fig. 54 show the duration of impact versus applied static load. Since the duration of response is very short and not easily measured in the laboratory, the data was obtained from results of DYNA3D and not compared with experimental results. The heavier the load, the longer the duration of contact.

The scratches produced by impact have a characteristic sharp cut as the diamond head scribes the surface. This

gouging phenomenon pushes material toward one side of the scratch developing a ridge. The amount of ridging, which is taken to be the difference in height before and after being scribed by the diamond head, versus applied static load for nodes 100 and 102 (Fig. 35) is plotted in Fig. 55 and listed in Table 4. Ridging magnitudes at node 102 are greater than those of node 100 by approximately 3%. This is because the tangential velocity of the shaft is in the negative Z-direction which makes the diamond head pile more material toward node 102.

Table 3: Duration of Impact Versus
Applied Static Load

Applied Static Load (grams)	Duration of Impact (microseconds)
35	43
50	63
85	105
185	159
285	204

Table 4: Amount of Ridging at Nodes 100 and 102
Versus Applied Static Load

Applied Static Load (grams)	Ridging at Node 100 (micrometers)	Ridging at Node 102 (micrometers)
35	2.0619	2.1150
50	5.9120	6.2622
85	14.8192	15.2220
185	24.0882	24.8319
285	31.1080	31.9121

scratch areas were calculated from computer simulations. Their magnitudes versus applied static load were listed in Table 5.

Table 5: Actual and Simulation Scratch Area Versus Applied Static Load

Applied Static Load (grams)	Actual Scratch Area ($\times 10^{-4}$ cm ²)	Simulation Scratch Area ($\times 10^{-4}$ cm ²)
35	2.176	2.018
35	2.209	—
50	—	2.180
85	2.356	2.297
85	2.527	—
185	2.150	2.398
285	2.300	2.452

In Figure 56 the triangles represent scratch area data from computer simulations and the squares indicate experimental data. It should be noted that in computer simulation the initial conditions (such as initial velocity, point of impact, etc.) for each applied load would be exactly the same, whereas, in a laboratory environment they were performed manually. The maximum percent error between experiment and computer simulation of the scratch approximated 10%.

IV. SUMMARY OF FUTURE OBJECTIVES

The primary objective for the second year of the research program is to change the mesh to simulate a composite material. The mesh developed for the solid material was used to verify the results from the finite element analysis with experimental data. The next task of the research project is to configure a simple cylindrical mesh for a composite material. For example, a two ply composite will be modeled first and then more complicated structures will be configured by decreasing the shell thickness and increasing the number of plies.

Once the model has been constructed, it will be fine-tuned by comparing it with experimental results. The simulation of the multidirectional composite to low velocity impact will proceed at a steady rate. The results obtained from this stage of the project will be important for understanding the unseen damage of delamination in multidirectional composites when impacted by a foreign object at low velocities.

V. REFERENCES

1. Ross, C. A., Malvern, L. E., Sierakowski, R. L., and Takeda, N., "Finite-Element Analysis of Interlaminar Shear Stresses Due to Local Impact," Recent Advances in Composites in the United States and Japan, ASTM STP 864, J. R. Vinson and M. Taya, Eds., American Society for Testing and Materials, Philadelphia, pp. 355-367, 1985.
2. Ko, F. K. and Hartman, D., "Impact Behavior of 2-D and 3-D Glass/Epoxy Composites," Sampe Journal, No. 7-8, pp. 26-50, 1986.
3. Bowles, K. J., "The Correlation of Low-Velocity Impact Resistance of Graphite-Fiber-Reinforced Composite with Matrix Properties," NASA TM-87337, NASA Lewis Research Center, Cleveland, Ohio, 1986.
4. Greszczuk, L. B., "Damage in Composite Materials Due to Low-Velocity Impact," Impact Dynamics, John Wiley and Sons, Inc., New York, NY, 1982.
5. Shivakumar, K. N. Elber, W., and Illg, W., "Prediction of Low-Velocity Damage in Thin Circular Laminates," AIAA Journal, Vol. 23, No. 14, pp. 442-449, 1985.
6. Tsai, S. W. and Hahn, H. T., Introduction to Composite Materials, Technomic, Westport, Conn., 1980.
7. Jones, R. M., Mechanics of Materials, McGraw-Hill Book Co., New York, 1975.
8. Sankar, B. V., and Sun, C. T., "Low-Velocity Impact Damage in Graphite-Epoxy Laminates Subjected to Tensile Initial Stresses," AIAA Journal, Vol. 24, No. 3, pp. 470-471, 1986.
9. Mahishi, J. M. and Adams, D. F., "Energy Release Rate During Delamination Crack Growth in Notched Composite Laminates," Delamination and Debonding of Materials, ASTM STP 876, W. S. Johnson, Ed., American Society for Testing and Materials, Philadelphia, pp. 95-111, 1985.
10. Monib, M. M. and Adams, D. F., Report UWME-DR-001-102-1, University of Wyoming, Laramie, 1980.
11. Ramkumar, R. L., NASA-CR 166046, Northrop Corp. Hawthorne, CA, March 1983.
12. Joshi, S. P. and Sun, C. T., "Impact Induced Fracture in a Laminated Composite," Journal of Composite Materials, Vol. 19, No. 1, pp. 51-66, 1985.

13. Barsom, J. M. and Rolfe, S. T., *Fracture and Fatigue Control in Structures*, Prentice-Hall, Englewood Cliffs, New Jersey, 1987.
14. Pipes, R. B. and Pagano, N. J., "Interlaminar Stresses in Composite Laminates under Uniform Axial Extension, *Journal of Composite Materials*, Vol. 4, pp. 538-548, 1970.
15. Kuo, An-Yu and Wang, Su-Su, "A Dynamic Hybrid Finite-Element Analysis for Interfacial Cracks in Composites," *Delamination and Debonding of Materials*, ASTM STP 876, W. S. Johnson, Ed., American Society for Testing and Materials, Philadelphia, pp. 5-34, 1985.
16. Lakshminarayana, H. V., Murthy, M. V. V., and Srinath, L. S., "On a Finite Element Model for the Analysis of Through Cracks in Laminated Anisotropic Cylindrical Shells," *Engineering Fracture Mechanics*, Vol. 14, No. 4, pp. 697-712, 1981.
17. Lee, J. D., "Three Dimensional Finite Element Analysis of Damage Accumulation in Composite Laminate," *Computers and Structures*, Vol. 15, No. 3, PP. 335-350, 1981.
18. Lee, J. D., Du, S., and Liebowitz, H., "Three-Dimensional Finite Element and Dynamic Analysis of Composite Laminate Subjected to Impact," *Computers and Structures*, Vol. 19, No.5-6, pp. 807-813, 1984.
19. Lee, S. W. and Pian, T. H. H., "Improvement of Plate and Shell Finite Elements by Mixed Formulations," *AIAA Journal*, Vol. 16, No. 1, pp. 29-34, 1978.
20. Bathe, K. J., Wilson, E. L., and Iding, R. H., "NONSAP: A Structural Analysis Program for Static and Dynamic Response of Nonlinear Systems," Report No. UCSESM 74-3, College of Engineering, University of California, Berkeley, CA, 1974.
21. Zukas, J. A., Nicholas, T., Swift, H. F., Greszczuk, L. B., and Curran, D. R., *Impact Dynamics*, John Wiley & Sons, Inc., New York, NY, 1982.
22. Johnson, G. R., "High Velocity Impact Calculations in Three Dimensions," *Journal of Applied Mechanics*, pp. 95-100, March, 1977.
23. Johnson, G. R., "Analysis of Elastic-Plastic Impact Involving Severe Distortions," *Journal of Applied Mechanics*, pp. 439-443, September, 1976.
24. Hutchings, I. M., Macmillan, N. H., and Rickerby, D. G., "Further Studies of the Oblique Impact of a Hard Sphere

- Against a Ductile Solid," International Journal of Mechanical Sciences, Vol. 23, No. 11, pp. 639-646, 1981.
25. Shivakumar, K. N., Elber, W., and Illg, W., "Prediction of Impact Force and Duration Due to Low-Velocity Impact on Circular Composite Laminates," Journal of Applied Mechanics, Vol. 52, pp. 674-680, September, 1985.
 26. Wilson, E. L., and Farhoomand, I., "A Nonlinear Finite Element Code for Analyzing the Blast Response of Underground Structures," N-70-1, U. S. Army Waterways Experiment Station, 1970.
 27. Key, S. W., Beisinger, Z. E., and Krieg, R. D., "HONDO II - A Finite Element Computer Program for the Large Deformation Dynamic Response of Axisymmetric Solids," SAND78-0422, Sandia Laboratories, Albuquerque, NM, October, 1978.
 28. Hallquist, J. O., "DYNA3D User's Manual (Nonlinear Dynamic Analysis of Solids in Three Dimensions)," UCID-19156, Lawrence Livermore National Laboratory, Livermore, CA, July, 1981.
 29. Benson, D. J., and Hallquist, J. O., "A Simple Rigid Body Algorithm for Structural Dynamics Programs," International Journal for Numerical Methods in Engineering, Vol. 22, pp. 723-749, 1986.
 30. Miller, J. D., "Three-Dimensional Finite Element Impact Analysis of a Nuclear Waste Truck Cask," SAND84-1899, Sandia Laboratories, Albuquerque, NM, May, 1985.
 31. Brown, B. E., and Hallquist, J. O., "TAURUS: An Interactive Post-Processor for the Analysis Codes NIKE3D, DYNA3D, TACO3D, and GEMINI," UCID-19392, Lawrence Livermore National Laboratory, Livermore, CA, 1982.
 32. Hallquist, J. O., Personal communication via telephone, April 16, 1986.
 33. Hughes, T. J. R., and Liu, W. K., "Implicit-Explicit Finite Elements in Transient Analysis: Implementation and Numerical Examples," Journal of Applied Mechanics, Vol. 45, pp. 375-378, June, 1978.
 34. Hughes, T. J. R., and Liu, W. K., "Implicit-Explicit Finite Elements in Transient Analysis: Stability Theory," Journal of Applied Mechanics, Vol. 45, pp. 371-374, June, 1978.
 35. Key, S. W., "Transient Response by Time Integration: Review of Implicit and Explicit Operators," Advanced Structural Dynamics, Applied Science Publishers, Ltd., England, 1980.

36. Hallquist, J. O., "Theoretical Manual for DYNA3D," UCID-19401, Lawrence Livermore National Laboratory, Livermore, CA, 1982.

LIST OF FIGURES

- Figure 1: The three basic modes of crack surface displacements: Mode I, Mode II, and Mode III (Ref. 13).
- Figure 2: The three major steps in studying the response of composite materials to low velocity impact (Ref. 4).
- Figure 3: C-Scan digital output of a multidirectional composite after low-velocity impact. The impact velocity was in the range of 10-40 m/s (Ref.8).
- Figure 4: 80x magnification of a shear crack of an impact loaded, Hercules AS4/3501-6 graphite epoxy plate (Ref. 11).
- Figure 5: Finite element mesh and through-the-thickness stress output locations along X-axis. Center of impact point is located at the origin and a semicircular spread of the load within the contact region is shown (Ref. 12).
- Figure 6: Shear stress distribution in [90/0/90] lay-up. Refer to Fig. 5 for z/t position, where t is the thickness of the plate and q_0 (GPa) is the applied load (Ref.12).
- Figure 7: Shear stress distribution in [0/90/0] lay-up (Ref. 12).
- Figure 8: Transverse normal stress distribution in [90/0/90] lay-up (Ref. 12).
- Figure 9: Flexural stress distribution in [0/90/0] lay-up (Ref. 12).
- Figure 10: Finite element mesh of a partially closed crack with A_c as the end point of the closure region S_c . The hybrid element for a closed crack is placed at the crack tip. Eight-node isoparametric elements for anisotropic materials are located around the crack-tip element (Ref. 15).
- Figure 11: An open interfacial crack subject to point loads at mid-crack surface (Ref. 15).
- Figure 12: Dynamic stress-intensity factors of Mode I delamination (Ref. 21).
- Figure 13: Dynamic stress-intensity factors of Mode III delamination (Ref. 21).

- Figure 14: Shear stress τ_{xz} , τ_{yz} , top interlaminar plane versus time. Stresses for locations A to G parallel to x-axis (Ref. 1).
- Figure 15: Shear stress τ_{xz} , τ_{yz} , bottom interlaminar plane versus time. Stresses for locations A to G parallel to x-axis (Ref. 1).
- Figure 16: Shear stress τ_{xz} , τ_{yz} , top interlaminar plane versus time. Stresses for locations A to G parallel to y-axis (Ref. 1).
- Figure 17: Shear stress τ_{xz} , τ_{yz} , bottom interlaminar plane versus time. Stresses for locations A to G parallel to y-axis (Ref. 1).
- Figure 18: Schematic view of apparatus for experimental impact of rotating shaft.
- Figure 19: Flowchart of Computational Process
- Figure 20: Flowchart of GMESH Program
- Figure 21: Front View of One-Half Mesh Geometry
- Figure 22: Side View of One-Half Mesh Geometry
- Figure 23: Side View of Entire Mesh Geometry
- Figure 24: 45° View of Entire Mesh Geometry
- Figure 25: Former Symmetrical Mesh Geometry
- Figure 26: Former Mesh Geometry
- Figure 27: Mesh Geometry at 12 Micro-Seconds After Initial Impact of Diamond on Rotating Shaft
- Figure 28: Mesh Geometry at 27 Micro-Seconds After Initial Impact of Diamond on Rotating Shaft
- Figure 29: Mesh Geometry at 117 Micro-Seconds
- Figure 30: Mesh Geometry at 132 Micro-Seconds at Which Rebounding Begins
- Figure 31: Mesh Geometry at 147 Micro-Seconds at Which Rebounding Continues
- Figure 32: Mesh Geometry at 198 Micro-Seconds Showing Indented Crater and Bending Of Indentor

- Figure 33: 50° View of Mesh Geometry at 198 Micro-Seconds
- Figure 34: Top View of Entire Mesh Geometry With Indented Crater at 198 Micro-Seconds
- Figure 35: Close-up View of the Impact Region of Interest With Numbered Nodes and Elements
- Figure 36: Y-Displacement vs. Time at Nodes 1299 and 101
- Figure 37: Y-Velocity vs. Time at Nodes 1299 and 101
- Figure 38: Y-Acceleration vs. Time at Nodes 1299 and 101
- Figure 39: Y-Displacement vs. Time at Nodes 100, 101, and 102
- Figure 40: X-Stress vs. Time for Element 841
- Figure 41: X-Stress vs. Time for Element 851
- Figure 42: Y-Stress vs. Time for Element 841
- Figure 43: Y-Stress vs. Time for Element 851
- Figure 44: Z-Stress vs. Time for Element 841
- Figure 45: Z-Stress vs. Time for Element 851
- Figure 46: XY-Shear Stress vs. Time for Elements 841 and 851
- Figure 47: YZ-Shear Stress vs. Time for Element 841
- Figure 48: YZ-Shear Stress vs. Time for Element 851
- Figure 49: ZX-Shear Stress vs. Time for Elements 841 and 851
- Figure 50: Effective Plastic Strain vs. Time For Element 831
- Figure 51: Effective Plastic Strain vs. Time For Element 841
- Figure 52: Effective Plastic Strain vs. Time For Element 851
- Figure 53: Effective Plastic Strain vs. Time For Element 861
- Figure 54: Duration of Impact vs. Applied Static Load
- Figure 55: Amount of Ridging at Nodes 100 and 102 vs. Applied Static Load
- Figure 56: Comparison of the scratch area calculated by using DYNA3D and measured optically.

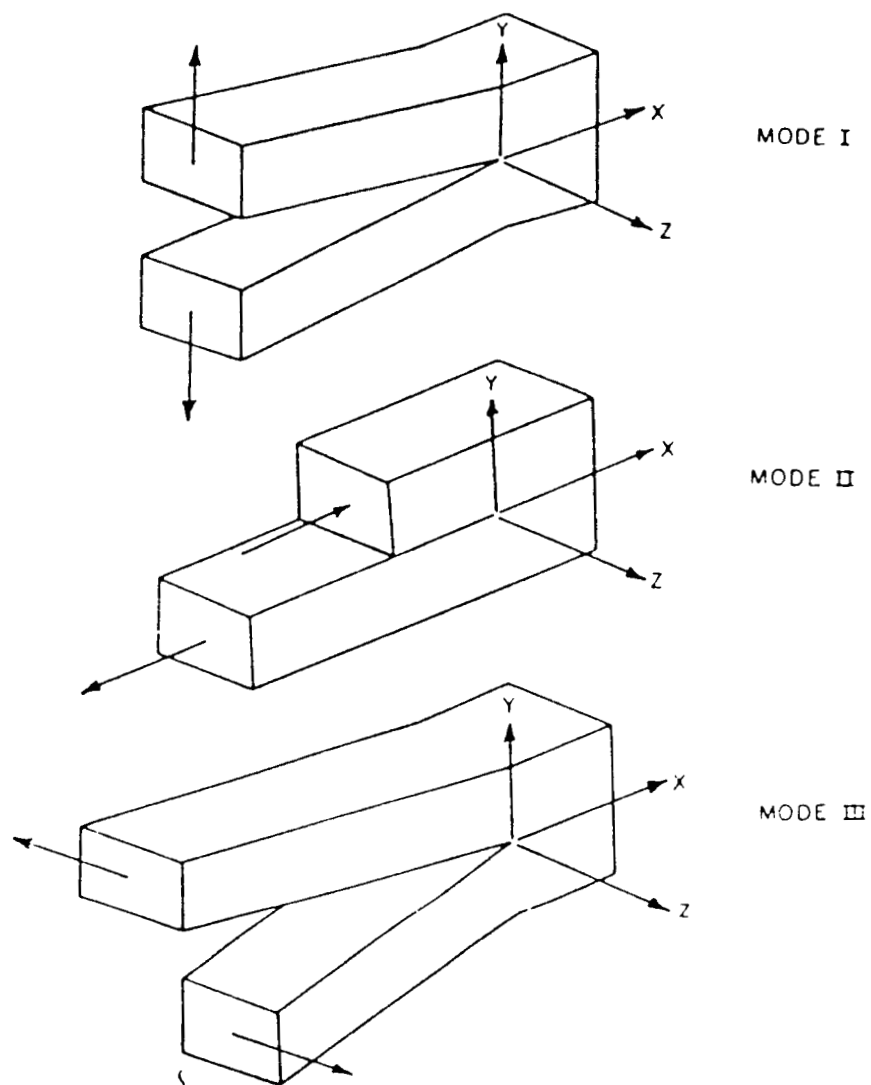


Figure 1. The three basic modes of crack surface displacements: Mode I, Mode II, and Mode III (Ref. 13).

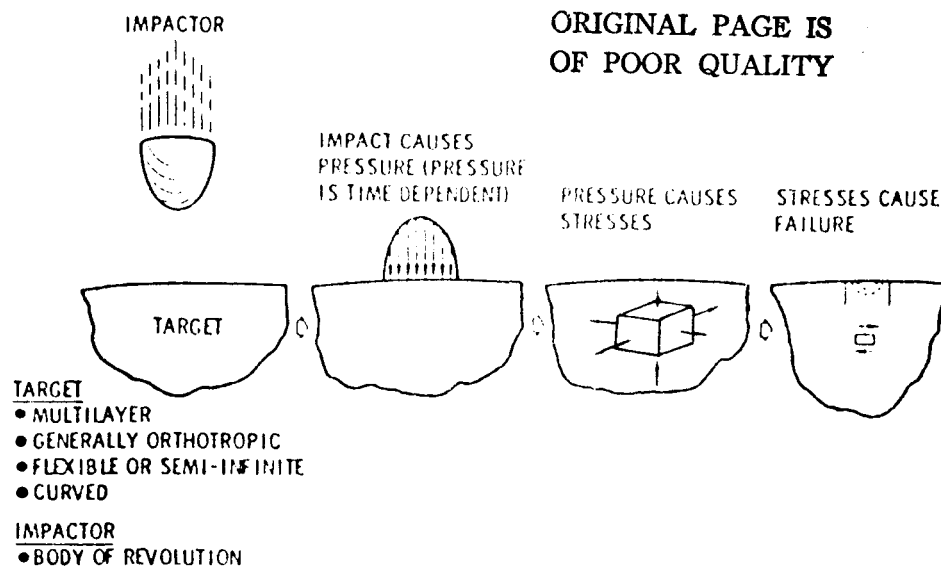


Figure 2. The three major steps in studying the response of composite materials to low velocity impact (Ref. 4).

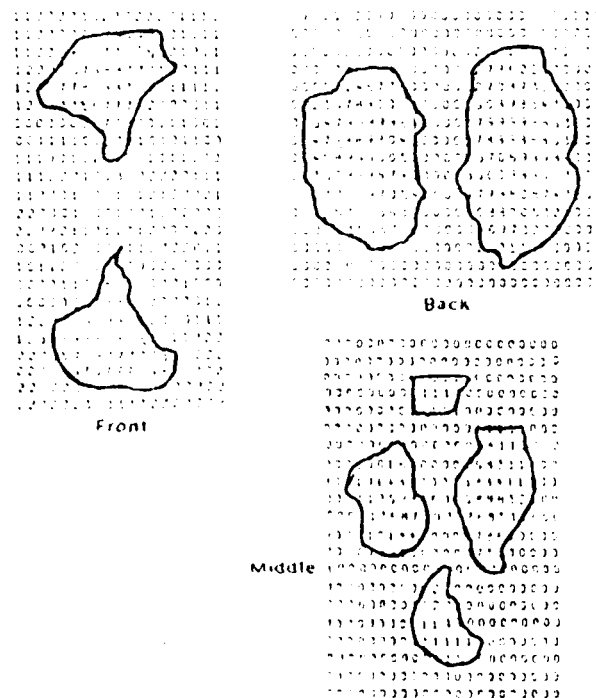


Figure 3. C-scan digital output of a multidirectional composite after low-velocity impact. The impact velocity was in the range of 10-40 m/s (Ref. 8).

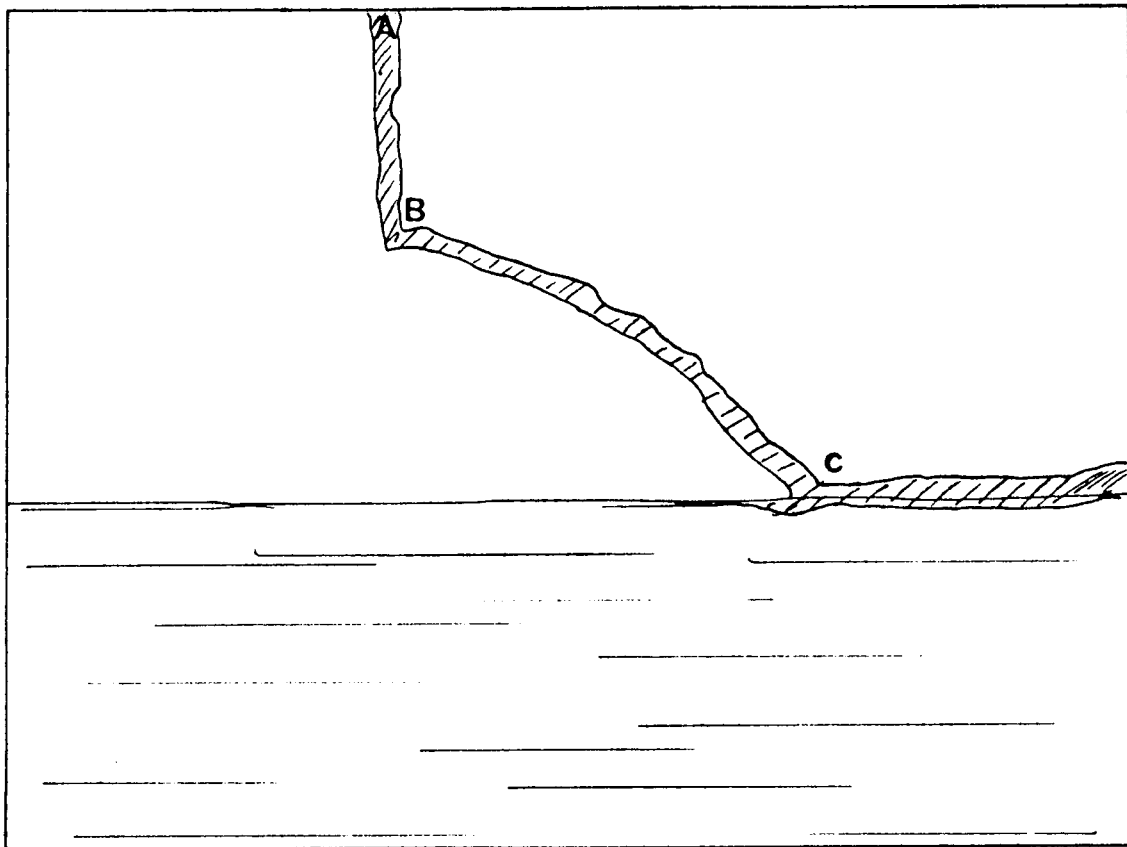


Figure 4. 80x magnification of a shear crack of an impact loaded, Hercules AS4/3501-6 graphite epoxy plate (Ref. 11).

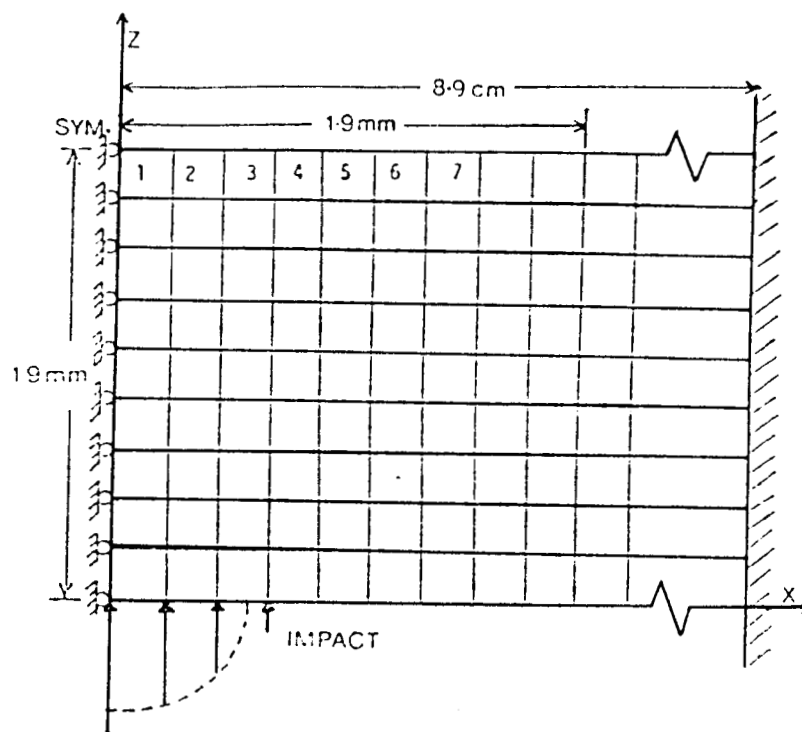


Figure 5. Finite element mesh and through-the-thickness stress output locations along X-axis. Center of impact point is located at the origin and a semicircular spread of the load within the contact region is shown (Ref. 12).

ORIGINAL PAGE IS
OF POOR QUALITY

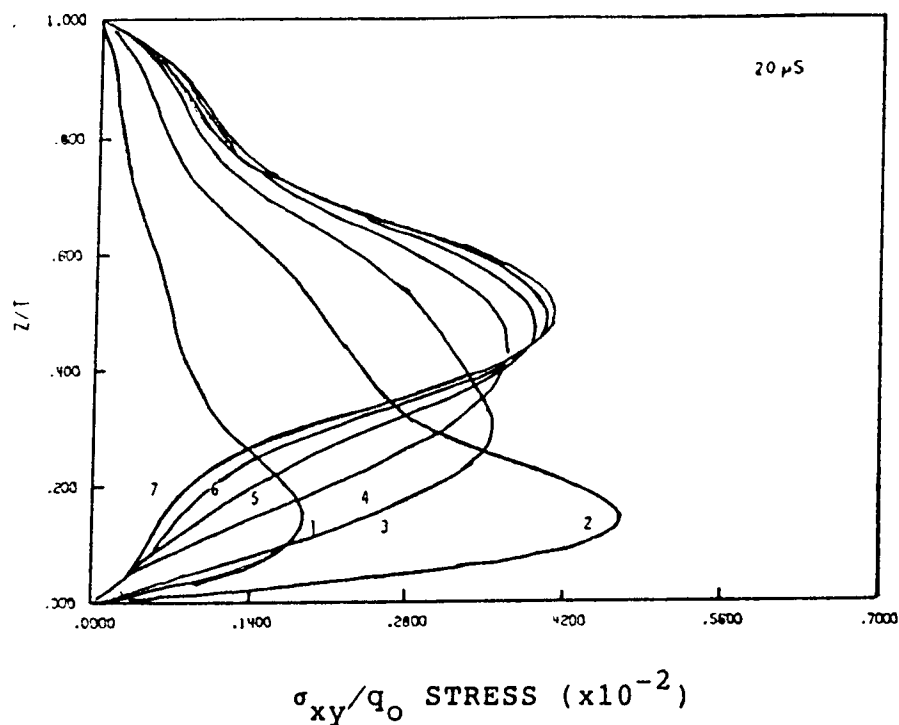


Figure 6. Shear stress distribution in [90/0/90] lay-up. Refer to Fig. 5 for z/t position, where t is the thickness of the plate and q_0 (GPa) is the applied load (Ref. 12).

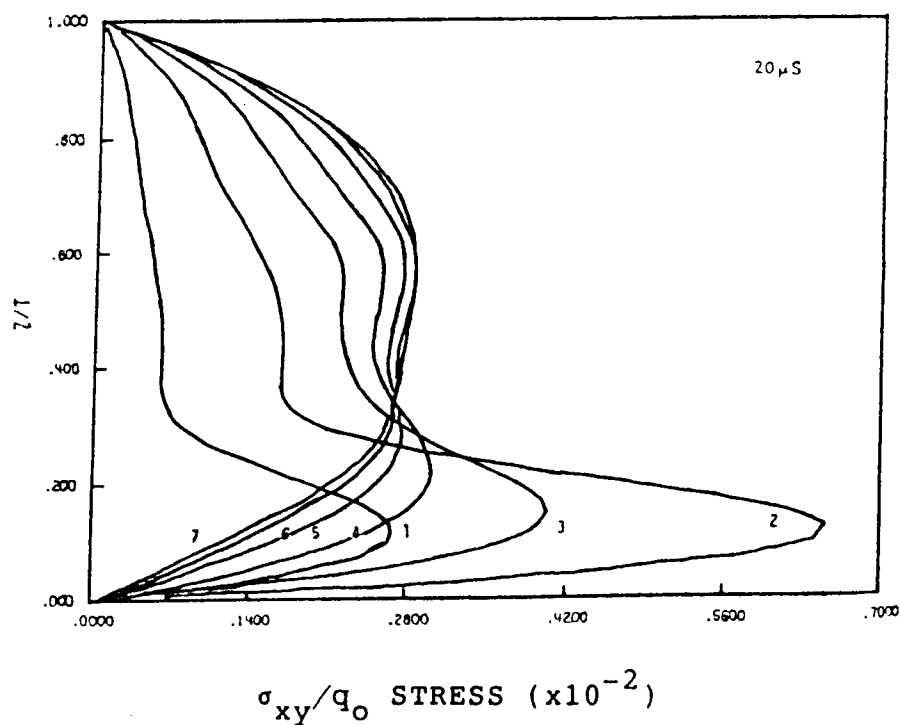


Figure 7. Shear stress distribution in [0/90/0] lay-up (Ref. 12).

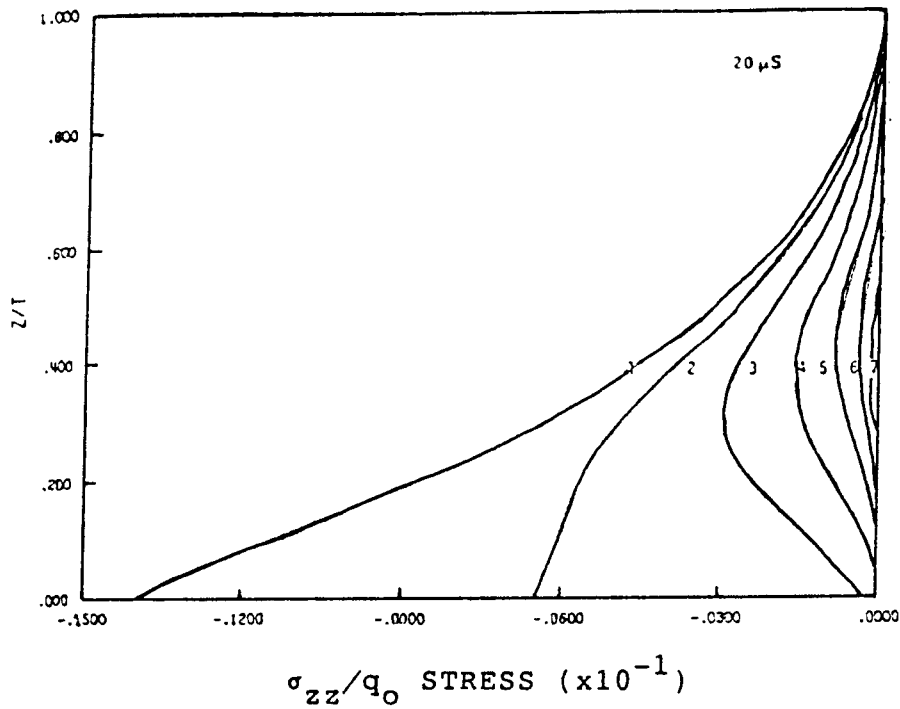


Figure 8. Transverse normal stress distribution in [90/0/90] lay-up (Ref. 12).

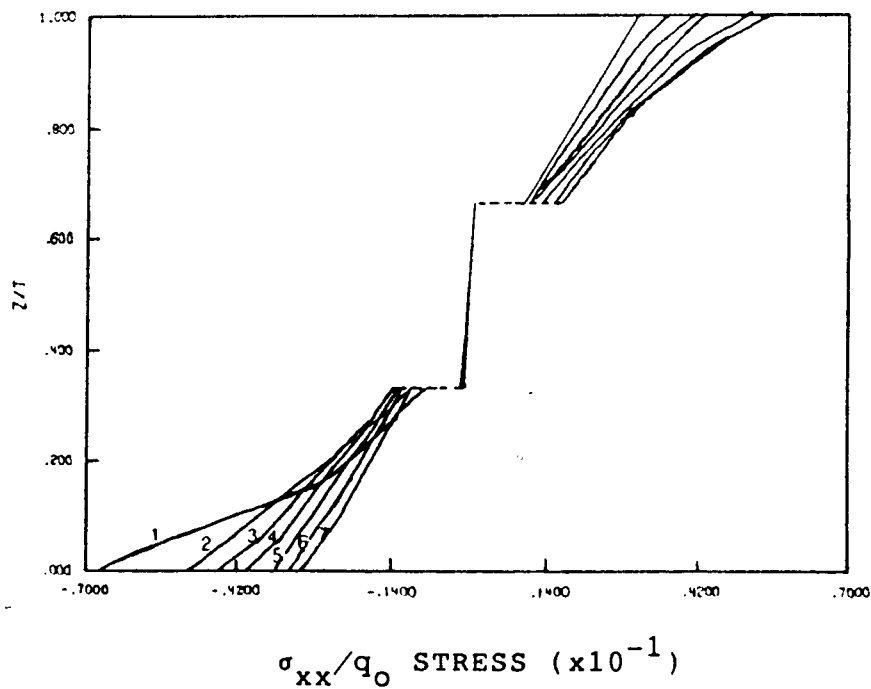


Figure 9. Flexural stress distribution in [0/90/0] lay-up (Ref. 12.).

ORIGINAL PAGE IS
OF POOR QUALITY

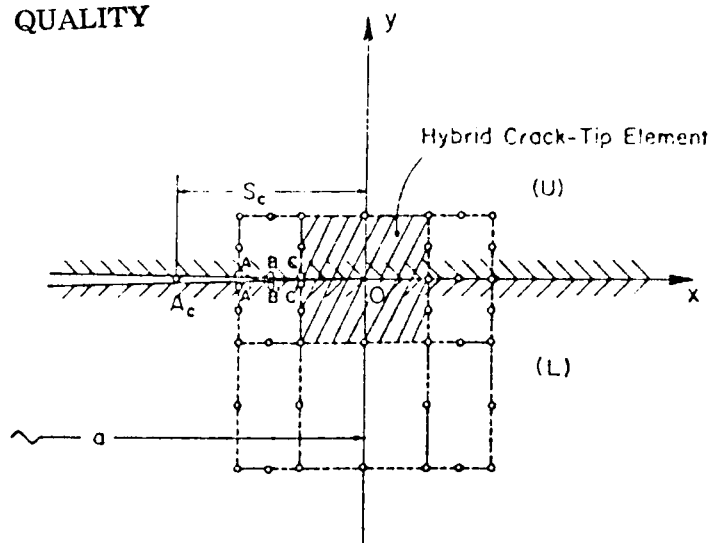


Figure 10. Finite element mesh of a partially closed crack with A_c as the end point of the closure region S_c . The hybrid element for a closed crack is placed at the crack tip. Eight-node isoparametric elements for anisotropic materials are located around the crack-tip element (Ref. 15).

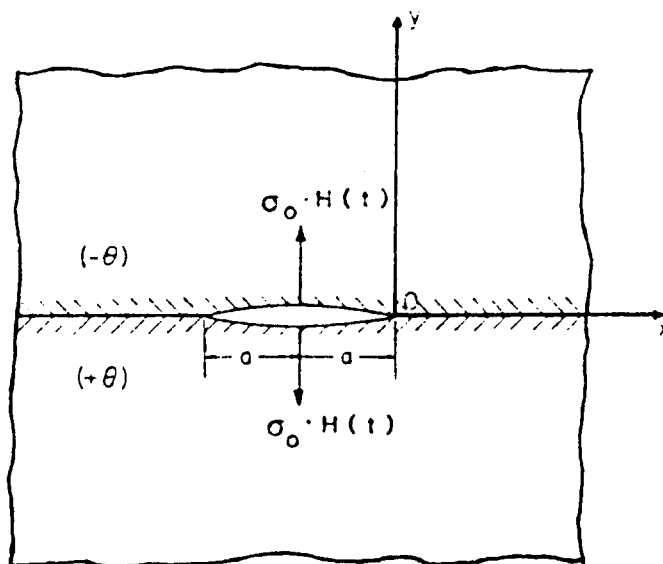


Figure 11. An open interfacial crack subject to point loads at mid-crack surface (Ref. 15).

ORIGINAL PAGE IS
OF POOR QUALITY

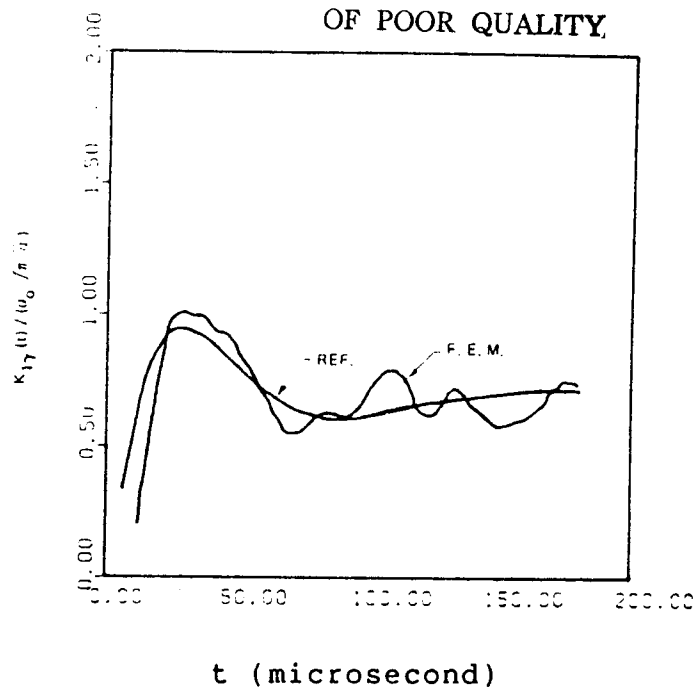


Figure 12. Dynamic stress-intensity factors of Mode I delamination (Ref. 21).

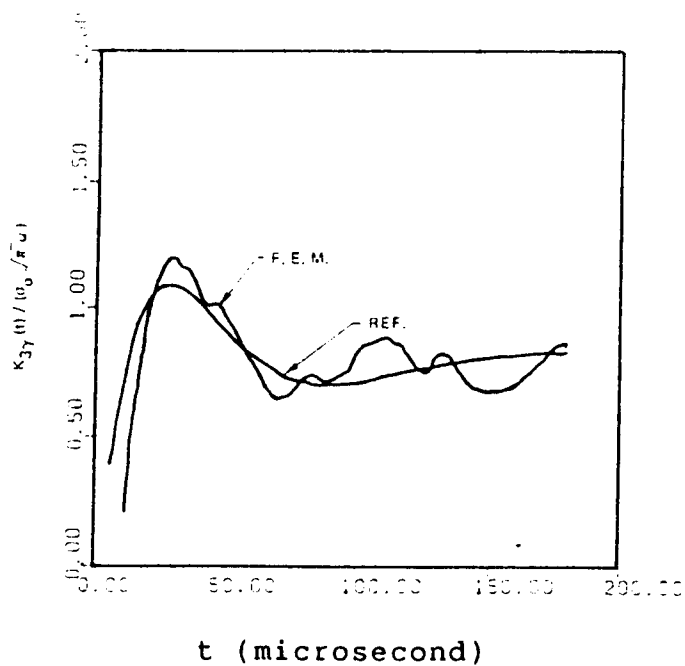


Figure 13. Dynamic stress-intensity factors of Mode III delamination (Ref. 21).

ORIGINAL PAGE IS
OF POOR QUALITY

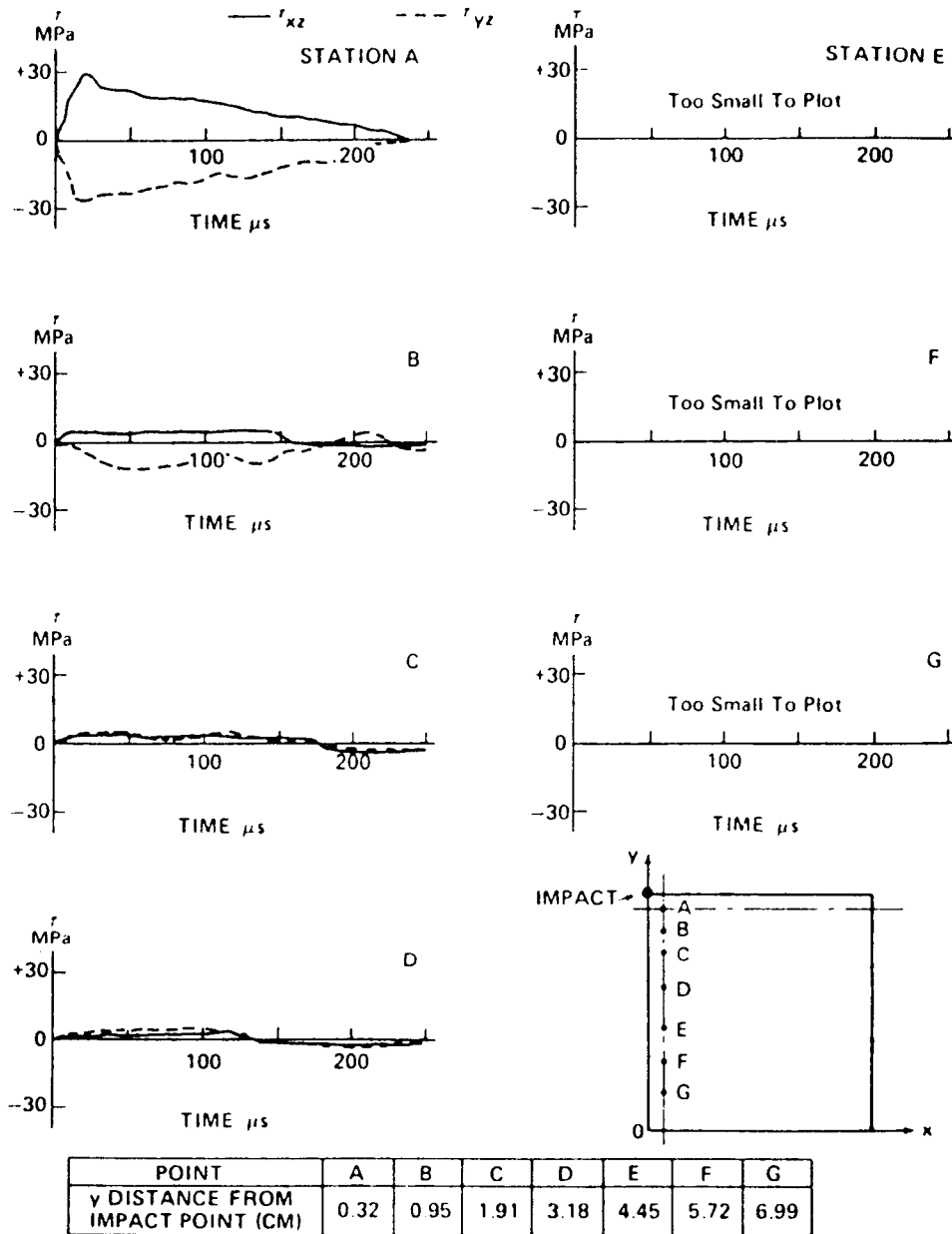
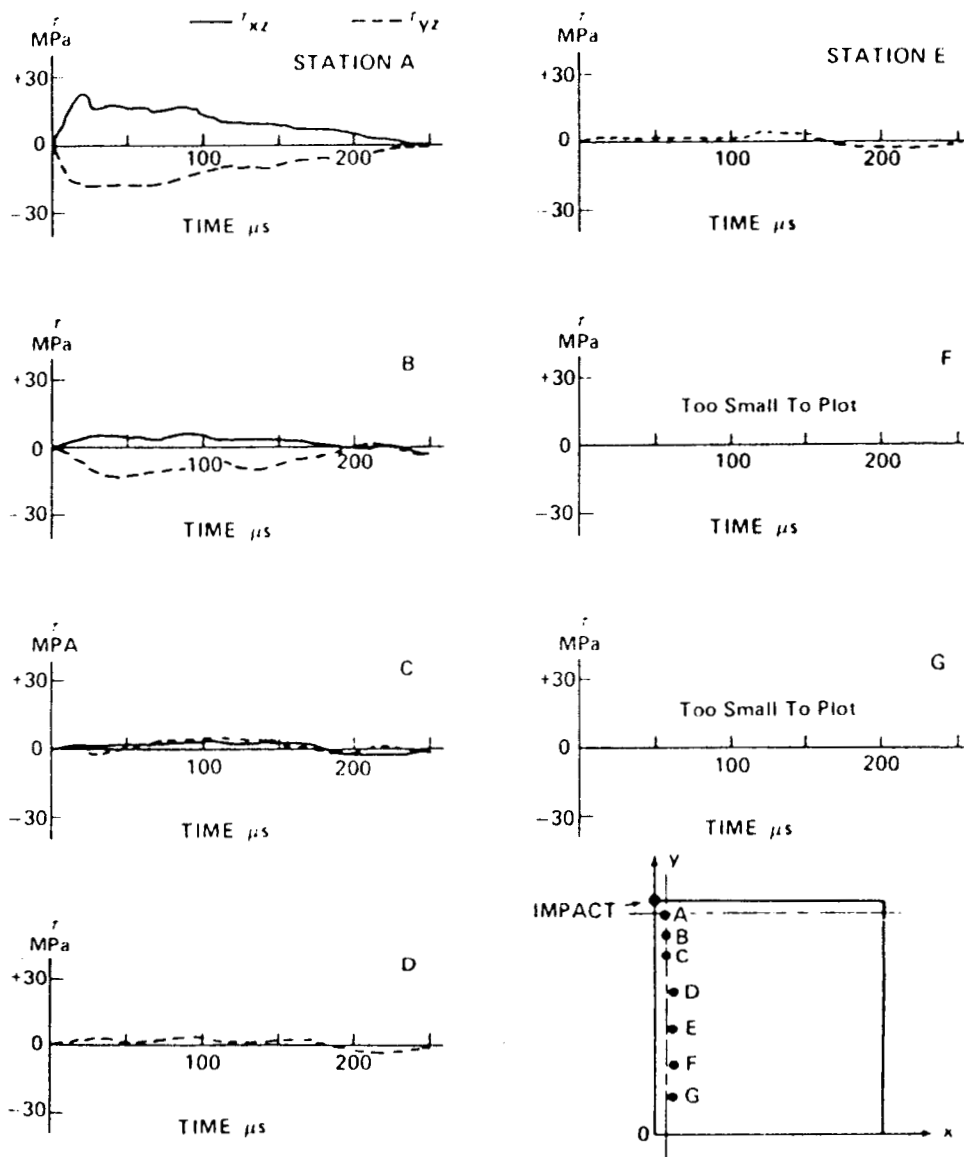


Figure 14. Shear stress τ_{xz} , τ_{yz} , top interlaminar plane versus time. Stresses for locations A to G parallel to x-axis (Ref. 1).



POINT	A	B	C	D	E	F	G
y DISTANCE FROM IMPACT POINT (CM)	0.32	0.95	1.91	3.18	4.45	5.72	6.99

Figure 15. Shear stress τ_{xz} , τ_{yz} , bottom interlaminar plane versus time. Stresses for locations A to G parallel to x-axis (Ref. 1).

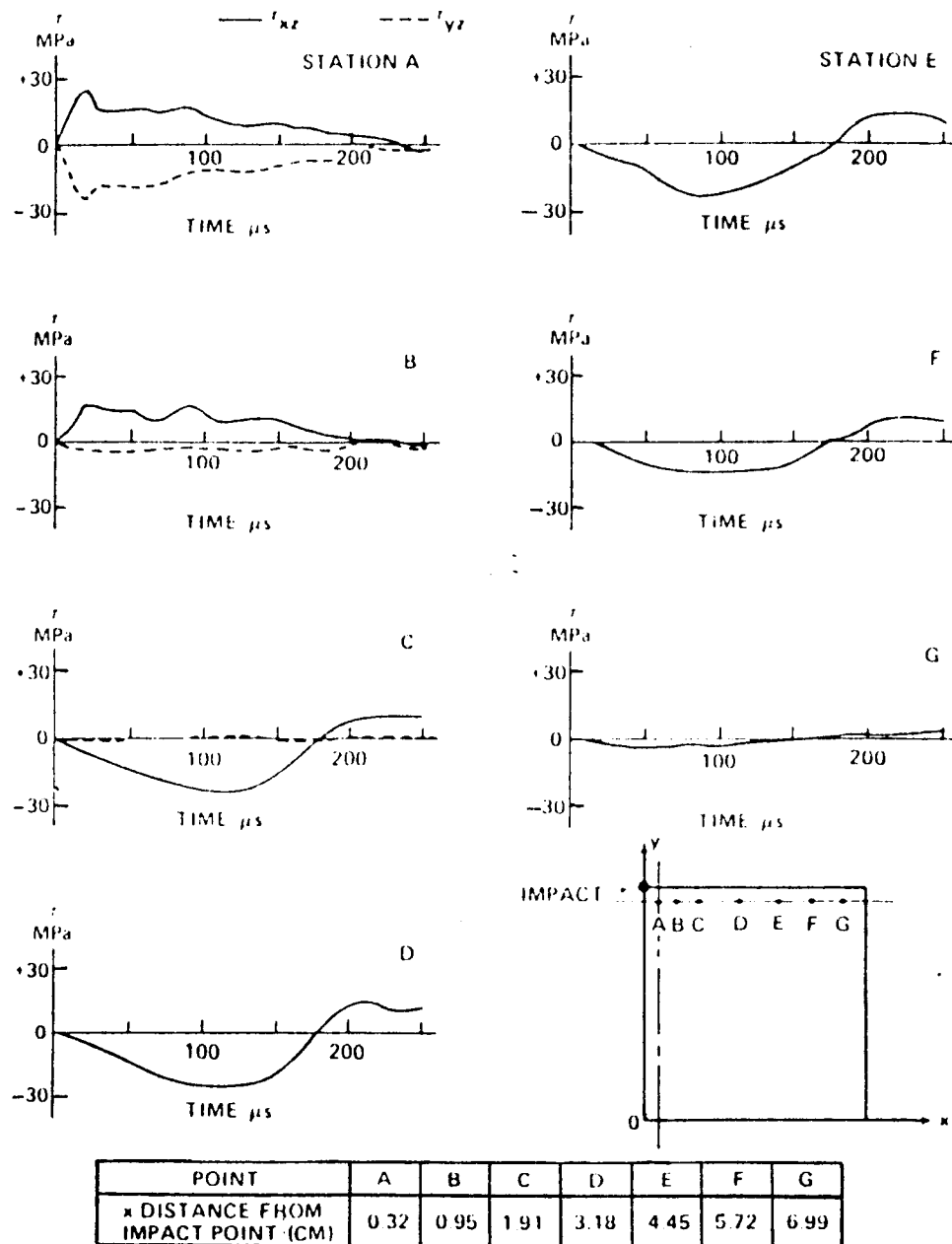


Figure 16. Shear stress τ_{xz} , τ_{yz} , top interlaminar plane versus time. Stresses for locations A to G parallel to y-axis (Ref. 1).

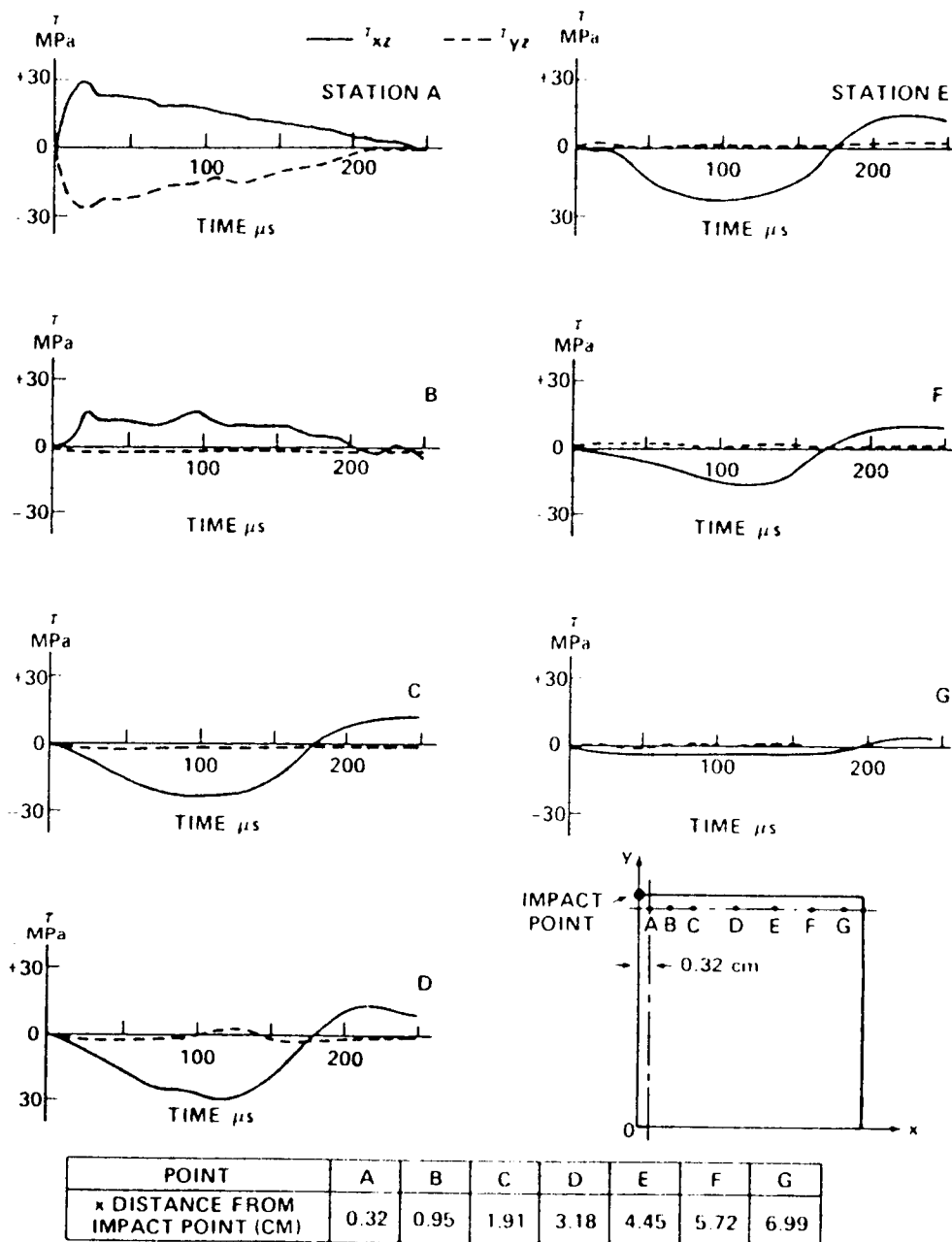


Figure 17. Shear stress τ_{xz} , τ_{yz} , bottom interlaminar plane versus time. Stresses for locations A to G parallel to y-axis (Ref. 1).

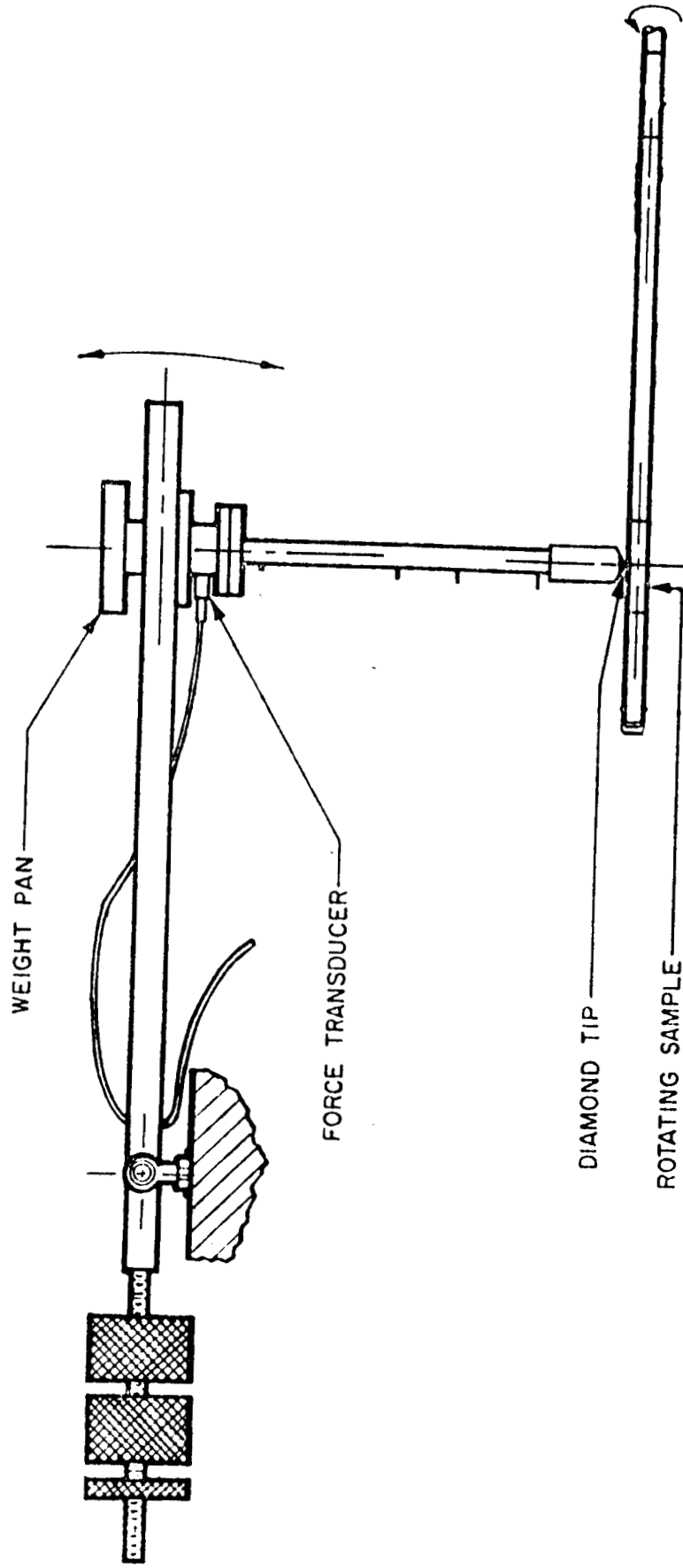


Figure 18. Schematic view of apparatus for experimental impact of rotating shaft.

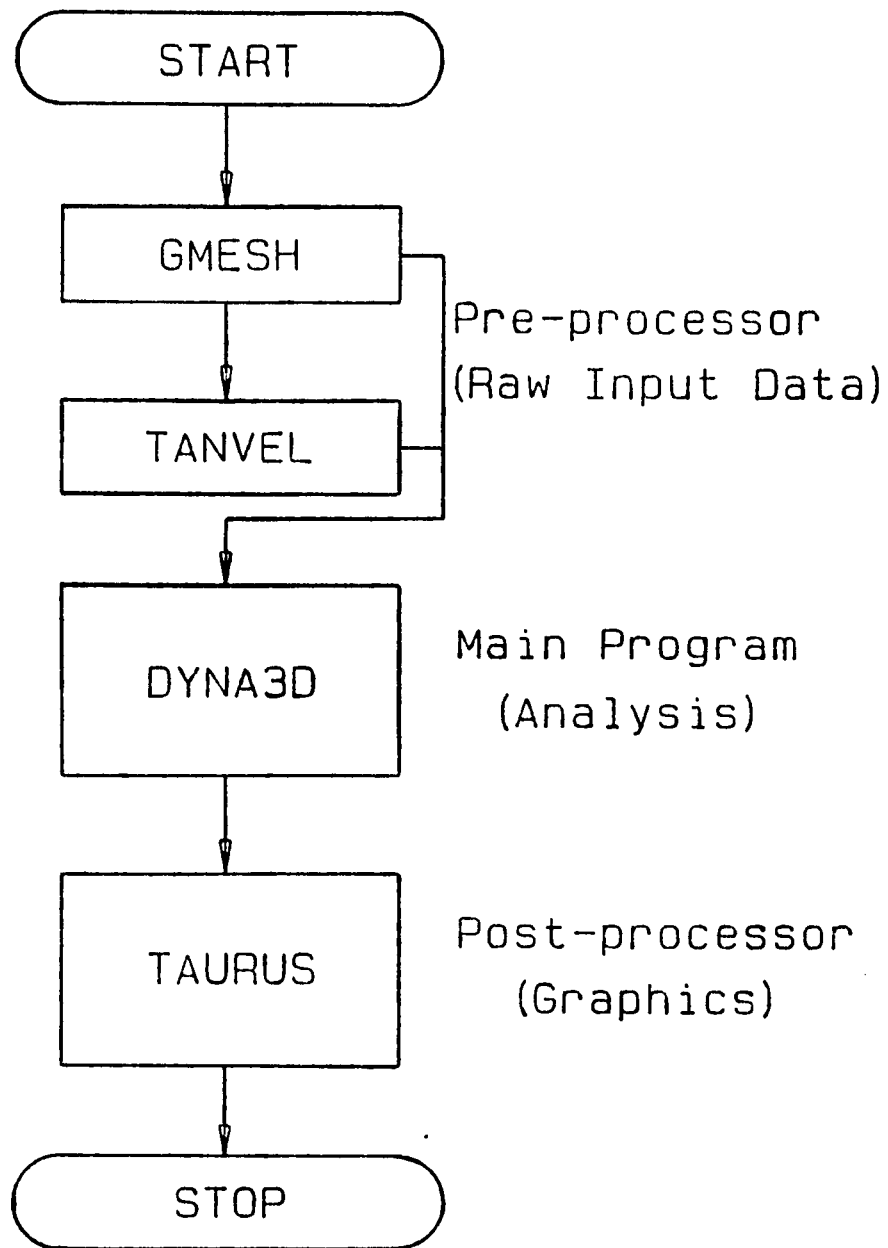


Figure 19: Flowchart of Computational Process

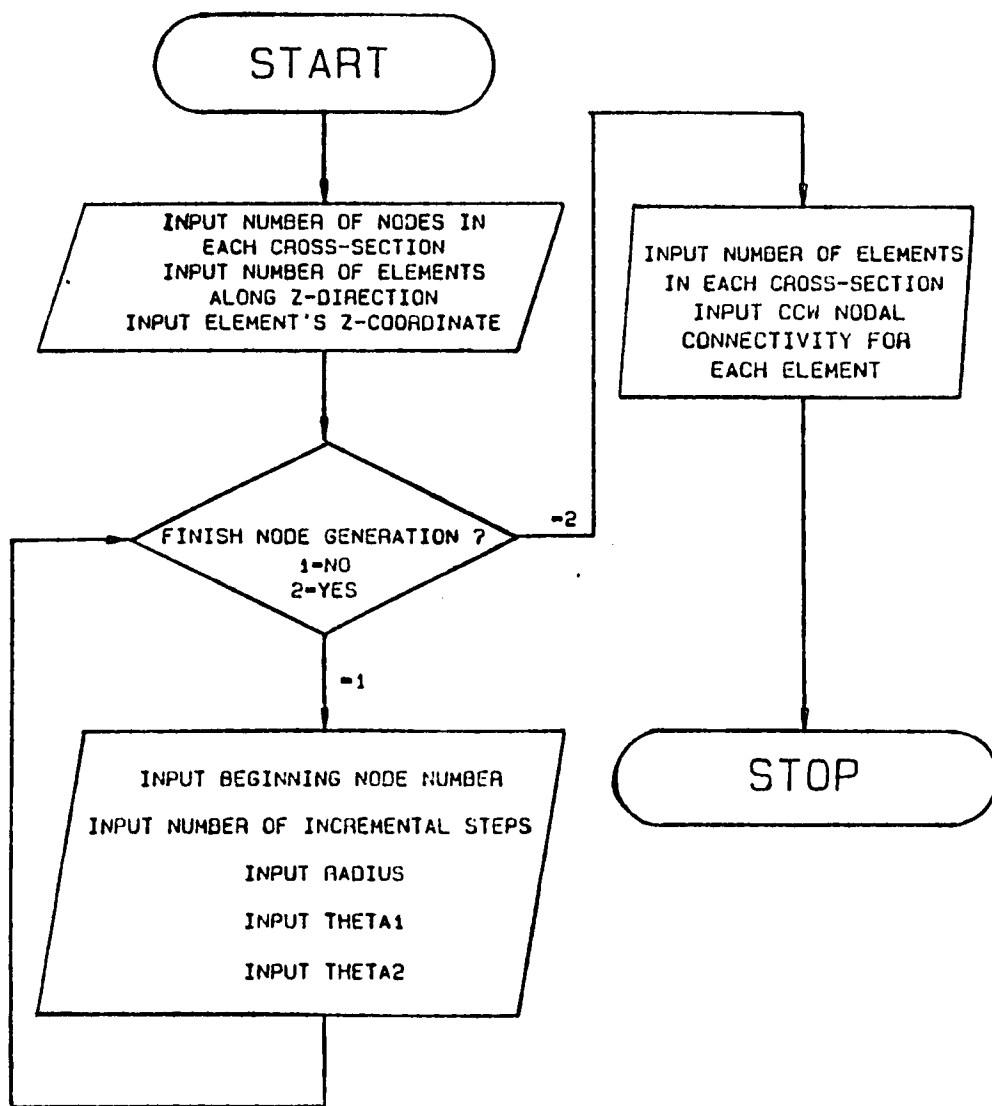


Figure 20: Flowchart of GMESH Program

TIME = 0.00000E+00

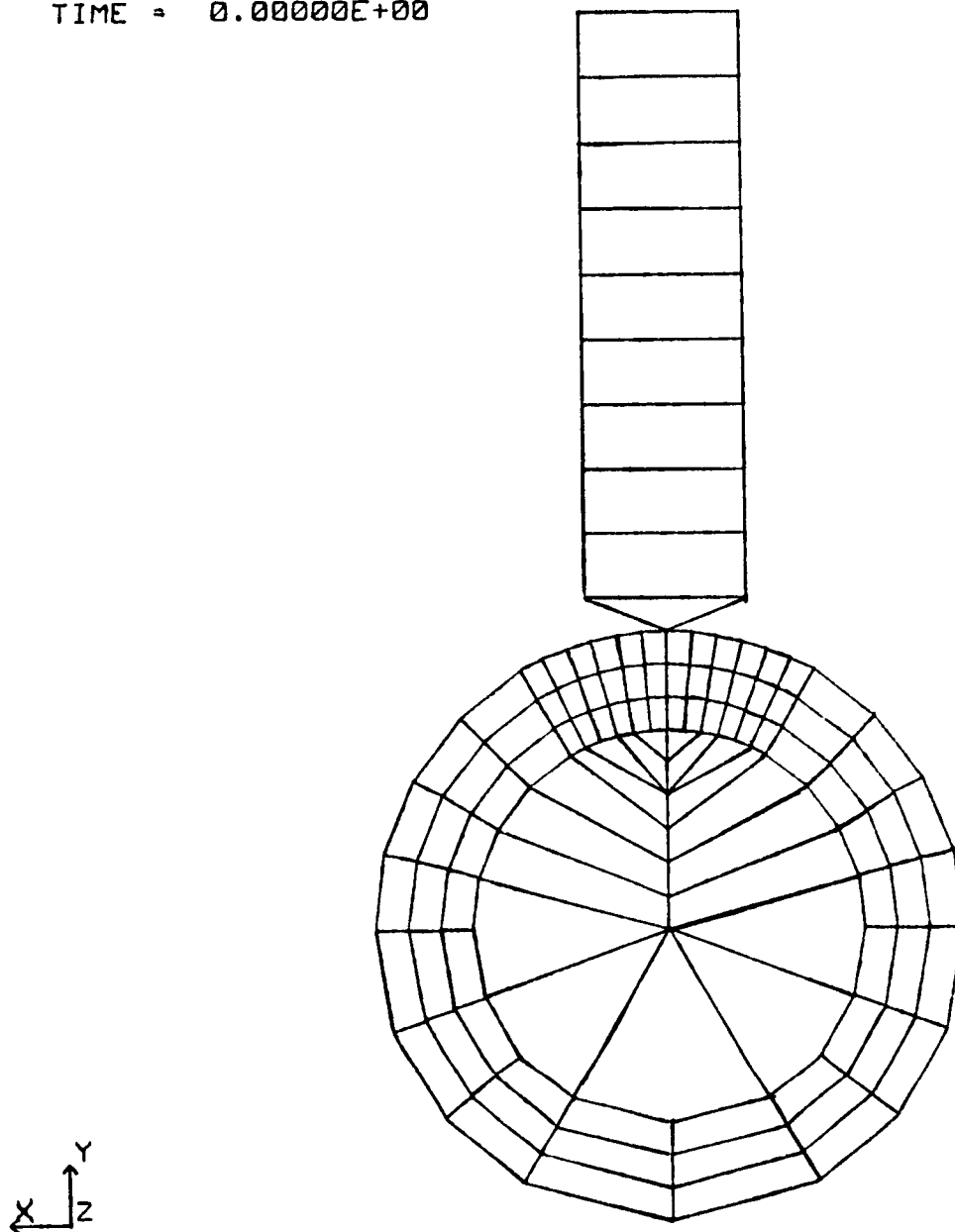


Figure 21: Front View of One-Half Mesh Geometry

TIME = 0.000000E+00

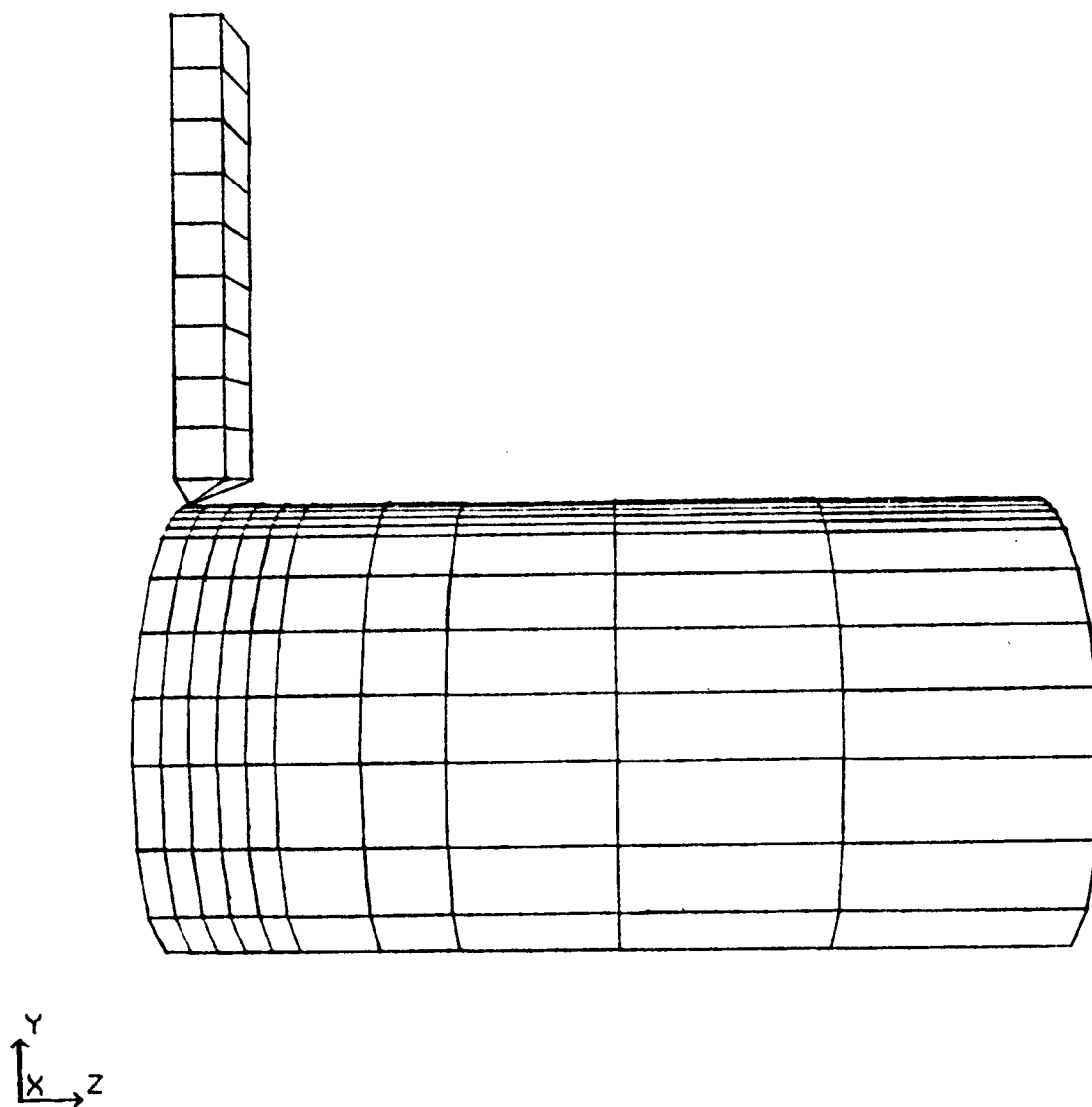


Figure 22: Side View of One-Half Mesh Geometry

TIME = 0.00000E+00

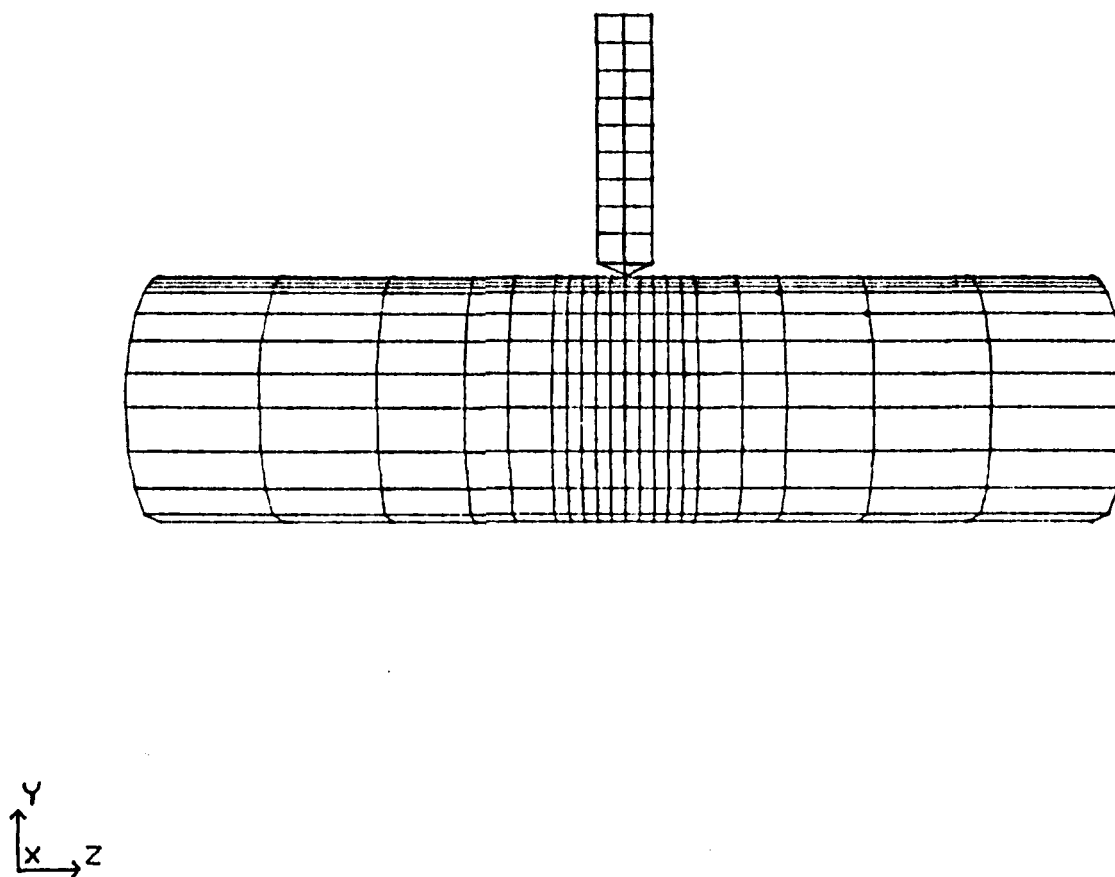


Figure 23: Side View of Entire Mesh Geometry

TIME = 0.00000E+00

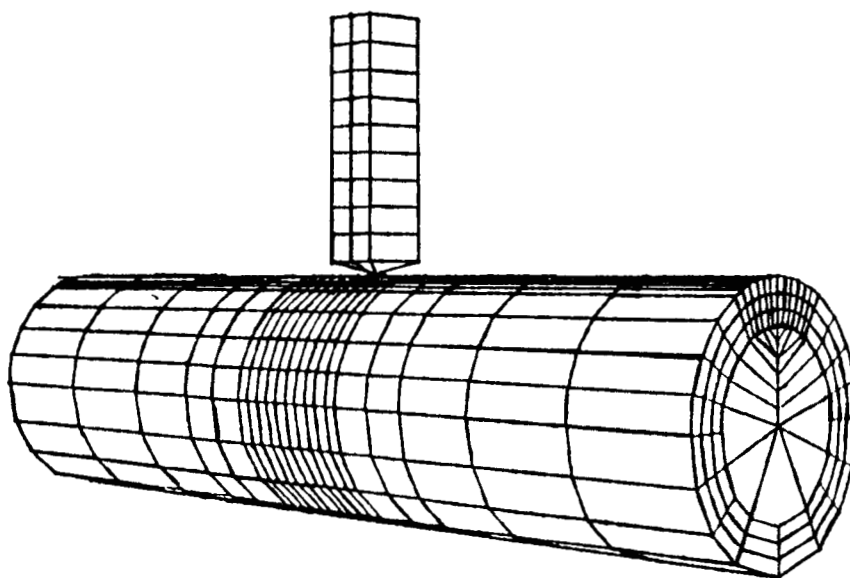


Figure 24: 45° View of Entire Mesh Geometry

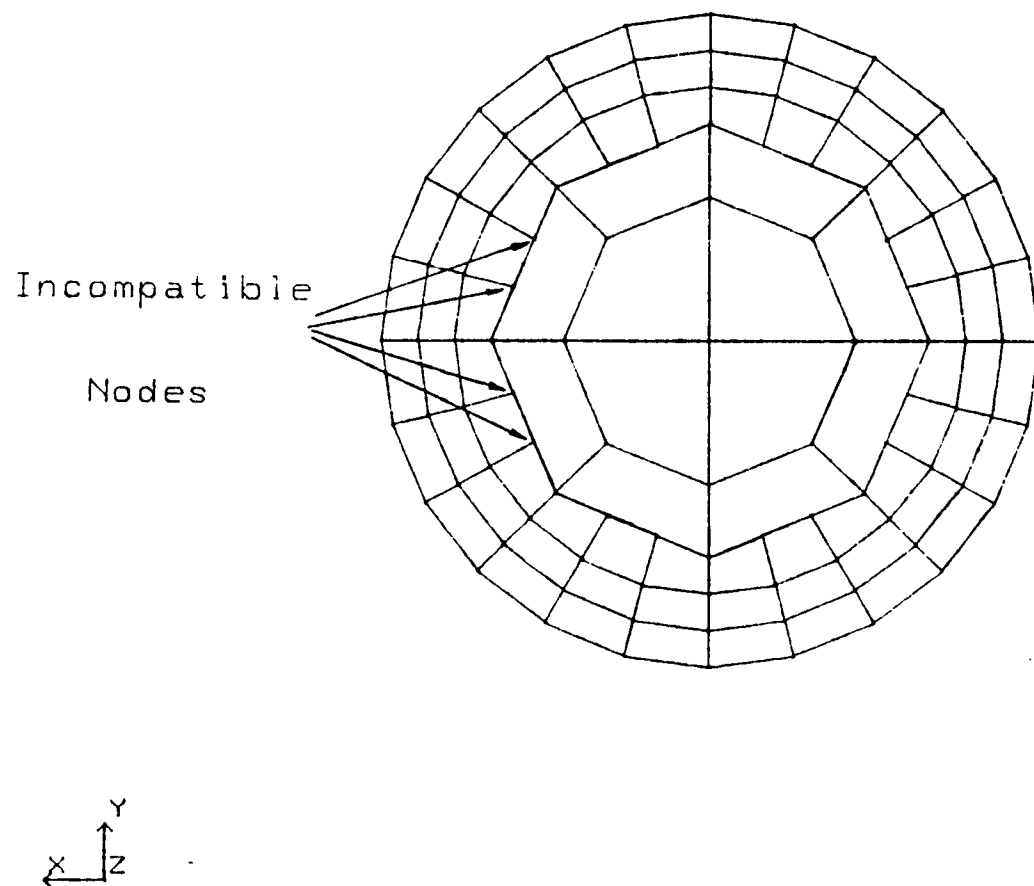


Figure 25: Former Symmetrical Mesh Geometry

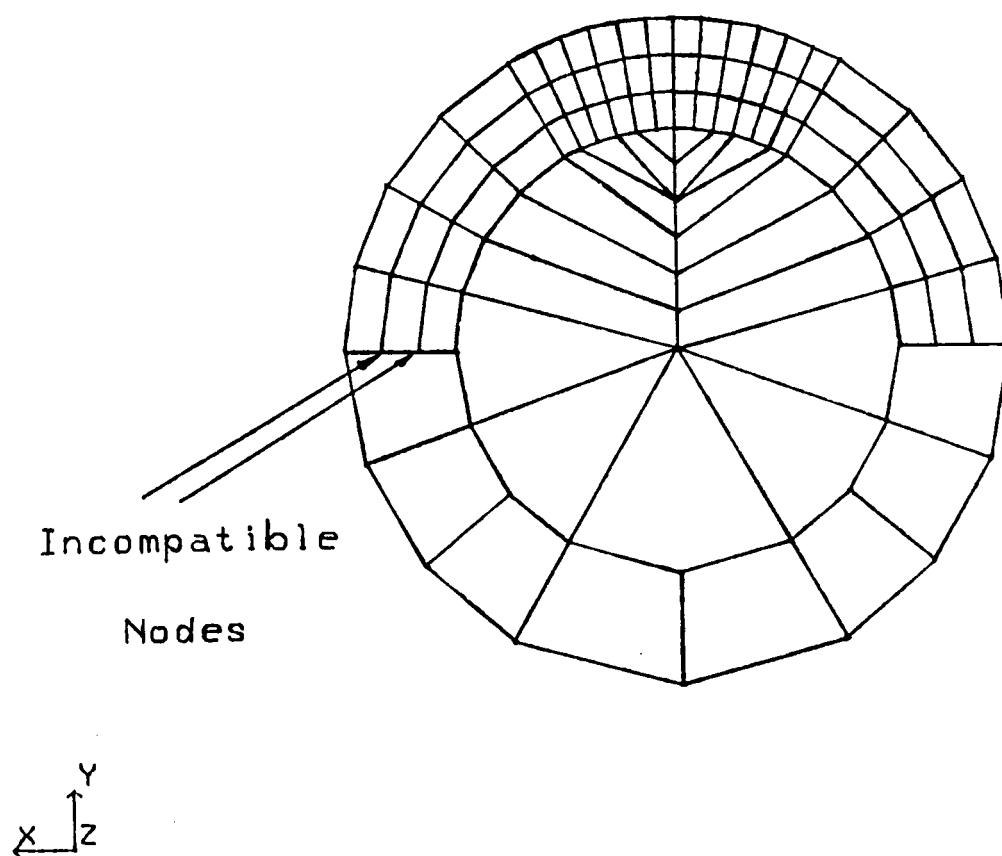


Figure 26: Former Mesh Geometry

TIME = 0.12002E-04

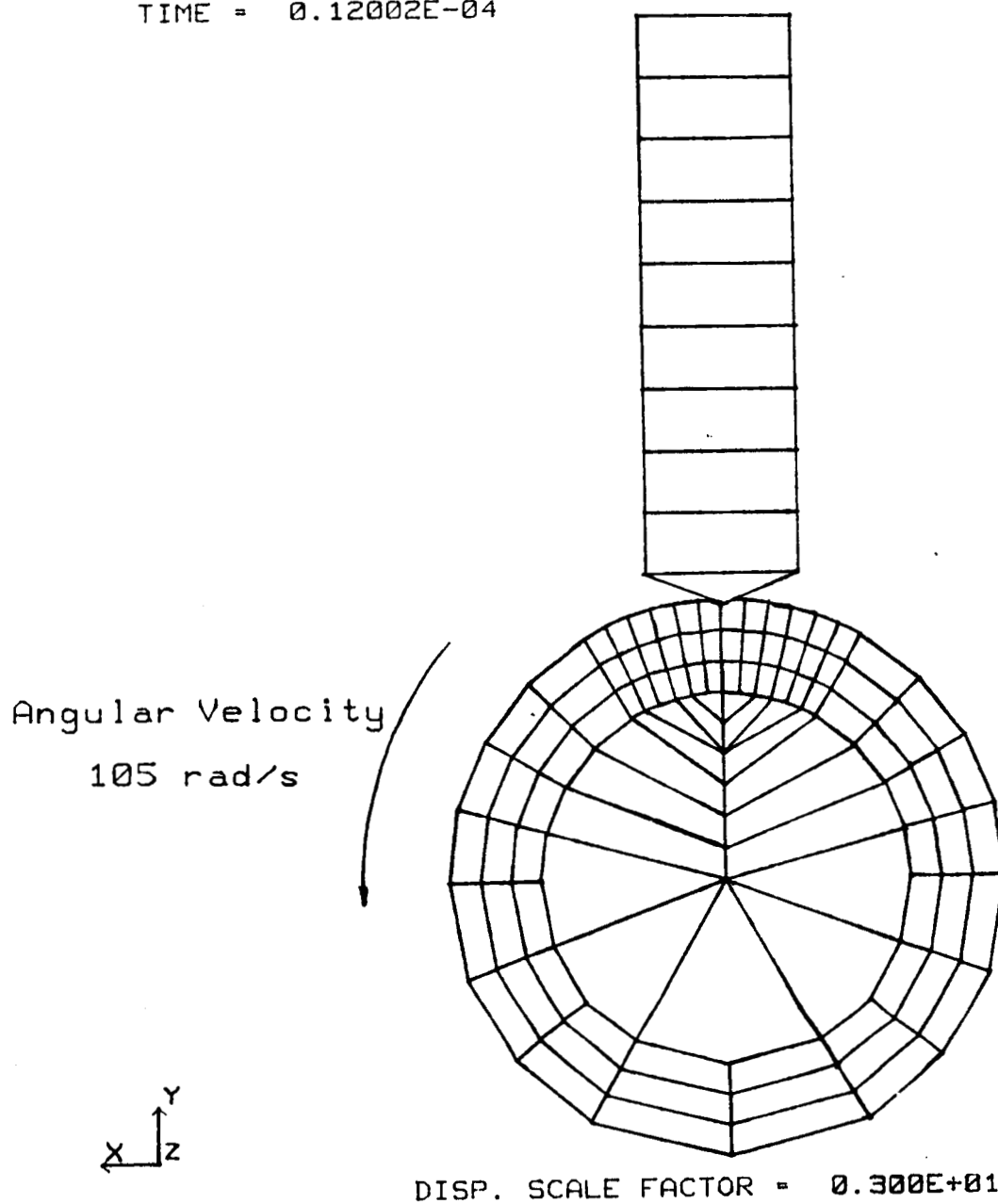
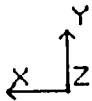


Figure 27: Mesh Geometry at 12 Micro-Seconds After Initial Impact of Diamond on Rotating Shaft

TIME = 0.27000E-04

Angular Velocity
105 rad/s



DISP. SCALE FACTOR = 0.300E+01

Figure 28: Mesh Geometry at 27 Micro-Seconds After Initial Impact of Diamond on Rotating Shaft

TIME = 0.11700E-03

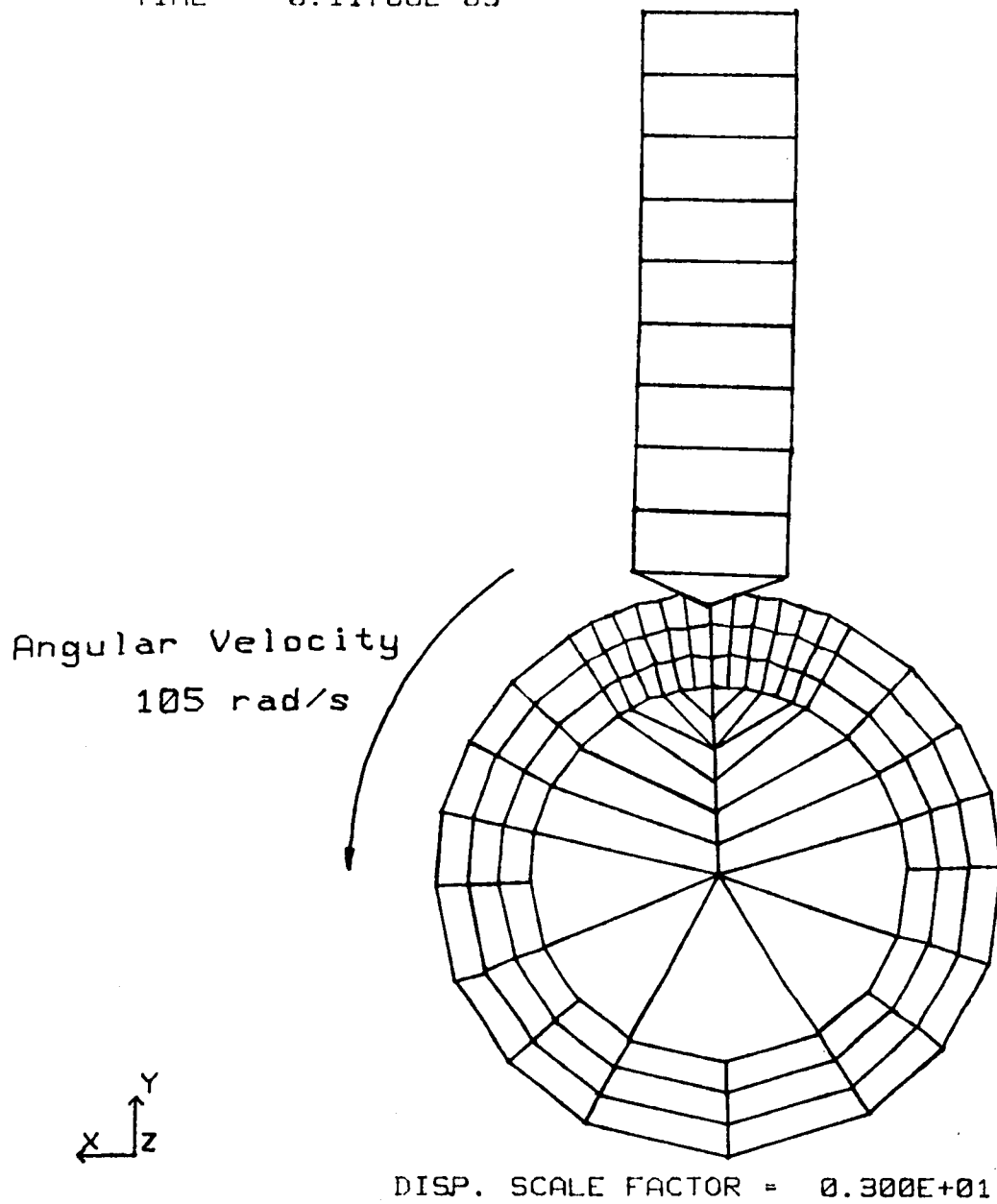


Figure 29: Mesh Geometry at 117 Micro-Seconds

TIME = 0.13200E-03

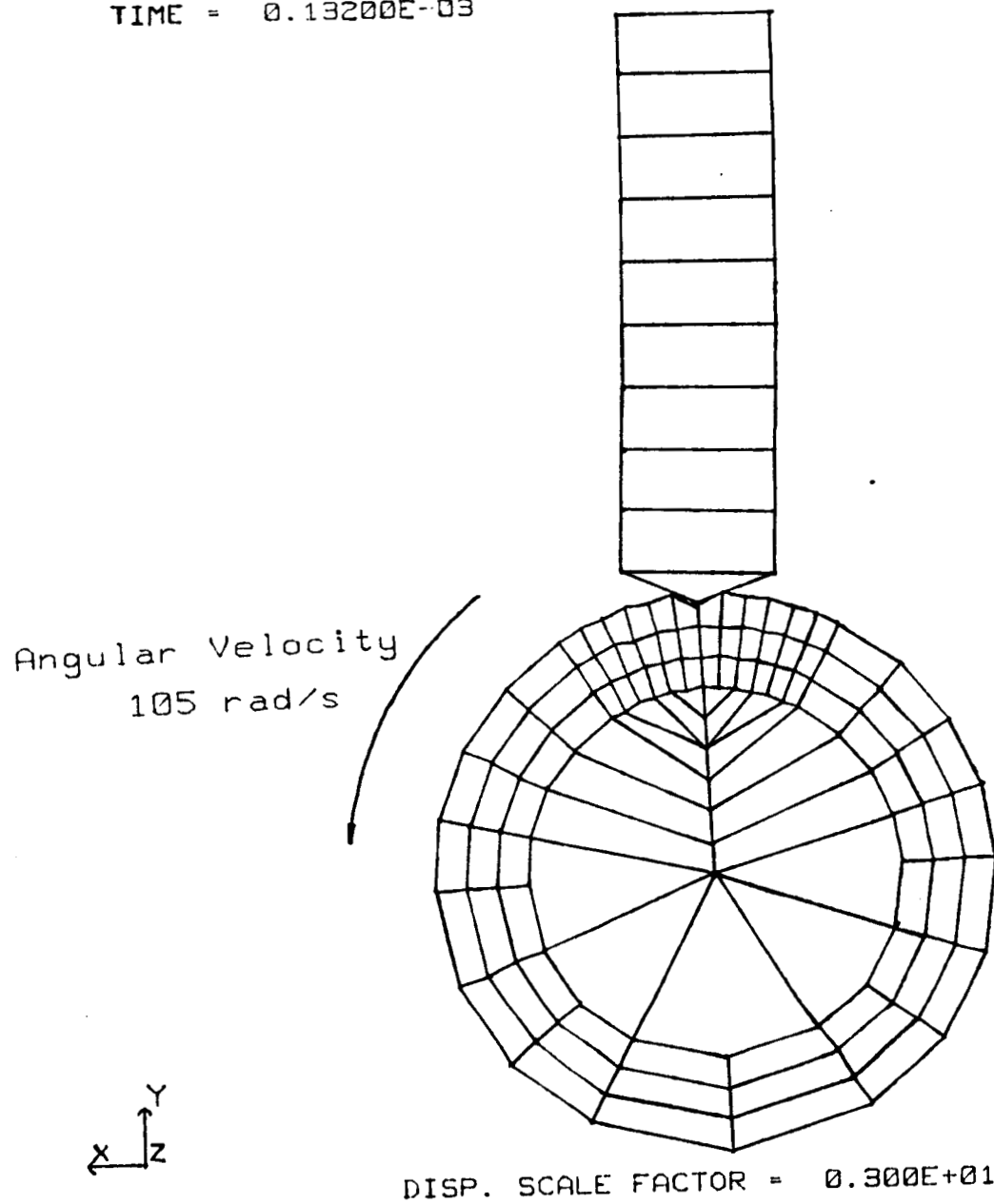


Figure 30: Mesh Geometry at 132 Micro-Seconds at Which Rebounding Begins

TIME = 0.14700E-03

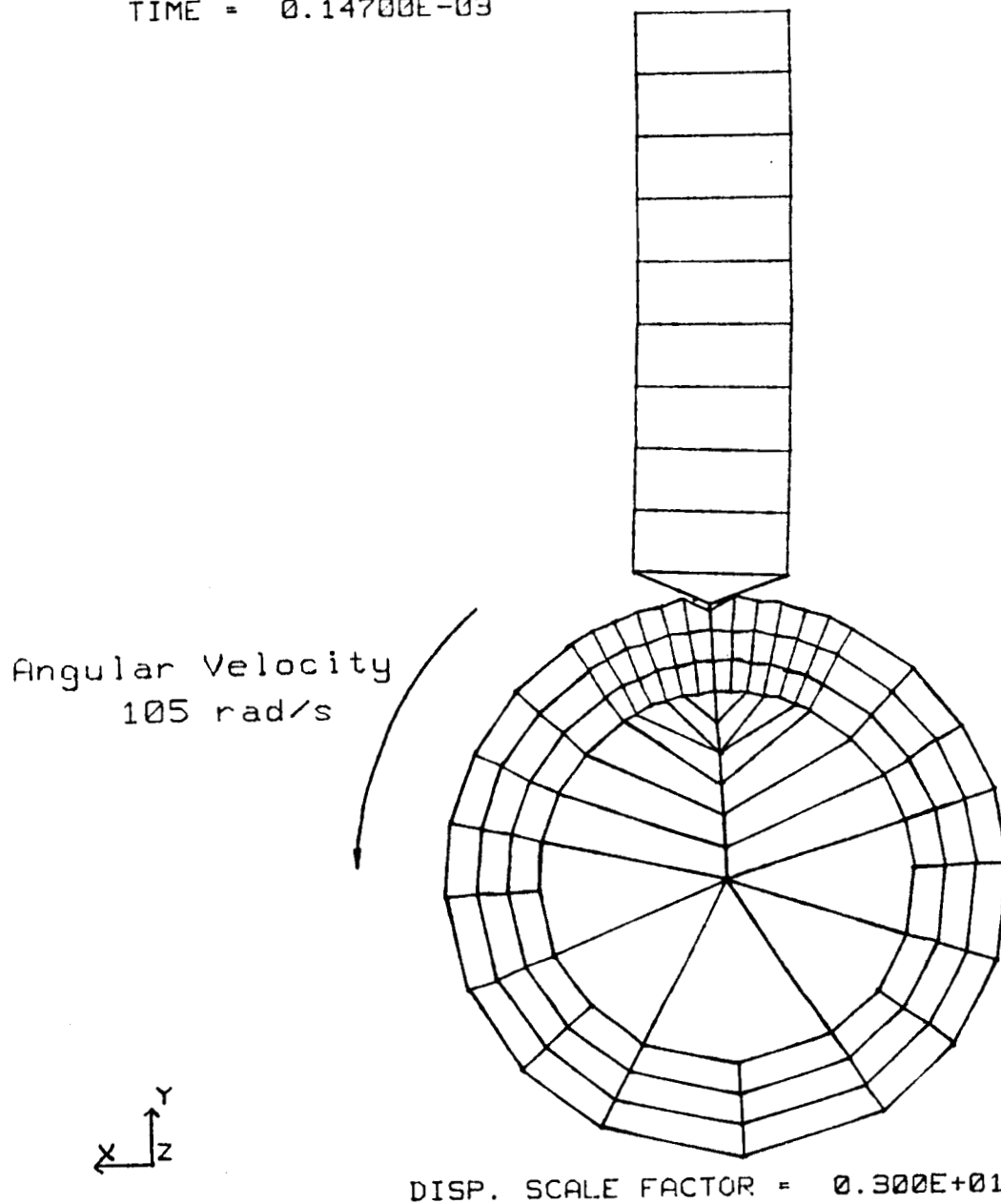


Figure 31: Mesh Geometry at 147 Micro-Seconds at Which Rebounding Continues

TIME = 0.19800E-03

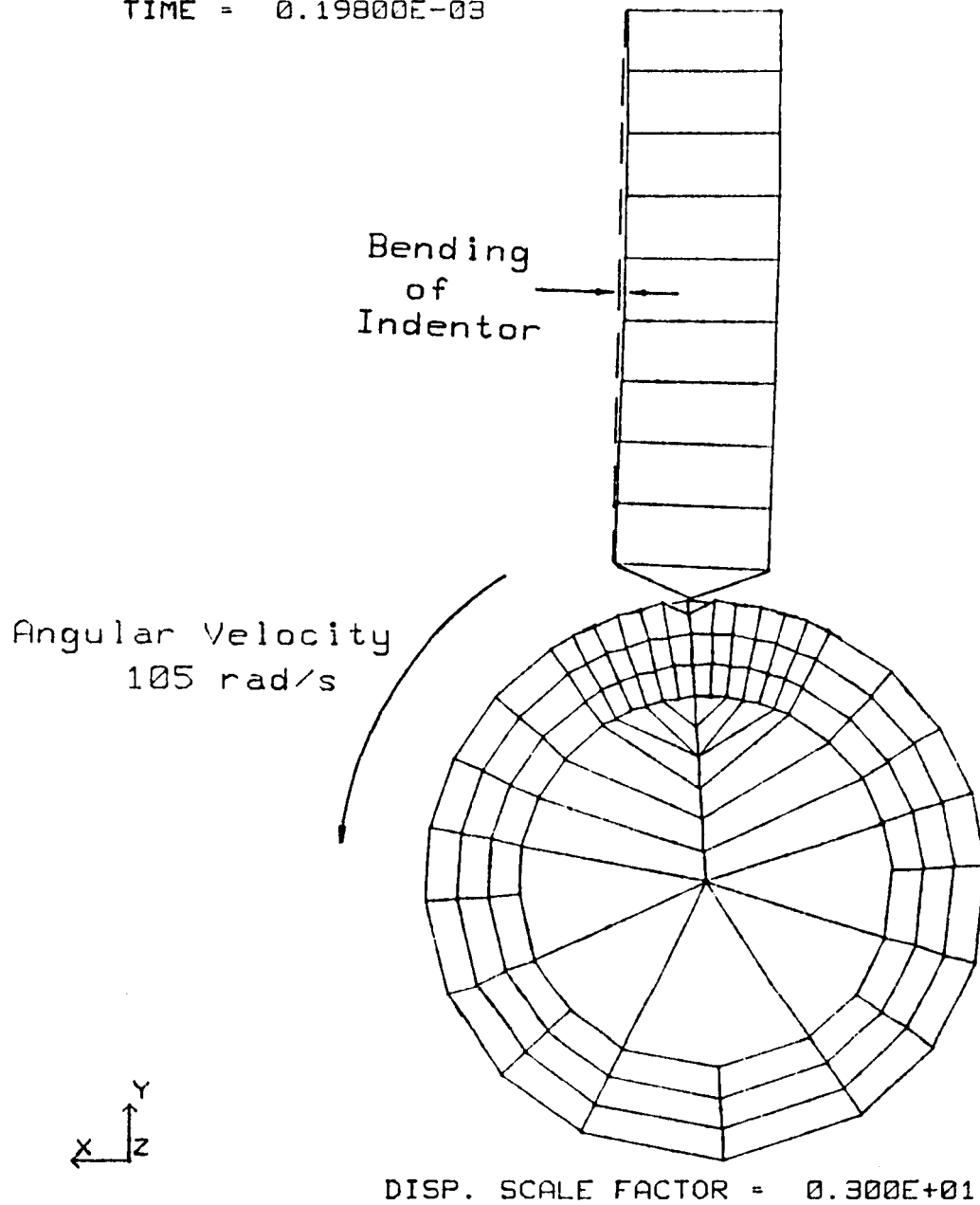


Figure 32: Mesh Geometry at 198 Micro-Seconds Showing Indented Crater and Bending Of indenter

TIME = 0.19800E-03

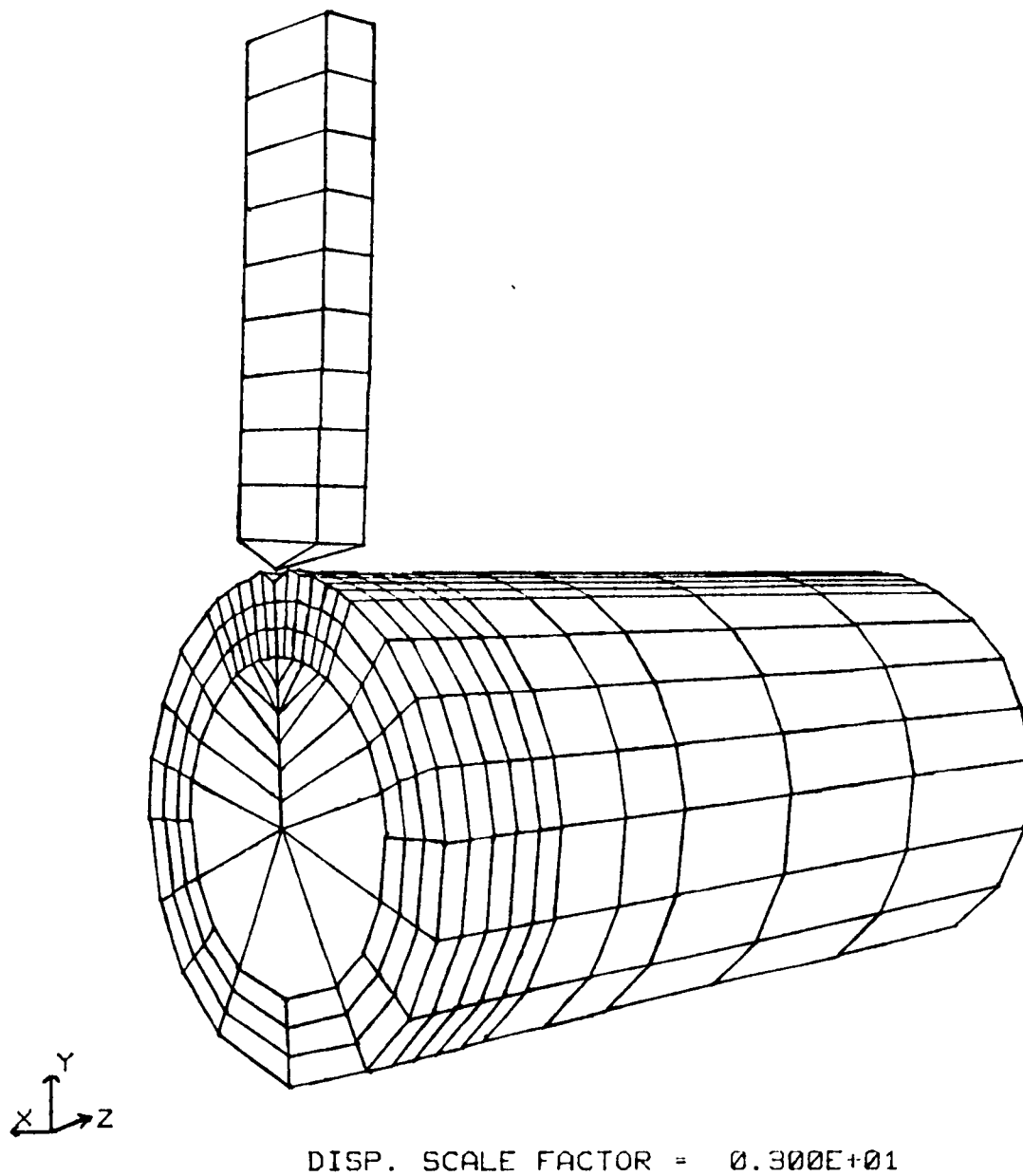
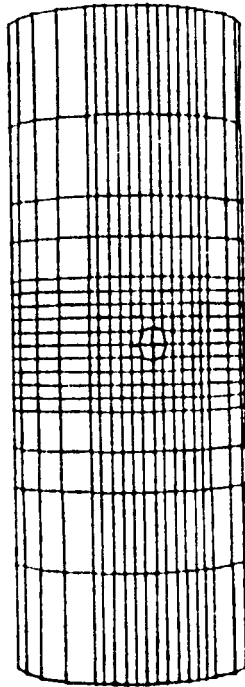


Figure 33: 50° View of Mesh Geometry at 198 Micro-Seconds

ORIGINAL PAGE IS
OF POOR QUALITY

TIME = 0.19800E-03



DISP. SCALE FACTOR = 0.100E+02

Figure 34: Top View of Entire Mesh Geometry With Indented
Crater at 198 Micro-Seconds

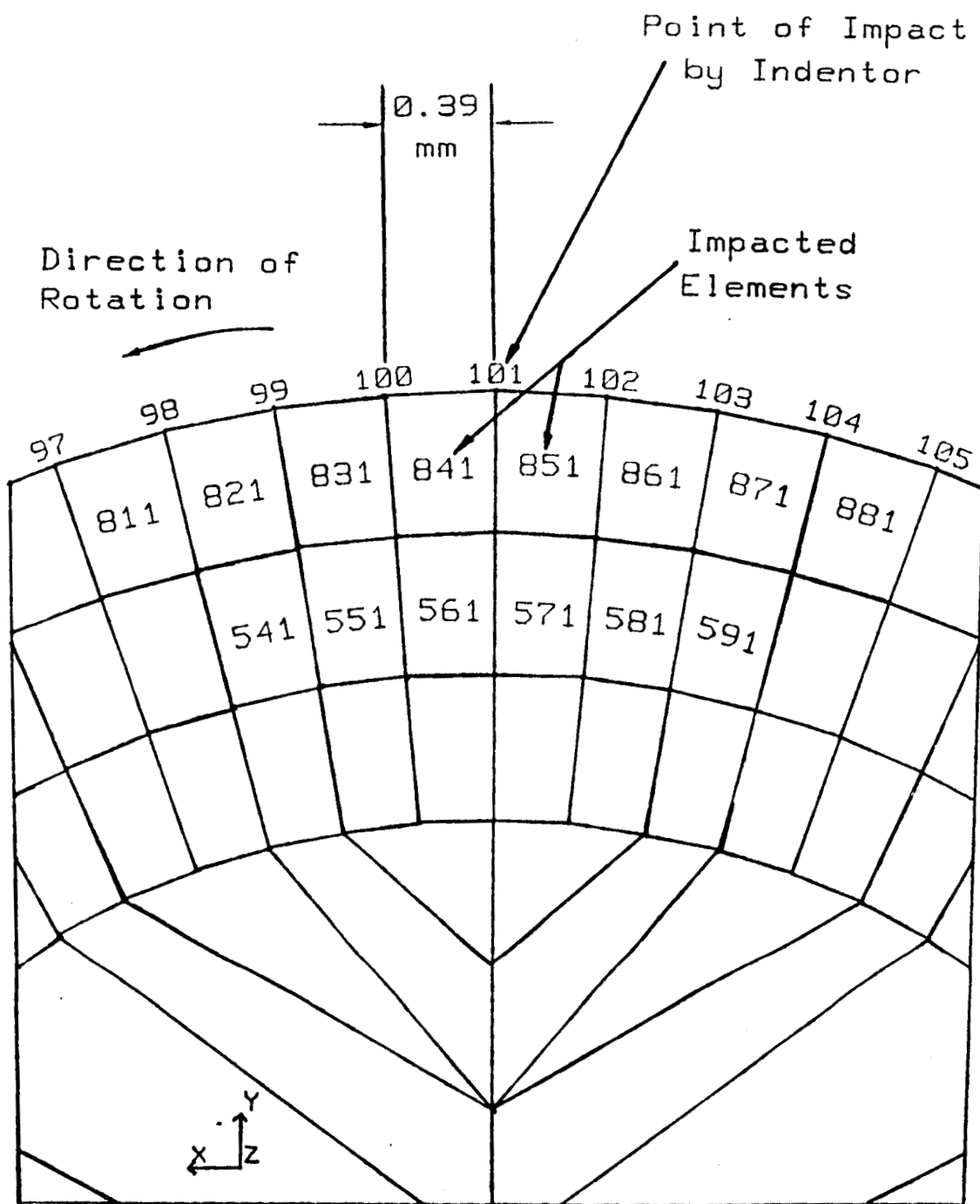


Figure 35: Close-up View of the Impact Region of Interest With Numbered Nodes and Elements

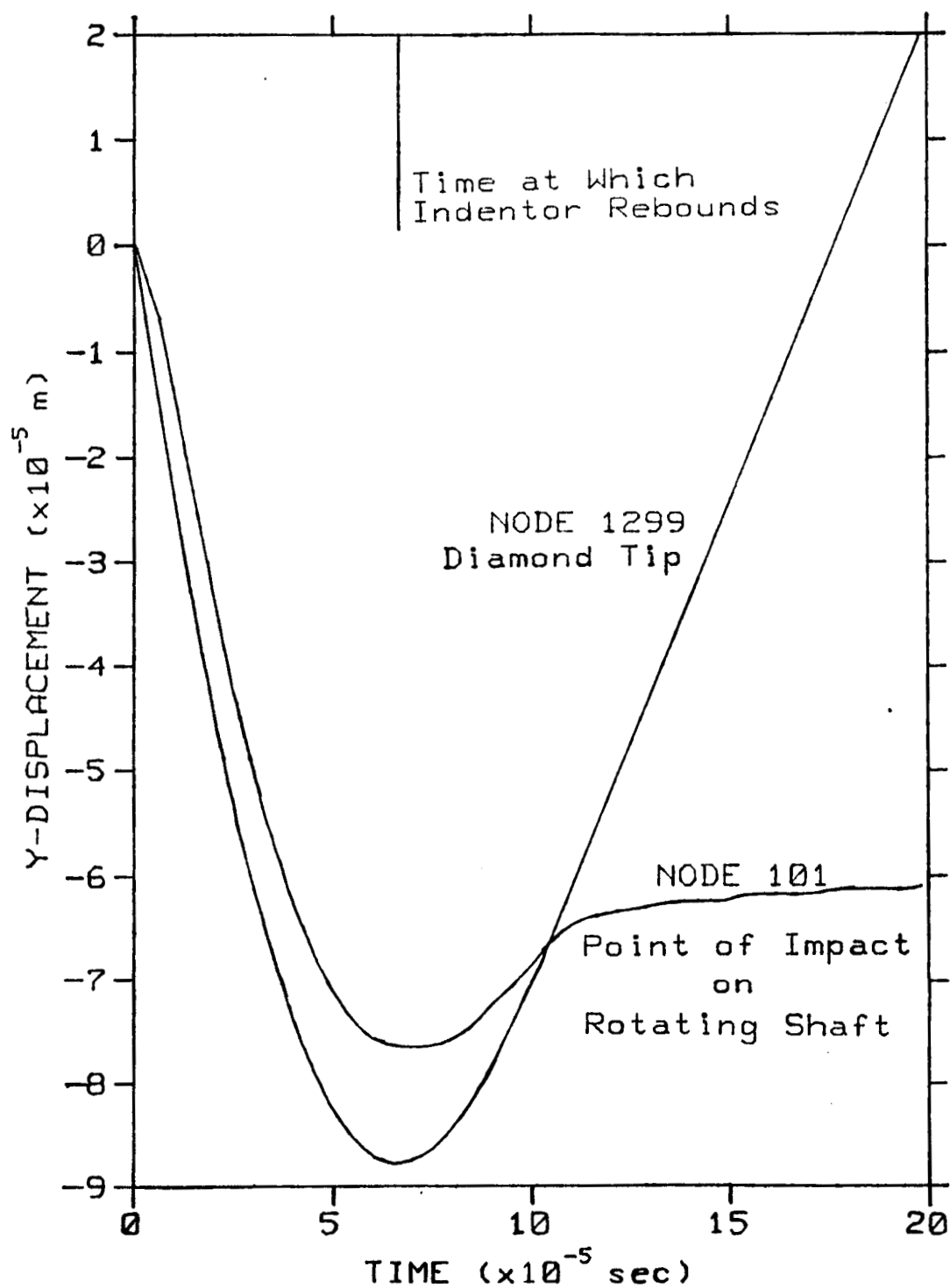


Figure 36: Y-Displacement Vs. Time at Nodes 1299 and 101

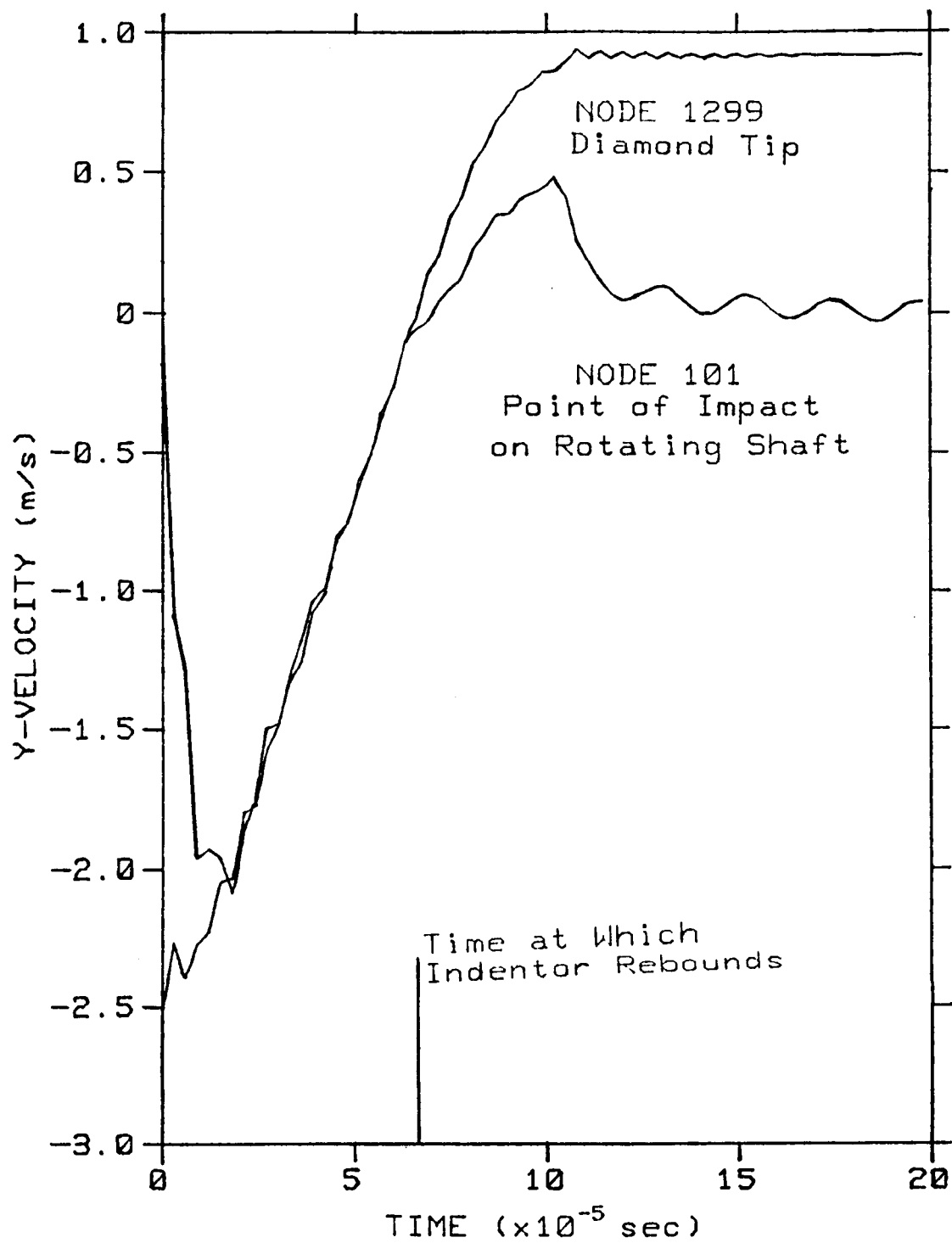


Figure 37: Y-Velocity vs. Time at Nodes 1299 and 101

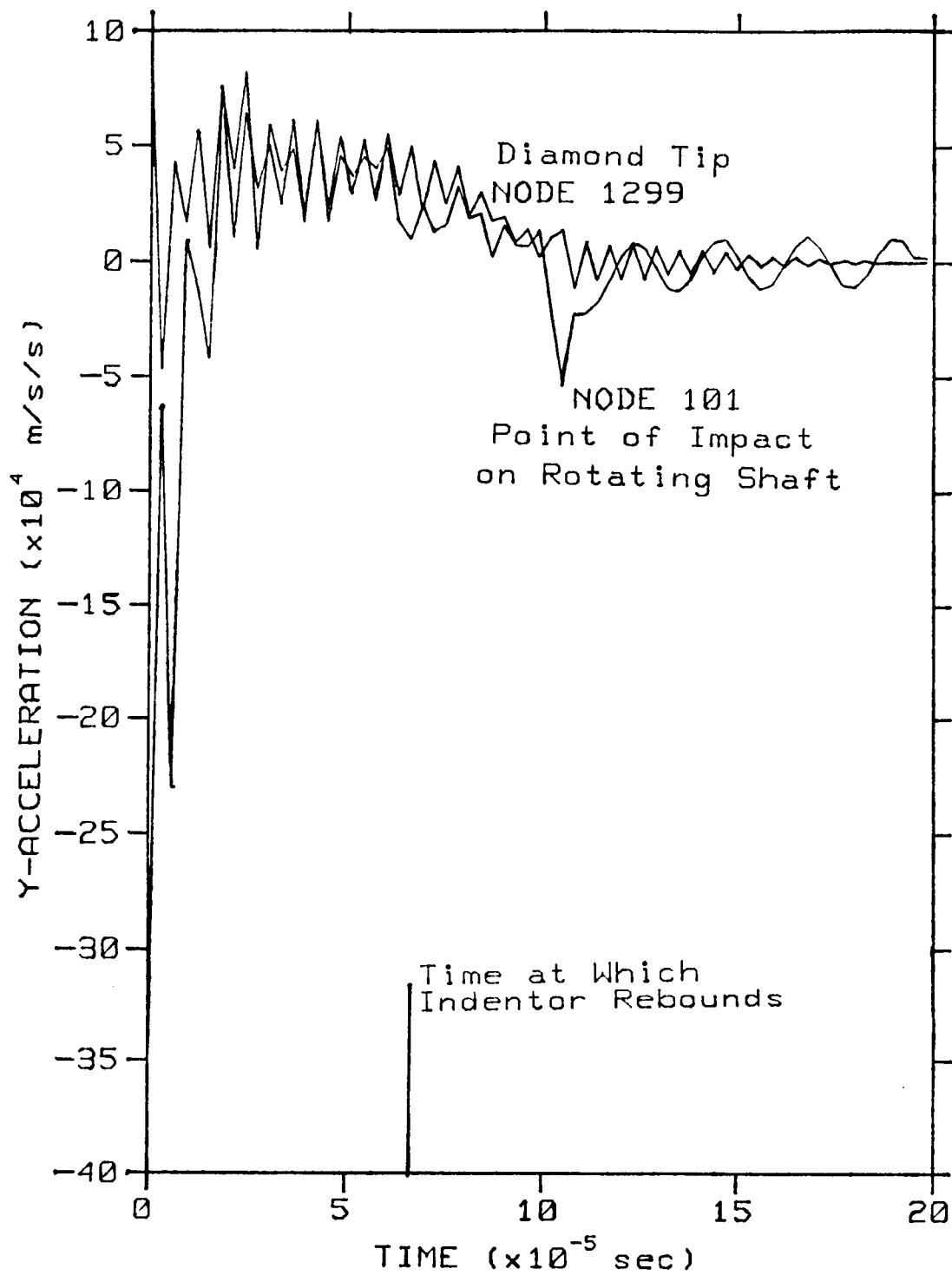


Figure 38: Y-Acceleration vs. Time at Nodes 1299 and 101

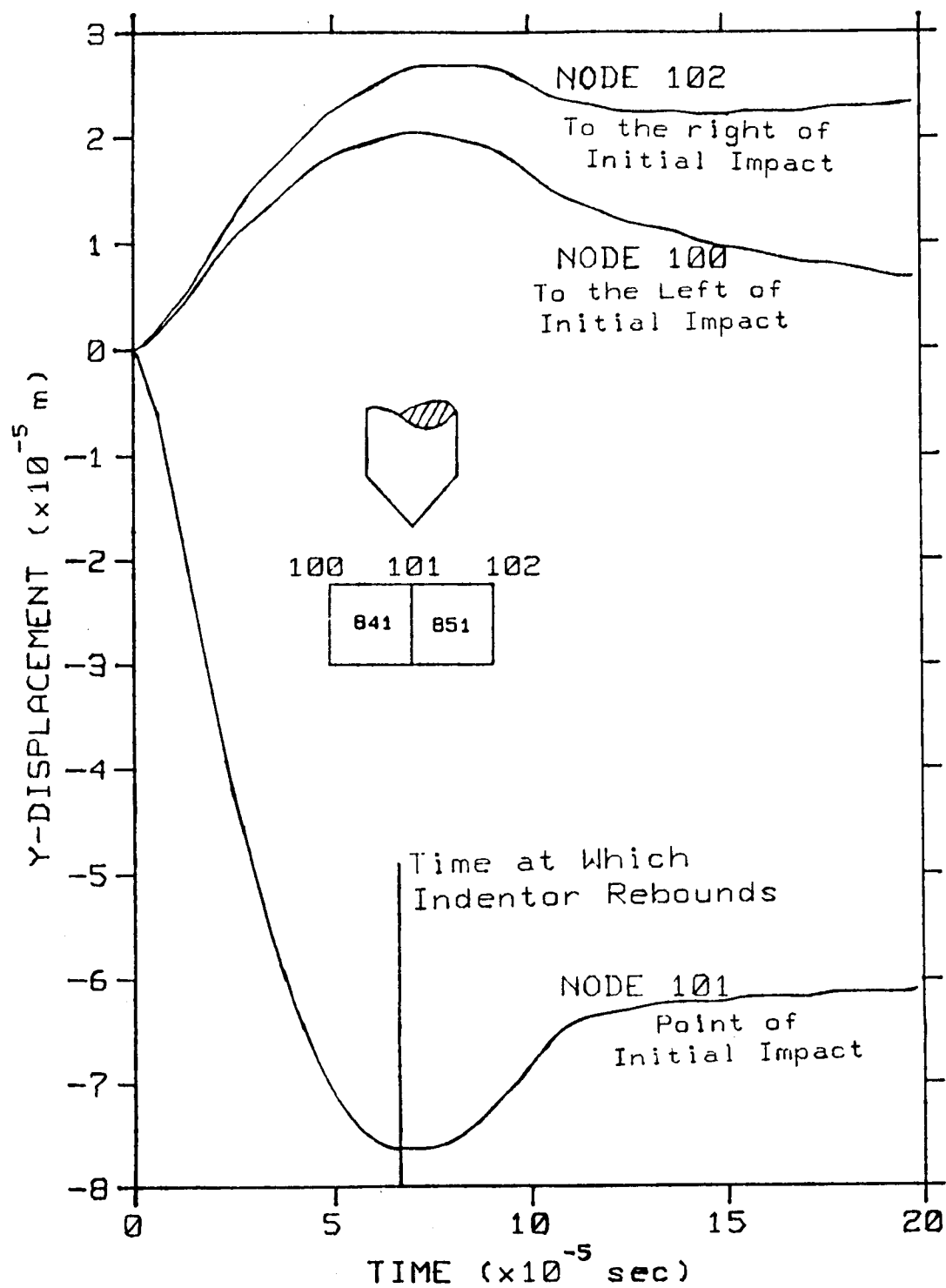


Figure 39: Y-Displacement vs. Time at Nodes 100, 101, and 102

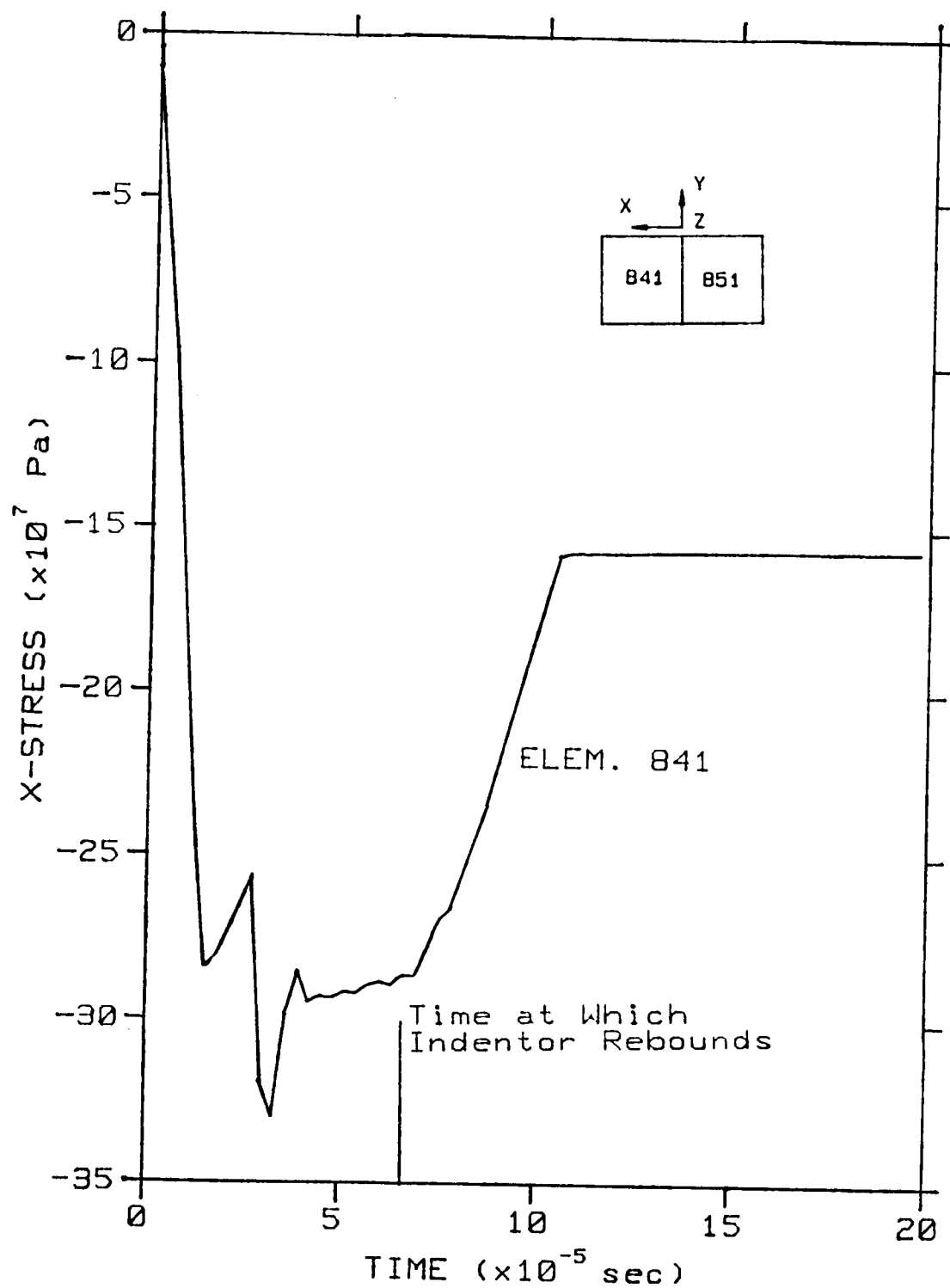


Figure 40: X-Stress vs. Time for Element 841

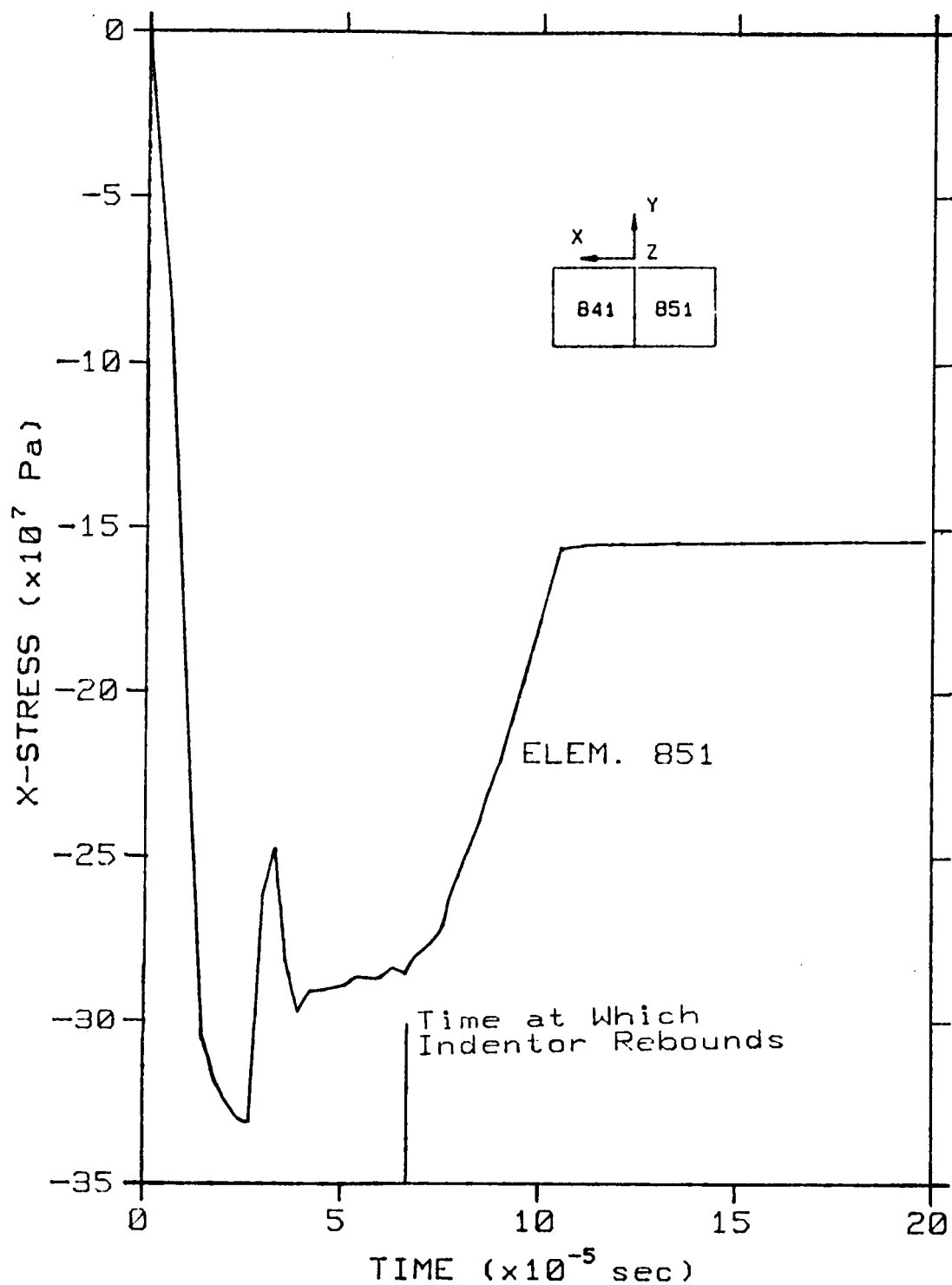


Figure 41: X-Stress vs. Time for Element 851

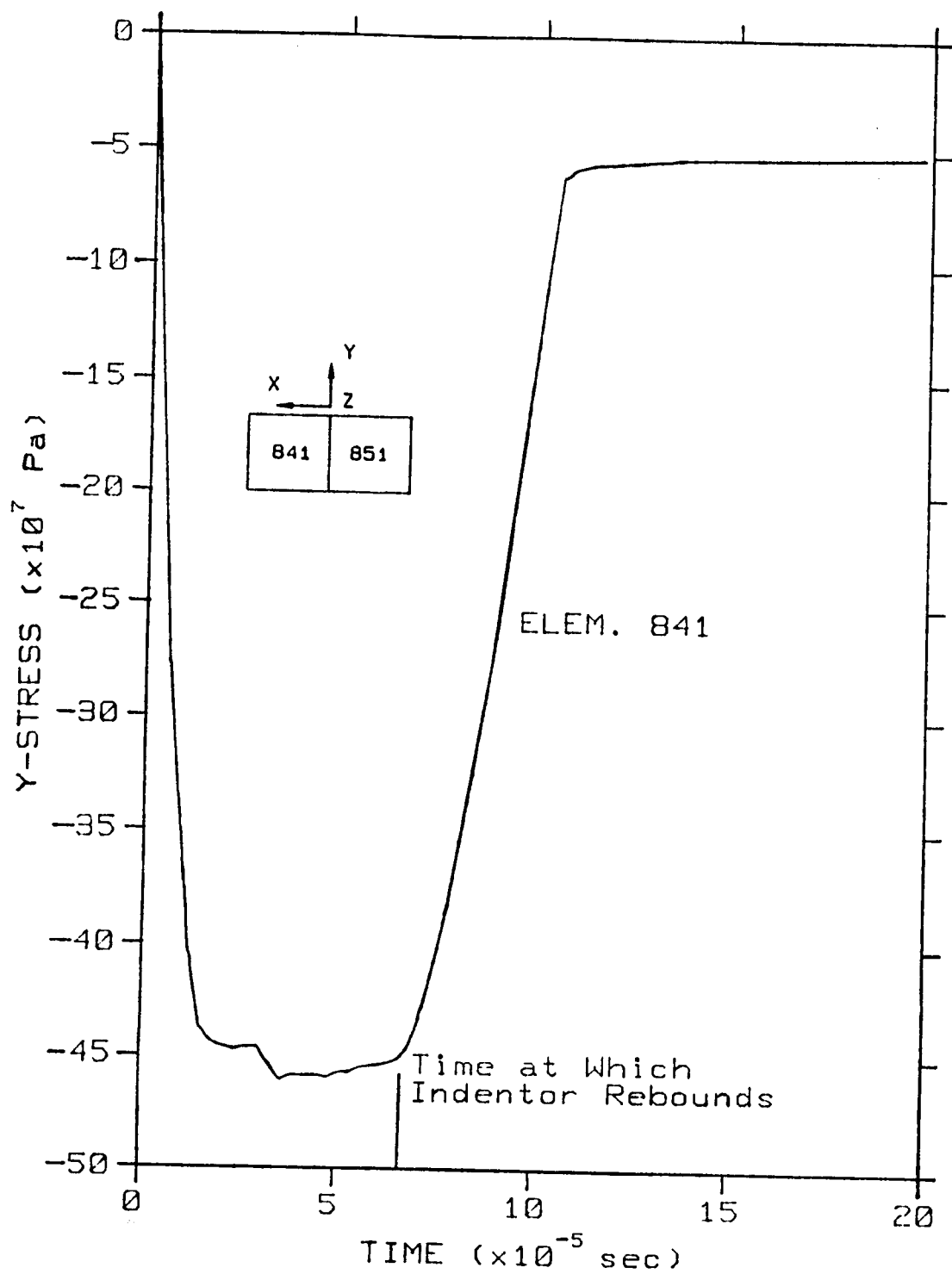


Figure 42: Y-Stress vs. Time for Element 841

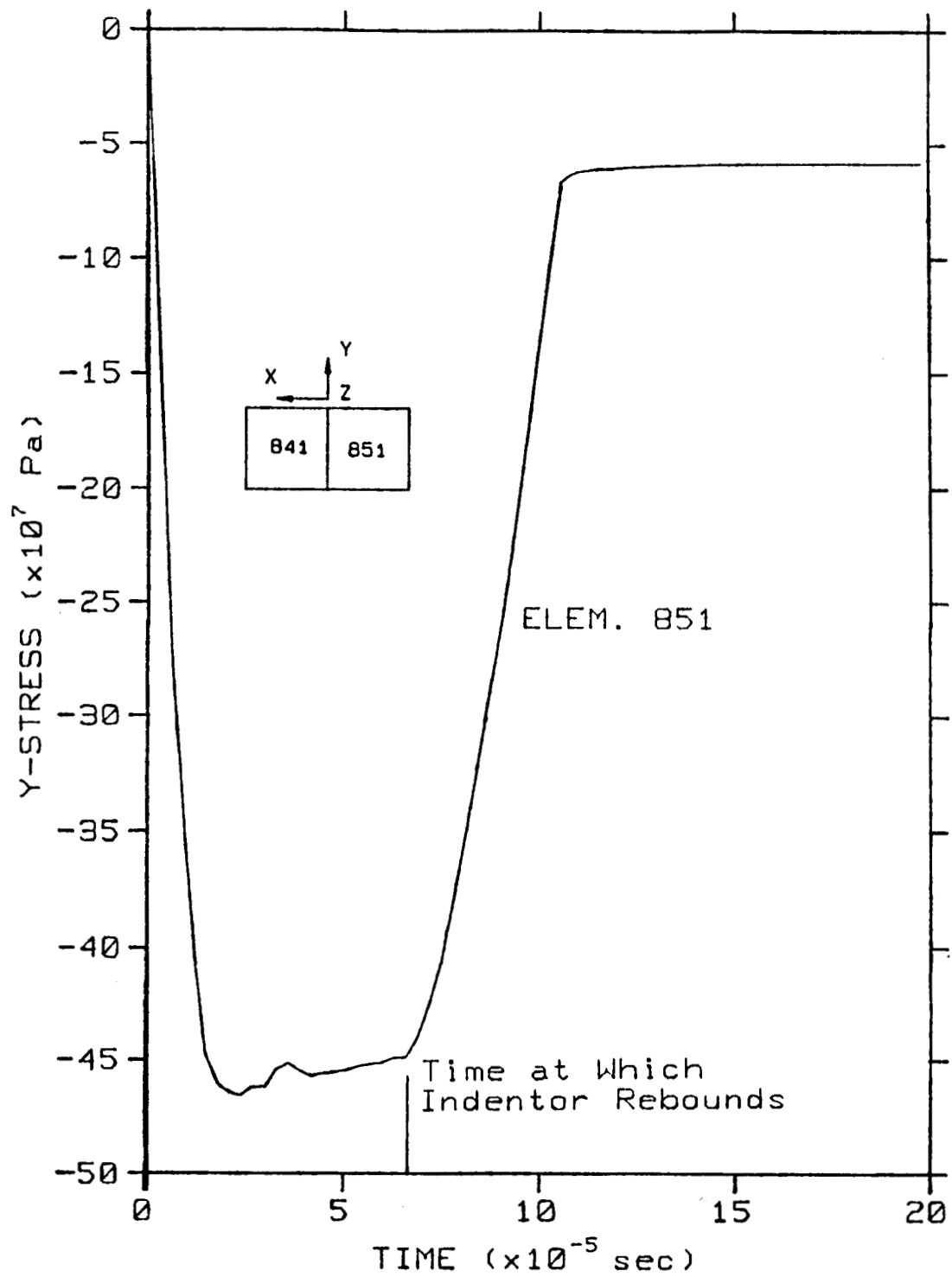


Figure 43: Y-Stress vs. Time for Element 851

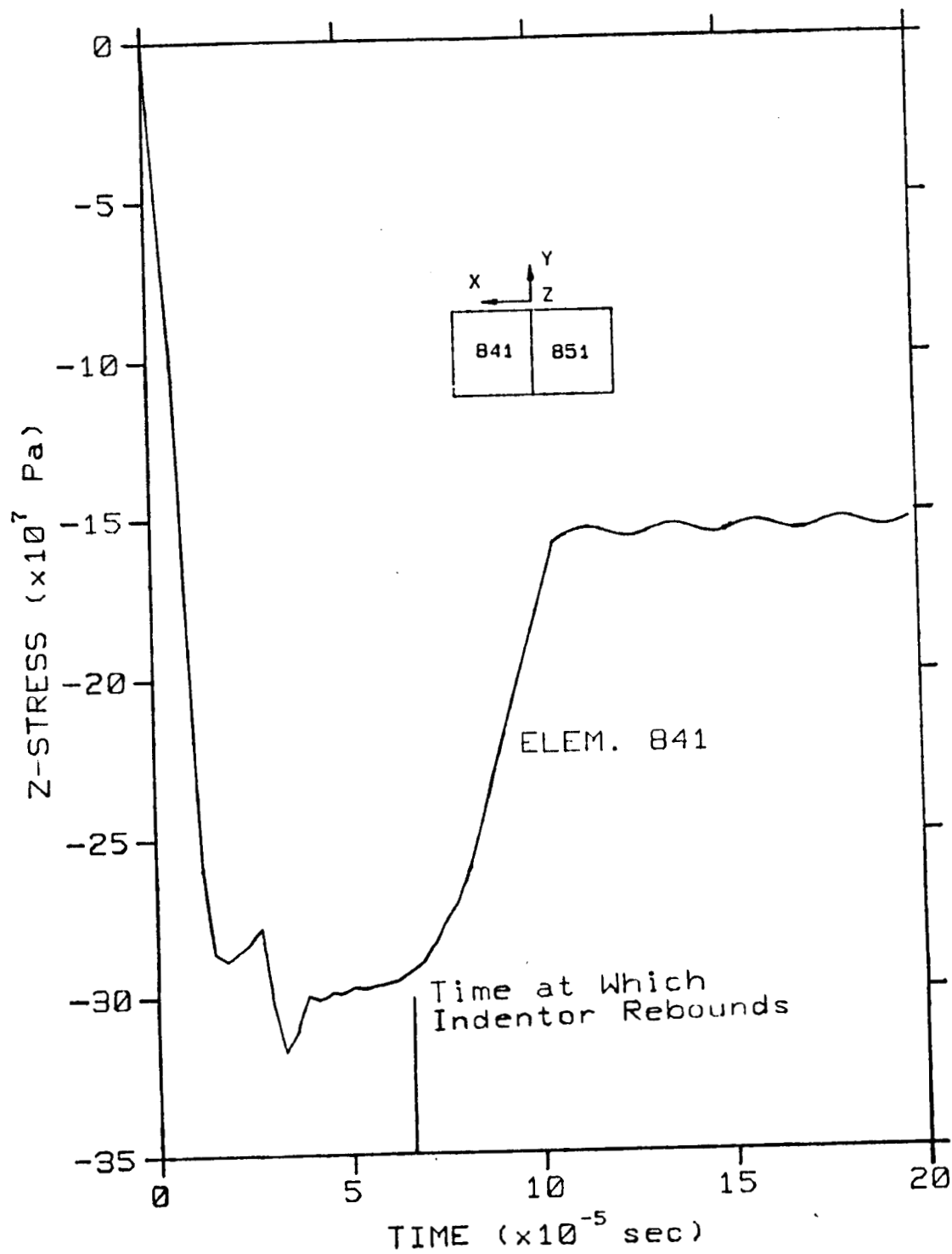


Figure 44: Z-Stress vs. Time for Element 841

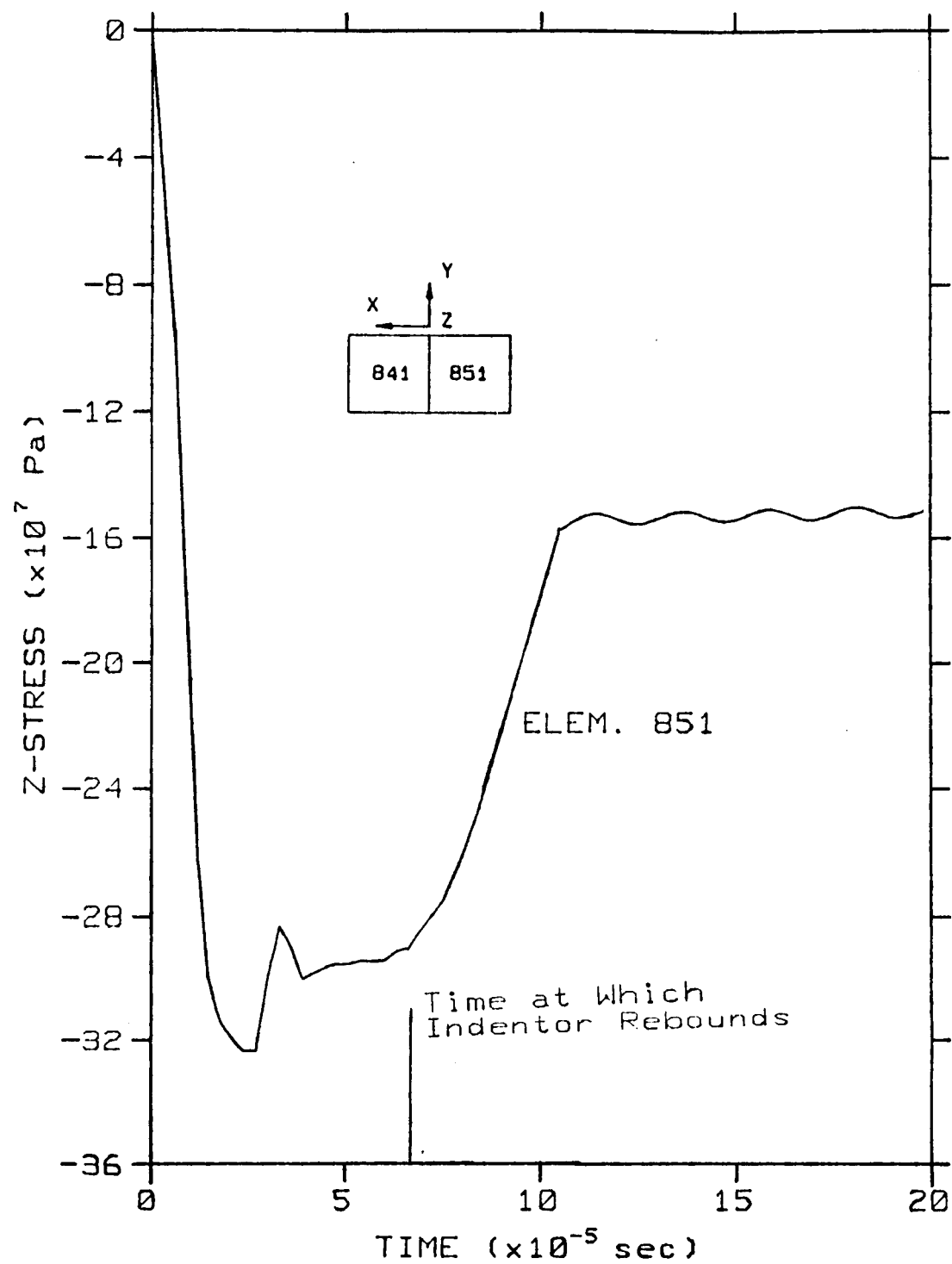


Figure 45: Z-Stress vs. Time for Element 851

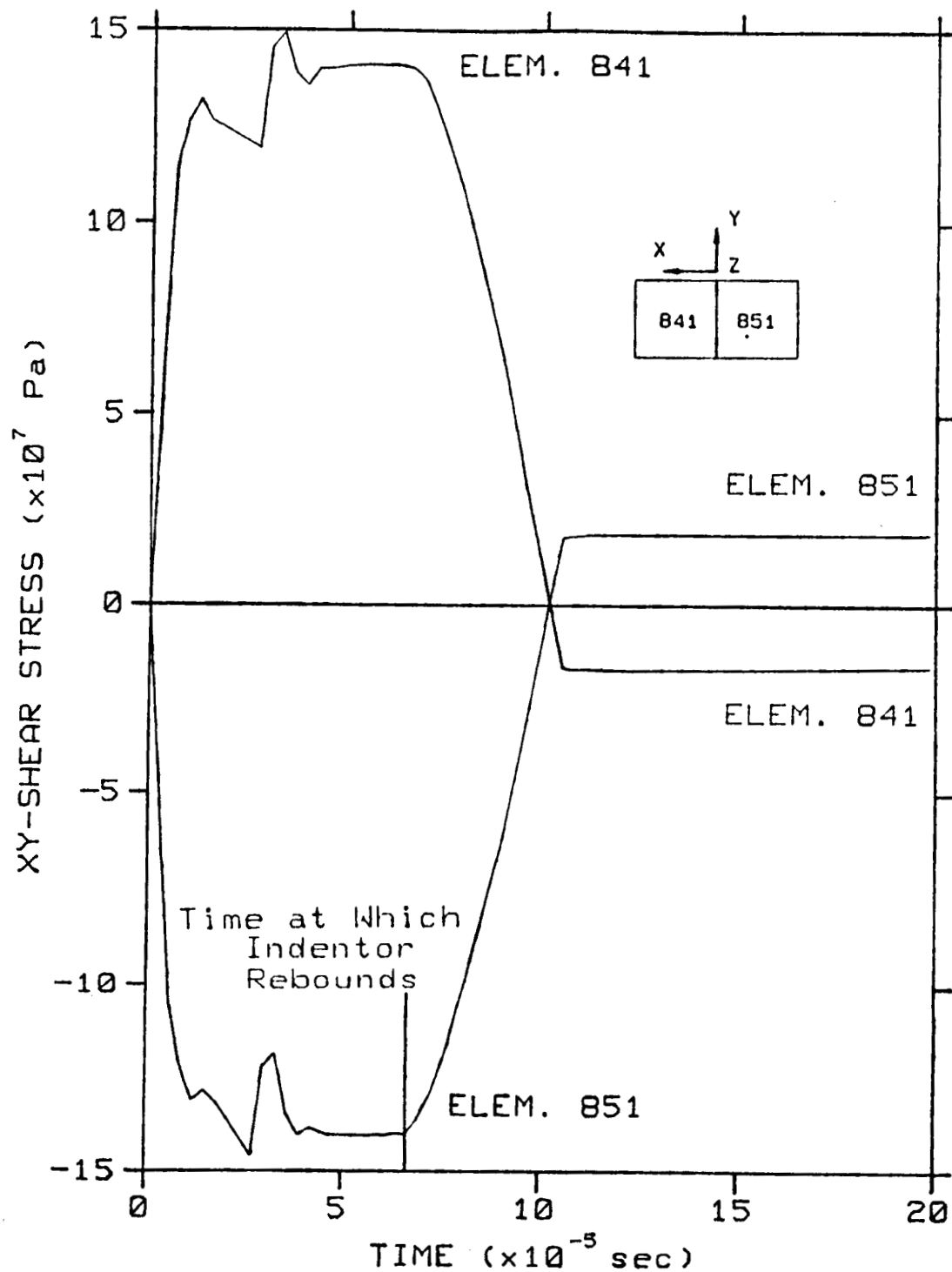


Figure 46: XY-Shear Stress vs. Time for Elements 841 and 851

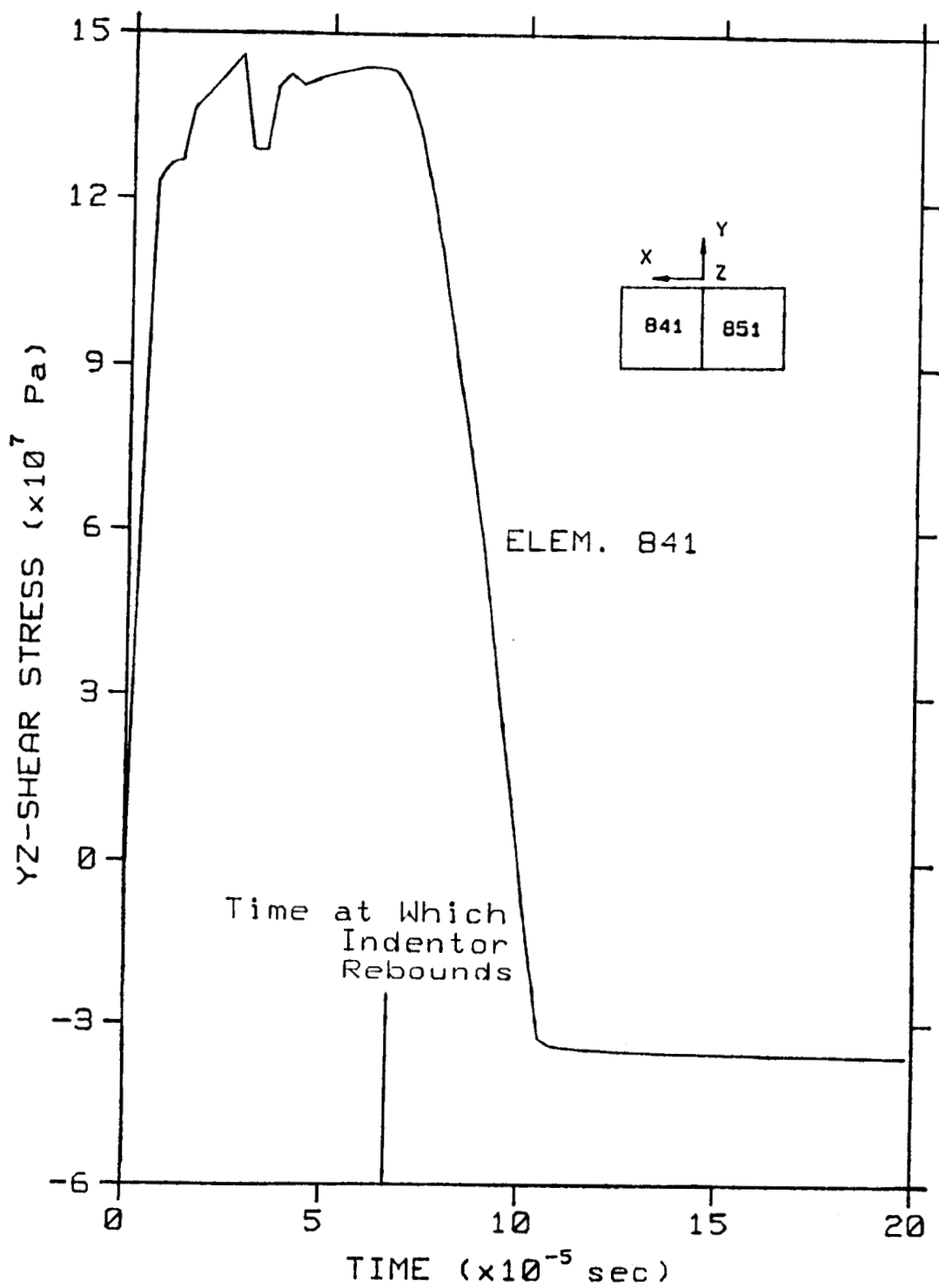


Figure 47: YZ-Shear Stress vs. Time for Element 841

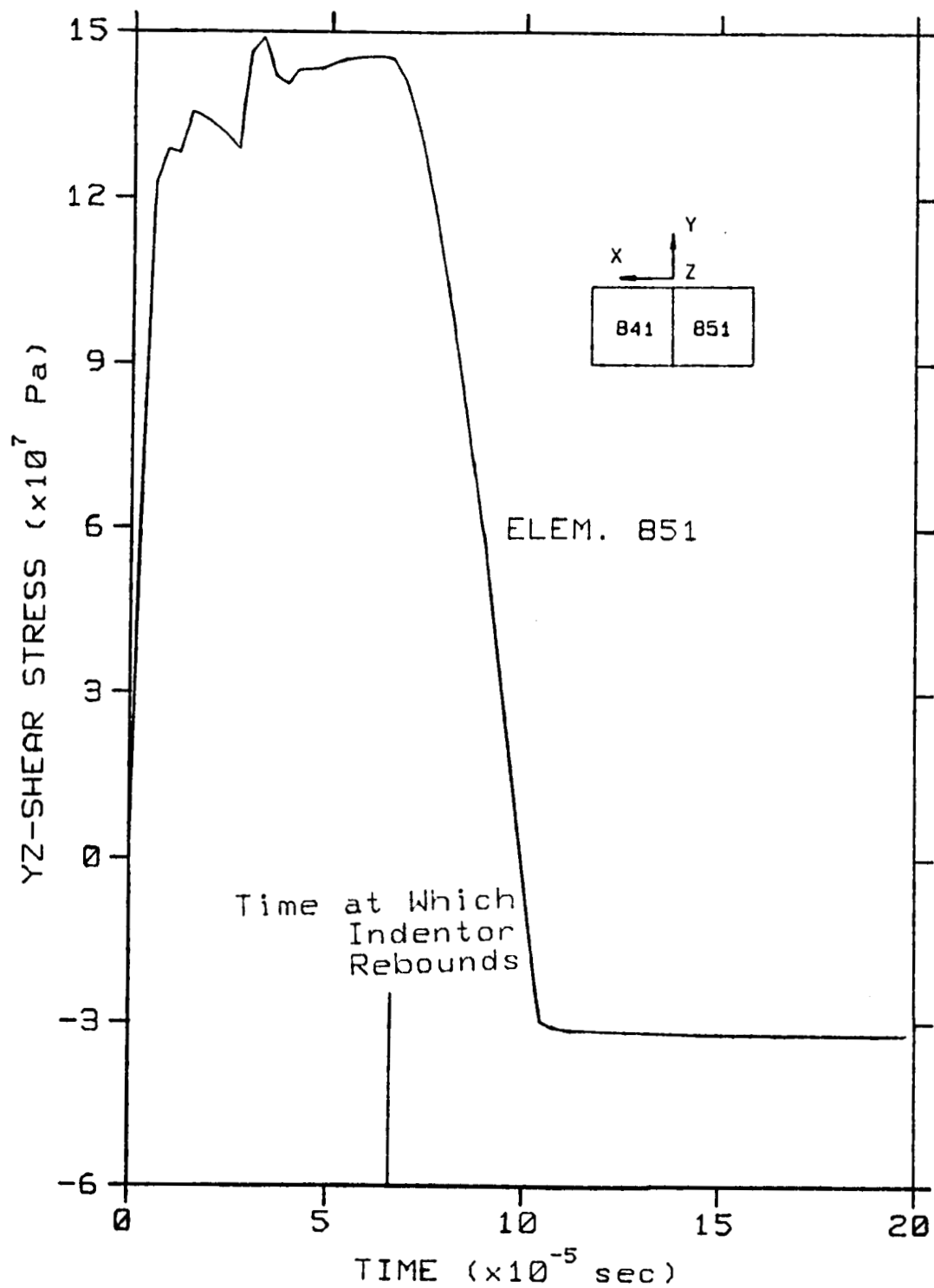


Figure 48: YZ-Shear Stress vs. Time for Element 851

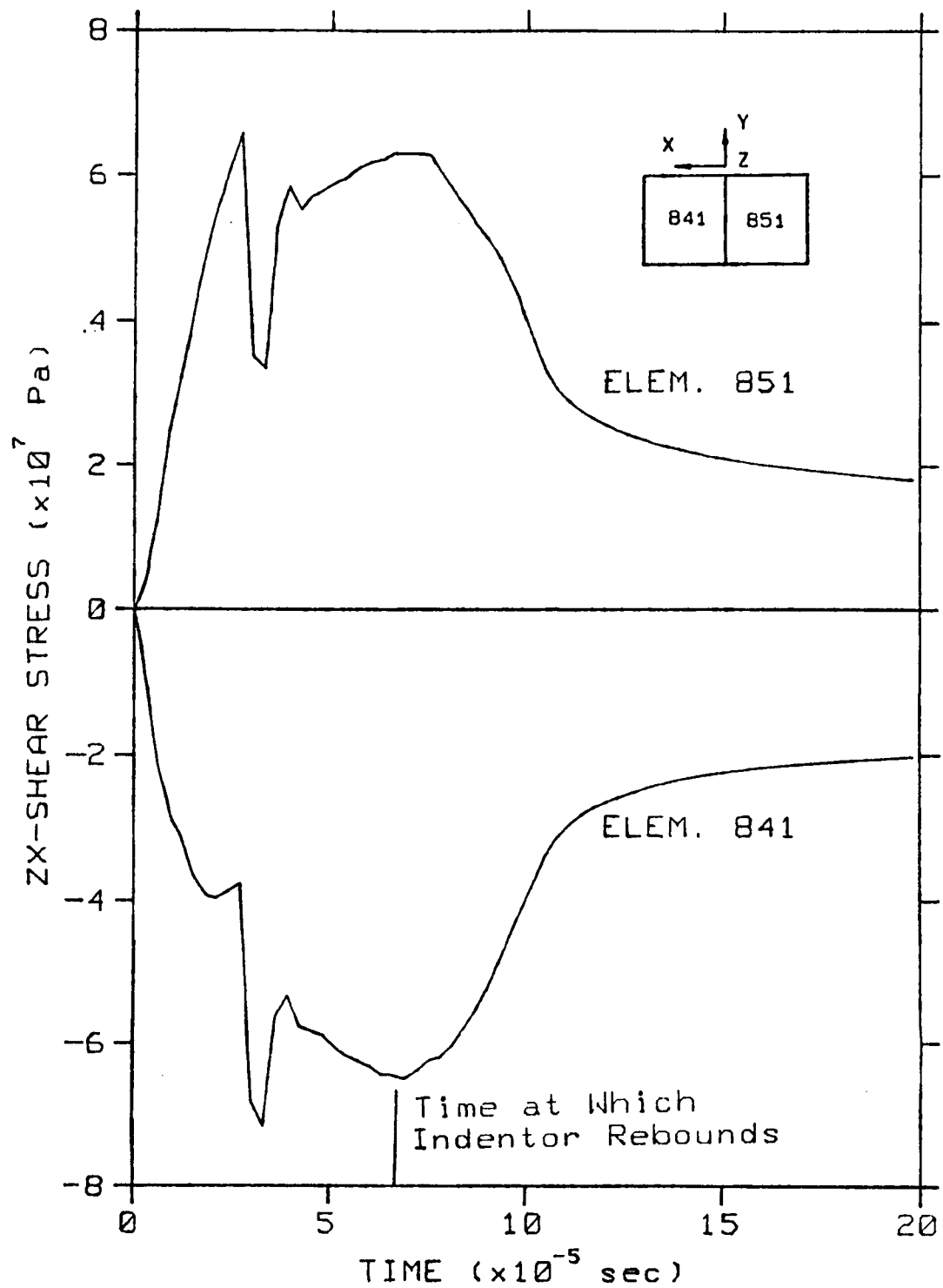


Figure 49: ZX-Shear Stress vs. Time for Elements 841 and 851

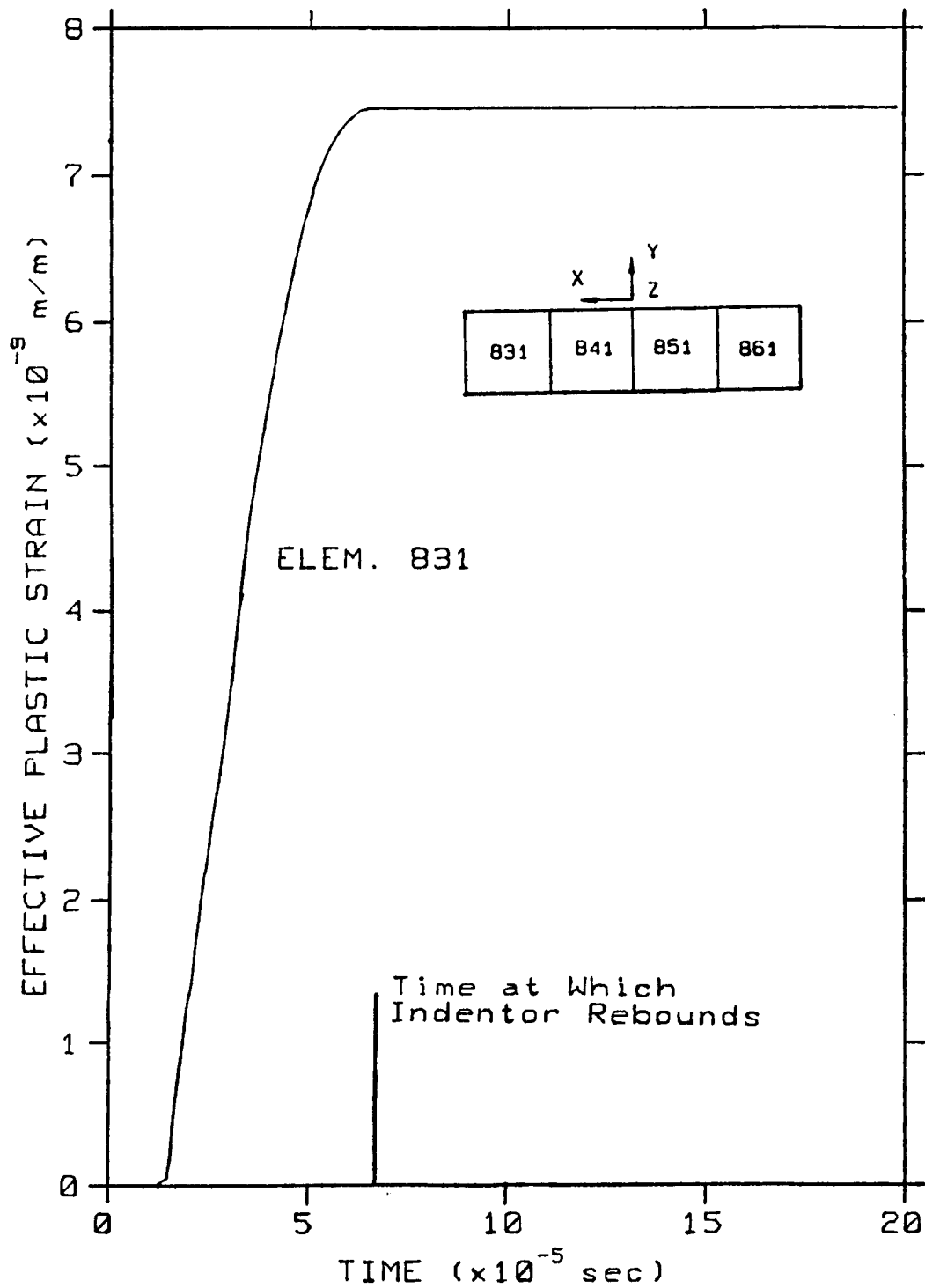


Figure 50: Effective Plastic Strain vs. Time
For Element 831

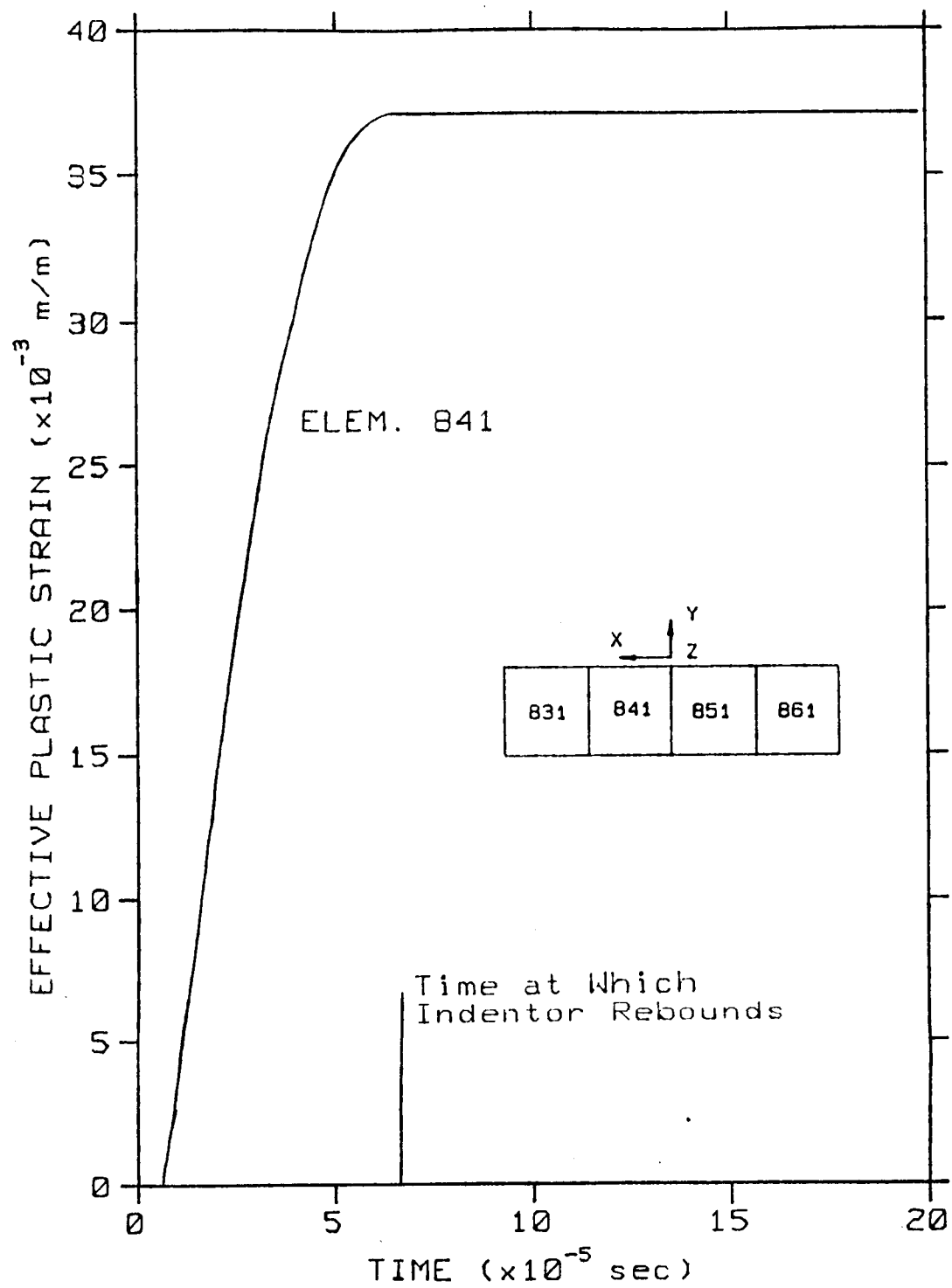


Figure 51: Effective Plastic Strain vs. Time
For Element 841

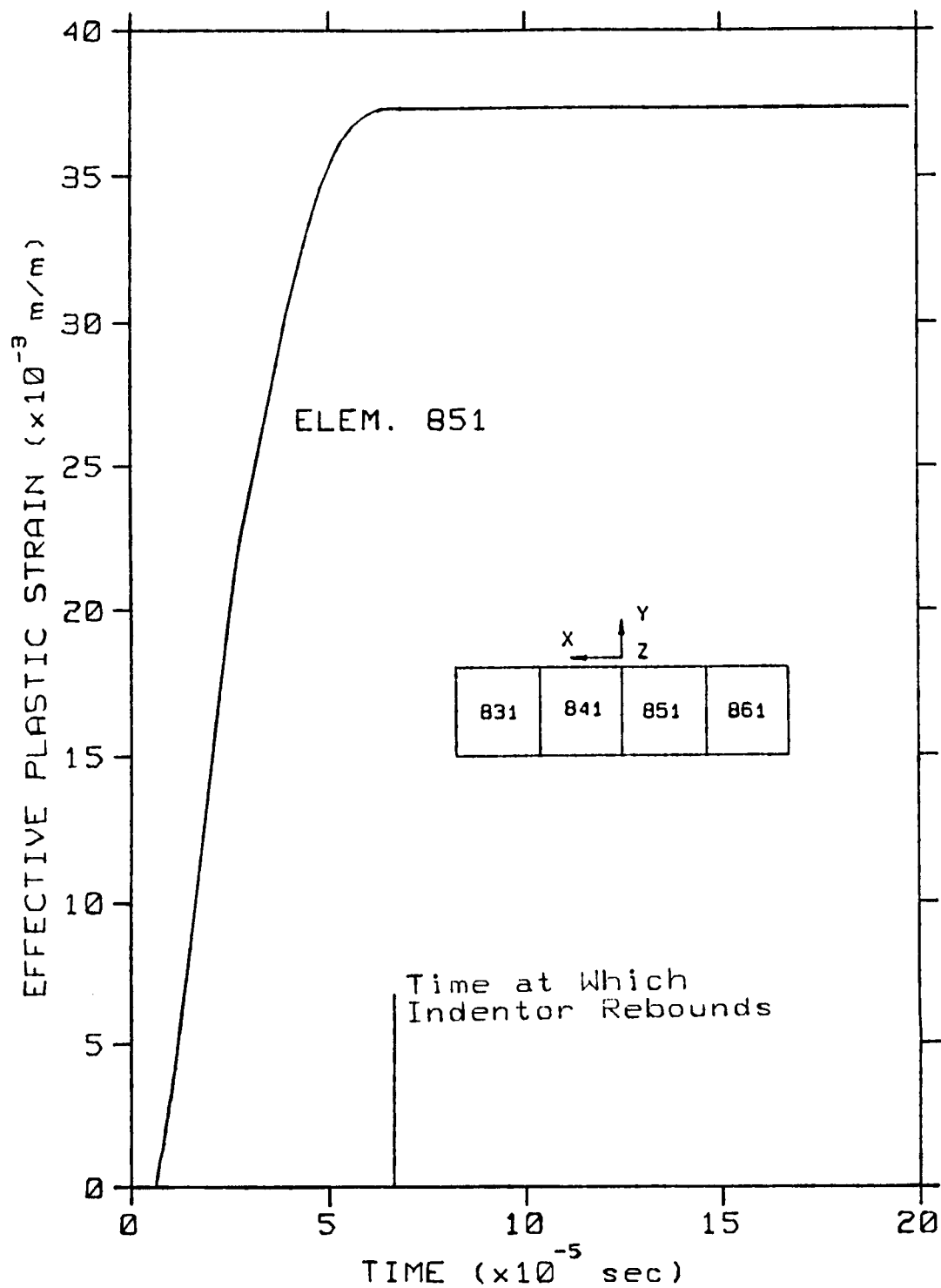


Figure 52: Effective Plastic Strain vs. Time
For Element 851

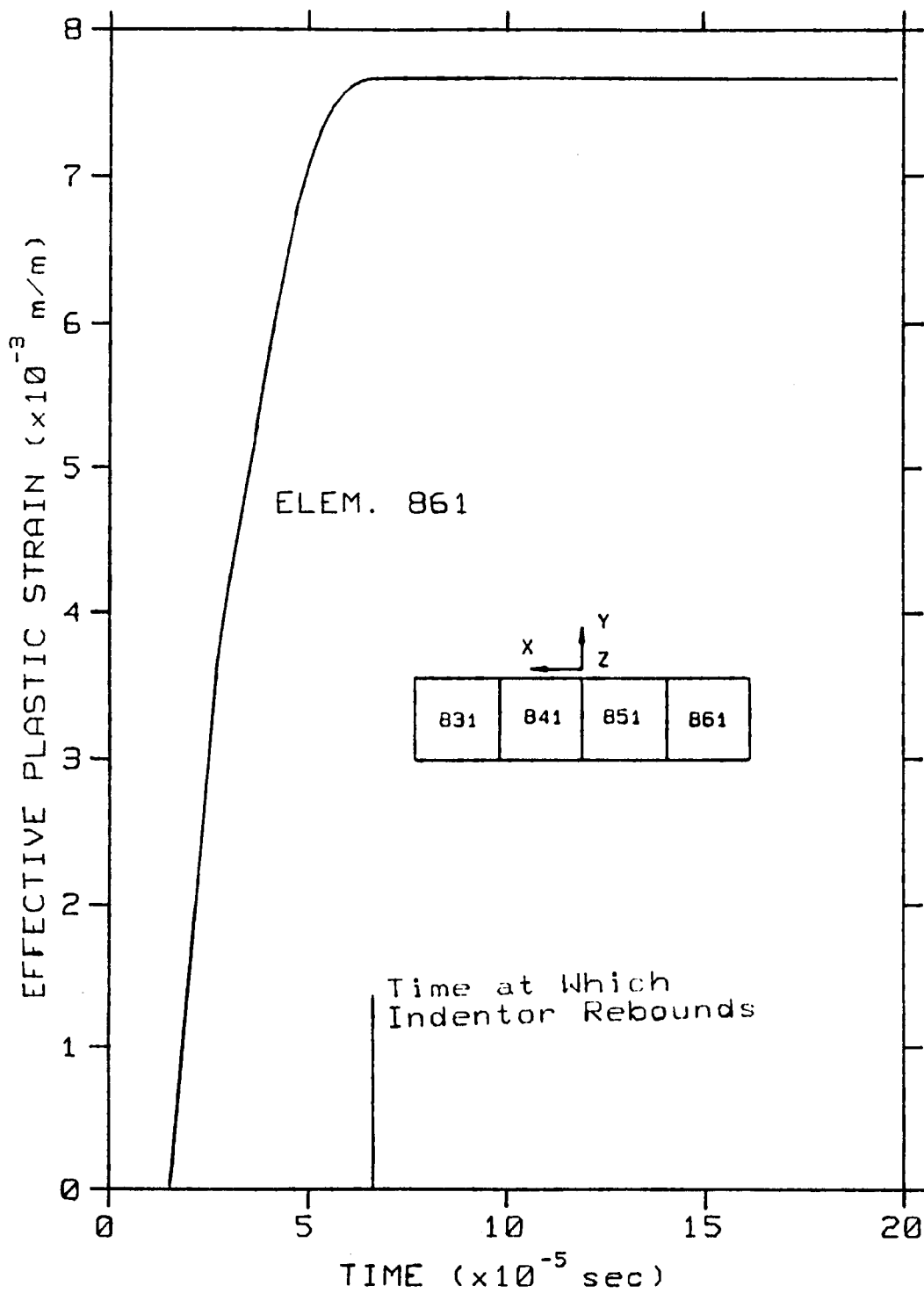


Figure 53: Effective Plastic Strain vs. Time
For Element 861

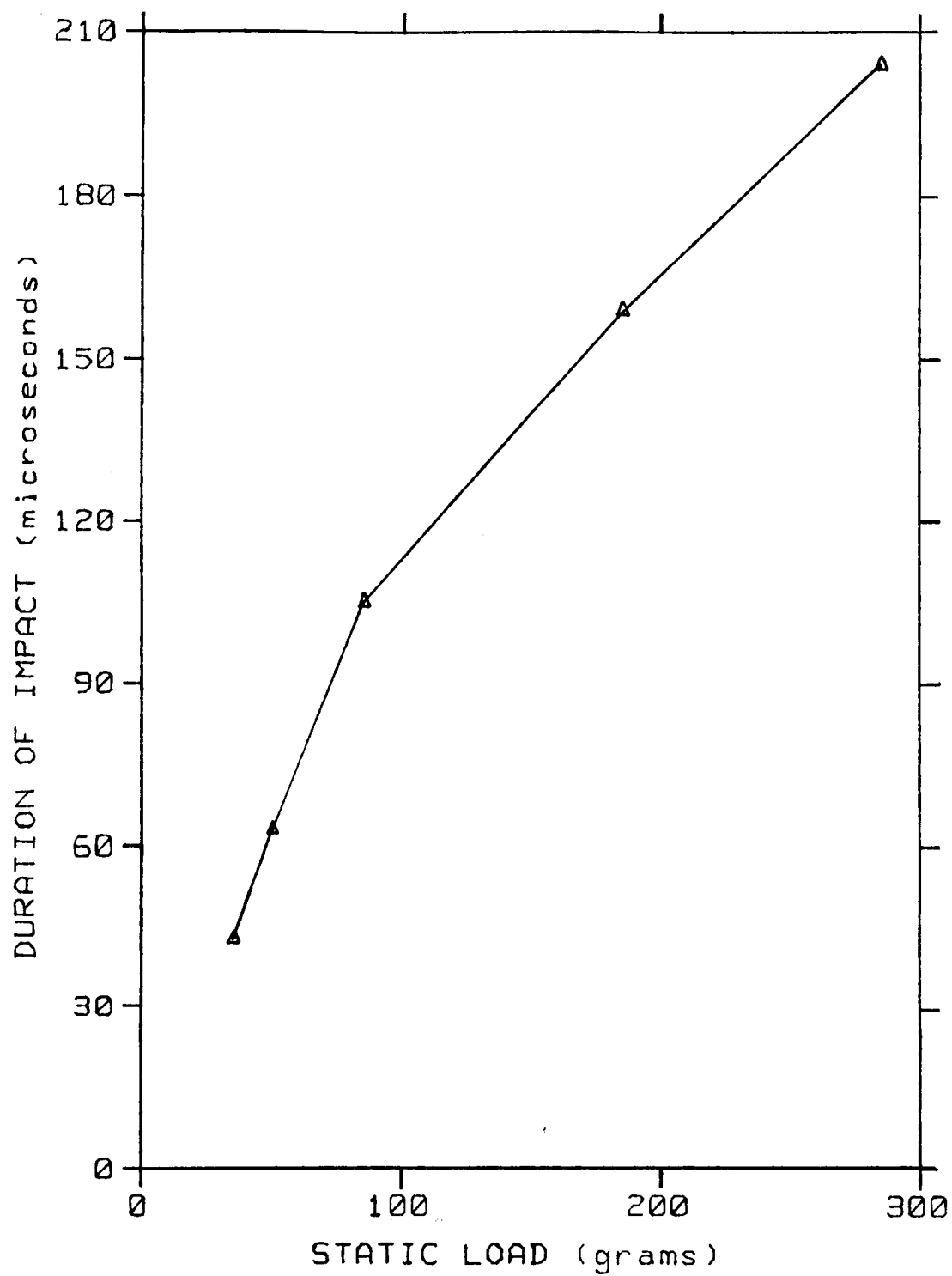


Figure 54: Duration of Impact vs. Applied Static Load

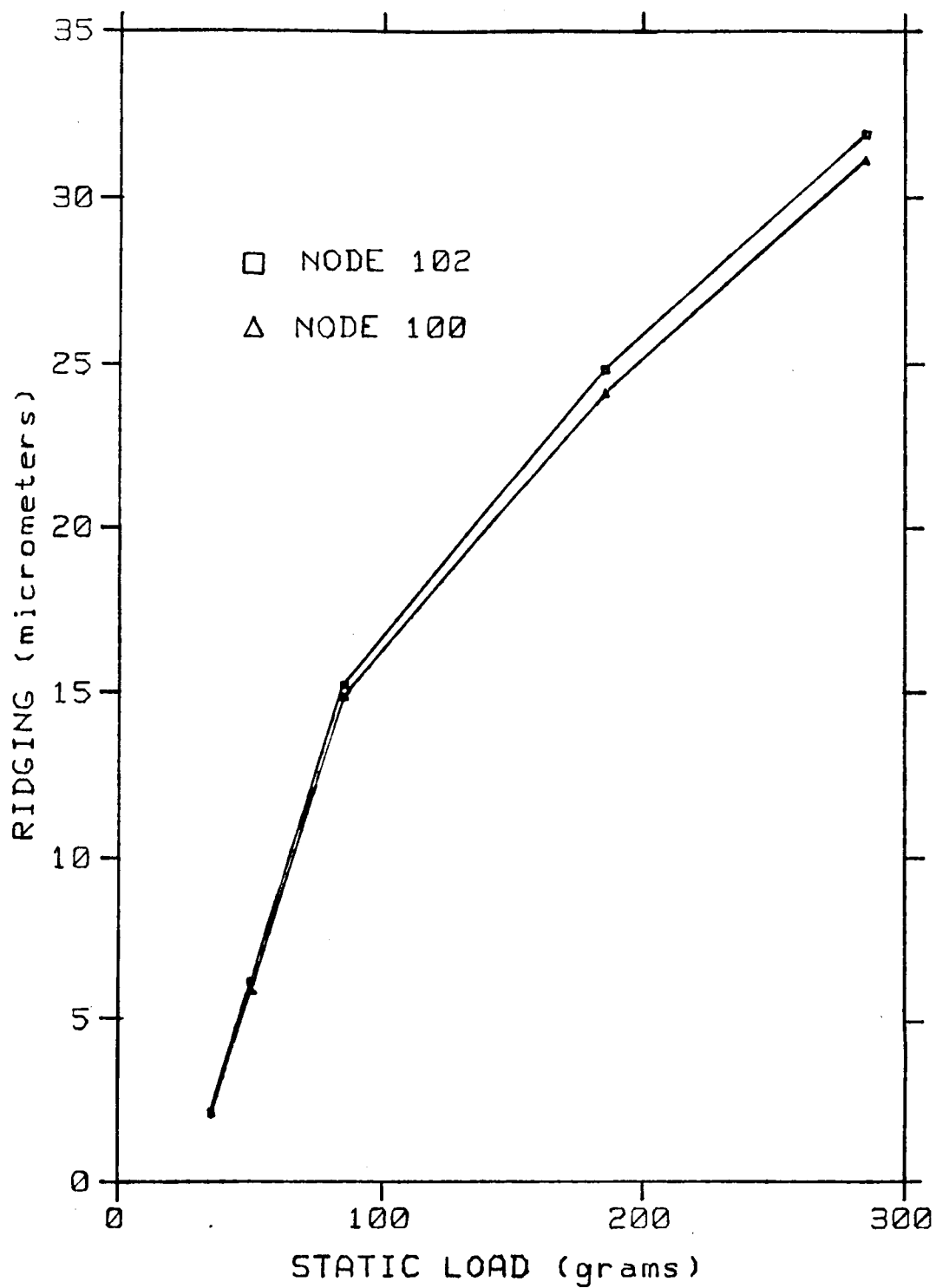


Figure 55: Amount of Ridging at Nodes 100 and 102 vs. Applied Static Load

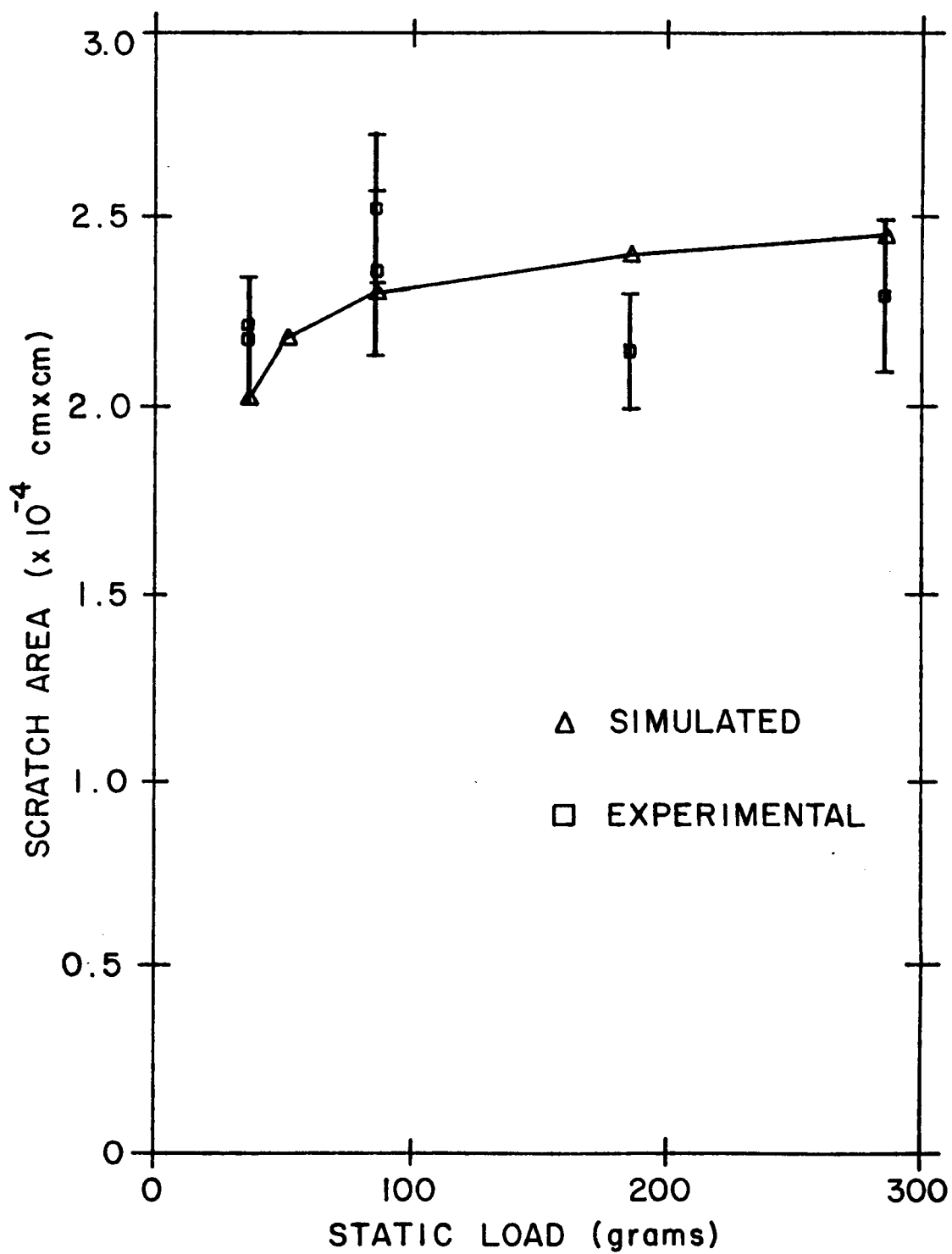


Figure 56: Comparison of the scratch area calculated by using DYNA3D and measured optically.

Appendix A

Failure Criteria Equations

Tsai-Wu Criterion [6]

Fiber failure is assumed to occur when

$$F_{11}\sigma_1^2 + 2F_{12}\sigma_1\sigma_t + F_{22}\sigma_t^2 + F_{66}\tau_{1t}^2 + F_1\sigma_1 + F_2\sigma_t \geq 1 \quad (1A)$$

where σ_1 and σ_t are normal stresses along and across the fiber direction, respectively, and τ_{1t} is the shear stress. The following strength parameters govern the lamina failure:

$$F_{11} = \frac{-1}{XX'}, \quad F_1 = \frac{1}{X} + \frac{1}{X'}, \quad F_{22} = \frac{-1}{YY'} \quad (2A)$$

$$F_2 = \frac{1}{Y} + \frac{1}{Y'}, \quad F_{66} = \frac{1}{S^2}, \quad F_{12} = \frac{-0.5}{(XX'YY')^{1/2}} \quad (3A)$$

where X and X' represent the lamina tensile and compressive strengths in the fiber direction, Y and Y' the strengths perpendicular to the fiber direction, and S the lamina shear strength.

Maximum Stress Criteria [7]

Failure is assumed to occur when any one of the following conditions is satisfied:

$$\begin{aligned} \sigma_1 &\geq X, && \text{fiber failure} \\ \sigma_t &\geq Y, && \text{transverse tension splitting} \\ \tau_{1t} &\geq S, && \text{shear splitting} \end{aligned}$$

and for compressive stresses:

$$\begin{aligned} \sigma_1 &< X', && \text{fiber crushing} \\ \sigma_t &< Y', && \text{matrix crushing} \end{aligned}$$

Appendix B

Finite-Element Technique for Calculating Elastic Strain Energy

Release Rates [9]

The relation between the rate of change of compliance and the energy release rate during and incremental crack growth in a linear elastic material is given by

$$G = \frac{1}{2} P^2 \frac{dC}{da} \quad (1B)$$

where P is the applied load and C is the compliance of the body or the inverse of the stiffness K .

If C_1 is the compliance of the body before an incremental crack growth and C_2 is the compliance after crack extension by an amount Δa , then the rate of change of compliance can be written as:

$$\frac{dC}{da} = \frac{C_1 - C_2}{\Delta a} \quad (2B)$$

Thus:

$$G = \frac{1}{2} \frac{P^2}{\Delta a} \left[\frac{1}{K_1} - \frac{1}{K_2} \right] \quad (3B)$$

where K_1 and K_2 are stiffnesses corresponding to C_1 and C_2 .

When the computed energy release rate was equal to the critical energy release rate at all node points lying near the crack tip, the nodes were split into two and the reaction forces were applied to the split nodes. These methods were the basis for Mahishi and Adams [9] analysis of delamination crack growth in composite laminates.

Appendix C

Laminate Code

A composite laminate is defined by the following code to designate the stacking sequence of ply groups, for example the group:

$$[0_3/90_2/45/-45_3]_s \quad (1C)$$

This code is represented in Figures 57 and 58, and contains the following features:

- 1.) Starting from the bottom of the plate, at $z=-h/2$, the first ply group has three plies of 0° orientation; followed by the next group with two 90° plies; followed by one 45° ply; and finally the last group with three 45° plies.
- 2.) The subscript s denotes that the laminate is symmetric with respect to the midplane or the $z=0$ plane. The upper half of the laminate is the same as the lower half except the stacking sequence is reversed.
- 3.) The laminate is symmetric if

$$\theta(z) = \theta(-z) \quad (2C)$$

$$\text{and} \quad Q_{ij}(z) = Q_{ij}(-z) \quad (3C)$$

where Q_{ij} is the ply material modulus.

ORIGINAL PAGE IS
OF POOR QUALITY

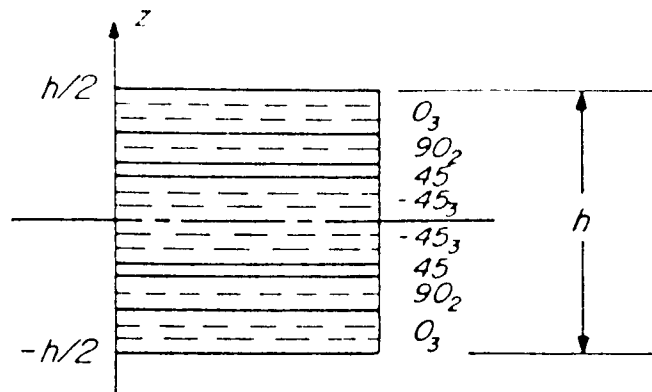


Figure 57 . Typical stacking sequence of a symmetric laminate. The laminate code as stated in Equation 1C follows an ascending order from the bottom ply (Ref. 6).

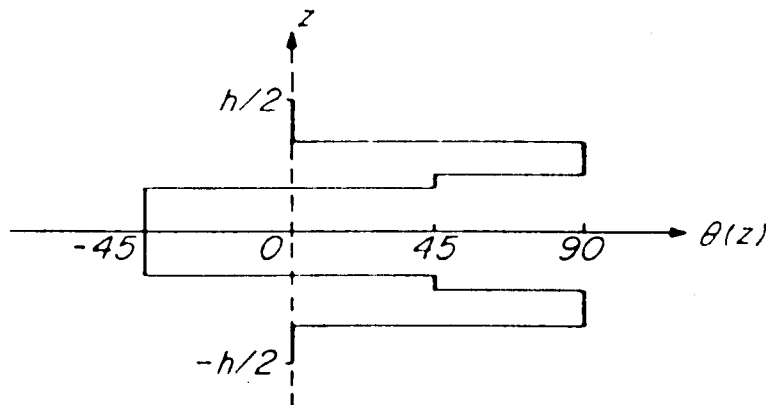


Figure 58. Ply orientations as a function of z . This is another representation of Figure 18 (Ref. 6).